Lawrence Berkeley National Laboratory
Lawrence Berkeley National Laboratory

Title
LIFETIME OF THE METASTABLE 23S1 STATE IN STORED Li+ IONS

Permalink
https://escholarship.org/uc/item/4pk4b357

Author
Knight, R.D.

Publication Date
1979-04-01

Peer reviewed

eScholarship.org Powered by the California Digital Library
University of California

Lifetime of the Metastable 2^3S_1 State in Stored Li^+ Ions

by

Randall Dewey Knight

(Ph.D. Thesis)

NOTICE

This report was prepared as an account of work sponsored by the United States Government. Neither the United States nor the United States Department of Energy, nor any of their employees, nor any of their contractors, subcontractors, or their employees, makes any warranty, express or implied, or assumes any legal liability or responsibility for the accuracy, completeness or usefulness of any information, apparatus, product or process disclosed, or represents that its use would not infringe privately owned rights.

Lawrence Berkeley Laboratory
University of California
Berkeley, California 94720

DISTRIBUTION OF THIS DOCUMENT IS UNLIMITED

Lifetime of the Metastable $2\,^3S_1$ State in Stored Li^+ Ions

By

Randall Dewey Knight

ABSTRACT

A laser-induced fluorescence technique combined with the observation of spontaneous magnetic dipole photons from the highly metastable $2\,^3S_1$ state of Li^+ has been used to measure the radiative lifetime of this state. The ions are created by electron impact on a lithium atomic beam and are subsequently stored for periods of many seconds in an RF-quadrupole ion trap. A tunable dye laser excites the $2\,^3S_1$ - $2\,^3P_1$ transition at 5485Å, and the intercombination electric dipole transition $2\,^3P_1$ - $1\,^1S_0$ at 202Å is observed. This process depletes the metastable population in a time $\tau_d < 1$ sec $\ll \tau_{^3S_1}$ and provides a measure of the total number of metastables. Comparison with the rate of 210Å spontaneously emitted photons yields a measured value for the $2\,^3S_1$ radiative lifetime of

$$\tau_{rad} = 58.6 \pm 12.9 \text{ sec},$$

where the quoted error represents 95% confidence levels. The theoretical lifetime is $\tau_{theory} = 49.0$ sec. The measured value includes data taken with both $^6Li^+$ and $^7Li^+$ isotopes and has been corrected for the slightly different detector efficiencies at 202Å and 210Å. A careful study of nonradiative quenching of the metastable state was necessary to understand observed

differences between τ_{rad} and $\tau_{^3S_1}$, the total metastable lifetime. Spatial density profiles of the ions within the trap, useful for determining the ion temperature, were obtained by scanning the laser beam horizontally across the ion trap while storing $2\,^3P_1$ - $1\,^1S_0$ photon counts as a function of the laser beam's position. Agreement with a simple equilibrium model, including space charge effects, is satisfactory. A study of the optical pumping process is necessary to understand the laser-ion interaction, and observational and theoretical data are presented.

TABLE OF CONTENTS

I. Introduction 1

II. Theoretical Background 6

A. The Physics of Two-Electron Atoms 6

1. Nonrelativistic theory 6

2. Relativistic theory - the Breit equation 10

3. Hyperfine structure 13

B. Calculation of the 2^3S_1 Radiative Lifetime 14

III. Methods of Measuring the Radiative Lifetime 18

A. Direct Determination of the Spontaneous Decay Curve 18

B. Direct Determination of the Number of Remaining Metastables 20

C. Indirect Determination of the Radiative Lifetime. 23

IV. Ion Trap Theory and Performance 29

A. The RF-Quadrupole Ion Trap 29

B. The Ion Detection System 36

C. Ion Trap Performance 43

1. Ion storage 43

2. Ion distribution 50

V. Experimental Methods 56

A. The Vacuum System 56

B. The Lithium Oven and Hot Wire Detector 60

C. The Ion Trap and Electron Gun 62

D. The Magnetic Field 66

E. Ion Trap Electronics 68
1. Trap voltages and frequencies 68
2. Ion excitation and detection 70
F. The Photon Detection System 73
1. Detector operation 73
2. Detector calibration 76
G. The Laser and Optical System 81
H. The Computer System 84
1. Timing and control 84
2. Operating and analysis programs 88

VI. Experimental Results 93
A. The Detection of Spontaneous M1 Photons 93
B. The Detection of Laser-Induced Photons 96
C. The Metastable Lifetime and Nonradiative Quenching 99
D. Procedures in Measuring the Radiative Lifetime 104
E. Data Reduction and Error Analysis 111

VII. Conclusion 119

Appendix A. Optical Pumping Calculations 121
A. The Magic Angle 121
B. The Optical Pumping Equations 123
C. Results of the Calculations 126

Appendix B. Measurements of the Ion Density Distribution 128
A. The Laser Scanning Technique 128
B. Experimental Results 130

Acknowledgements 133

References 134

I. INTRODUCTION

Without a doubt, the helium atom is one of the most studied systems in physics. In the decade leading up to the birth of quantum mechanics, helium was one of the major stumbling blocks for the simple Bohr model and provided a stimulus to search for a better theory. The early quantum mechanical calculations of Heisenberg, giving rough agreement with observation, were one of the first dramatic results showing quantum mechanics to be the sought-for theory. Since then, the helium atom, being only slightly more complicated than the "simple" hydrogen atom, has been the major testing ground of all forms of perturbation theory, and details of the spectrum have been calculated to a remarkably high level of accuracy.

It comes as something of a surprise, then, to learn that the correct decay mode of the lowest excited state ($1s2s\,^3S_1$) was not discovered until 1969! In that year, Gabriel and Jordan[1] reported the observation in the solar spectrum of lines attributed to $1s2s\,^3S_1 - 1s^2\,^1S_0$ transitions for various ions in the helium isoelectronic sequence, C V - Mg XI. (This is a nice touch of irony, since helium itself was discovered in the solar observations of Lockyer (1868) and named in accordance with the Greek word for sun - Helios.) The major work prior to this discovery was that of Breit and Teller[2], who estimated the lifetimes of the metastable 2S state in hydrogen and the $2\,^1S_0$ and $2\,^3S_1$ states in helium. Based on the earlier work of Maria Goeppert Mayer[3], they correctly predicted the dominant decay modes of 2S in H and $2\,^1S_0$ in He to be two-photon emission and obtained approximate values for the lifetimes. For the $2\,^3S_1$ state, they considered both two-photon decay and single-photon magnetic dipole decay occurring due to the breakdown of LS coupling. By making rough estimates, they concluded that the two-photon decay rate was many orders of magnitude larger than the single-photon rate, and thus two-photon decay was considered, for nearly thirty years, to be the dominant decay mode.

By the 1960's, various solar models began to require accurate values of the lifetimes of many ions, so the first detailed calculations of the two-photon decay of $2\,^3S_1$ were carried out[4]. These gave, for example, a transition rate of $\sim 9 \times 10^{-3}$ sec^{-1} for C V, far less than collisional transition rates in the solar atmosphere of ~ 8 sec^{-1}. The Breit-Teller estimate for the single-photon decay would give a C V transition rate of only $\sim 10^{-9}$ sec^{-1}. Gabriel and Jordan's discovery of strong single-photon lines thus required a major modification of the theory.

The clue, interestingly enough, was contained in Breit and Teller's original paper, but they had considered it for hydrogen only. Their suggestion, namely that using relativistic wavefunctions could alter the magnetic dipole rate, was followed up by Griem[5], who showed that it could indeed account for the observed intensities. Detailed calculations were then carried through by Schwartz[6], Drake[7], and others, verifying that single-photon relativistic magnetic dipole decay should be the dominant decay and preparing the way for experimental effort.

Laboratory searches for the $2\,^3S_1$ - $1\,^1S_0$ line in helium-like ions were begun almost immediately. The first observations, for Si XIII, S XV, and Ar XVII, were reported by Marrus and Schmieder[8], who used a beam-foil technique. The first lifetime measurement was made on Ar XVII[9], yielding a value of 172 ± 30 nsec, somewhat smaller than the theoretical value of 212 nsec[7]. Lifetimes were measured for several other ions in the range $Z \sim 20$, using beam-foil techniques, and an indirect measurement for neutral He was carried out by Moos and Woodworth[10]. The somewhat disturbing trend of the data, as it was known at the time the present work began, is shown in Figure 1[11]. Whether these deviations from theory represented an experimental error, calculational error, or a basic flaw in quantum electrodynamics was unknown. It was in the spirit of resolving this difficulty, by performing a low-Z measurement using a different technique, that the present work was undertaken.

Since then, the experimental situation has been somewhat modified, both by a new measurement in He[12] and by the discovery of nonexponential decays in the beam foil measurements[13]. It was found that after times longer than $\simeq 1$ theoretical lifetime, the measured total decay rate becomes constant and is in agreement with theory. For shorter times, as was the case

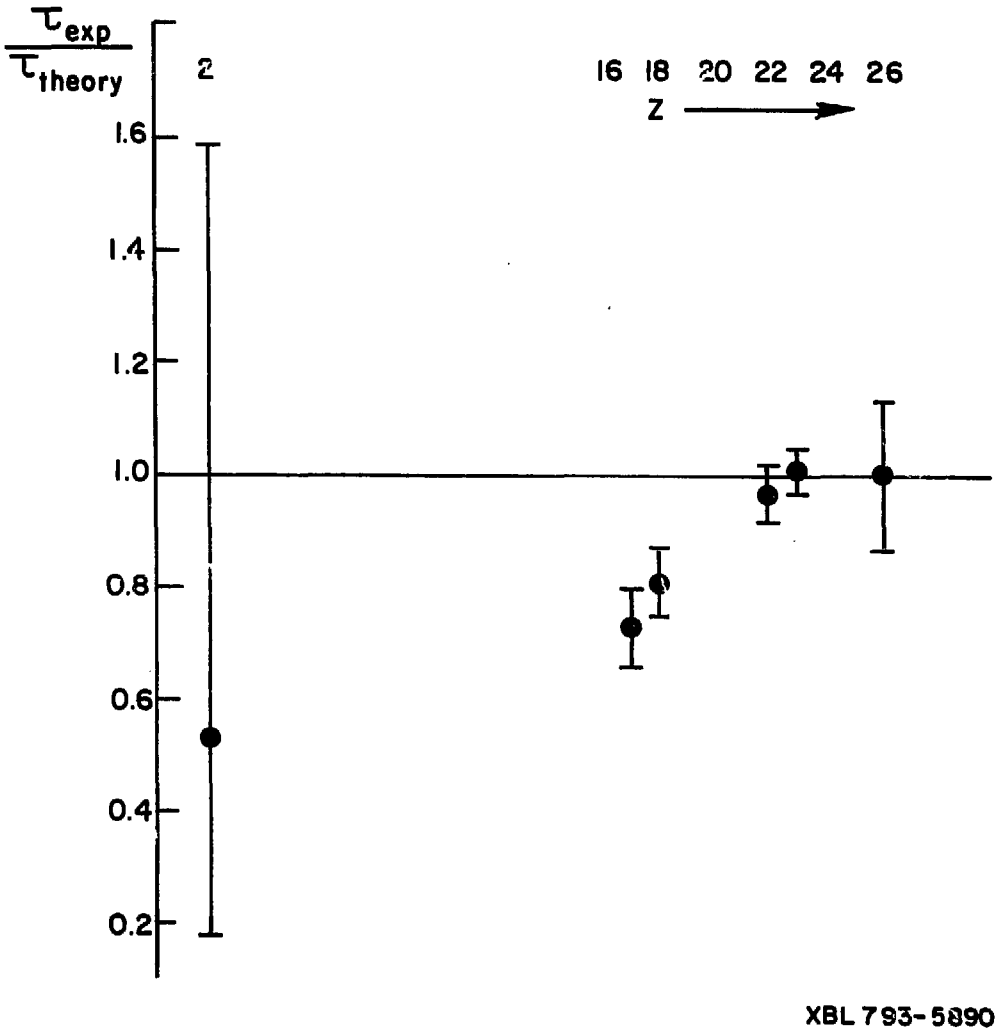


Figure 1. Comparison of experimental and theoretical values for the 2^3S_1 lifetime as of 1974.

in the earlier beam-foil measurements at $Z = 17$ and $Z = 18$, the decay is faster than exponential. This behavior is not understood, though Lin and Armstrong[14] have proposed that it may be due to unresolved Li-like ions in the beam. The present situation[15], including the results of this experiment, are shown in Figure 2. Because of the Z^{10} dependence of the transition rate, the lifetimes represented by this figure cover nearly fourteen orders of magnitude. The general agreement with theory over this wide range of values is an impressive test of our understanding of radiative mechanisms in two-electron atoms.

This thesis is, of necessity, divided into several parts. Before presenting experimental details, it will be of value to summarize the pertinent theory of two-electron atoms and the calculation of transition rates. Also required is a discussion of several methods of measuring the lifetime as well as a general treatment of the ion storage device used in this work. Following a description of the many experimental details will be a discussion of how nonradiative quenching of the metastable ions prevented the experiment from working as originally planned and how this was overcome. Finally, data will be presented, a final value for the lifetime, including possible systematic errors, will be determined, and the significance of the outcome will be discussed.

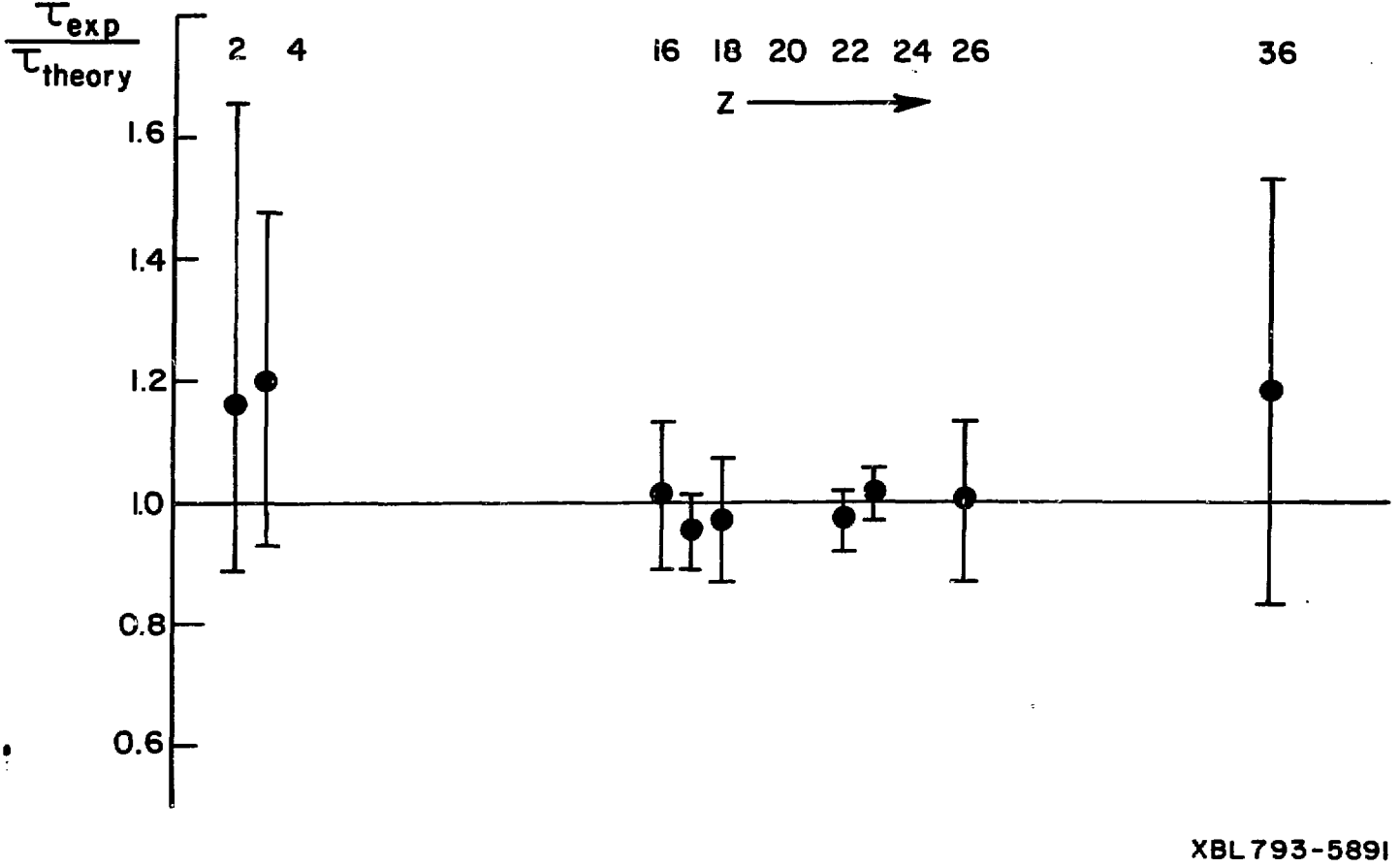


Figure 2. Present state of experiment vs. theory for the 2^3S_1 lifetime.

II. THEORETICAL BACKGROUND

A. THE PHYSICS OF TWO-ELECTRON ATOMS

For many years after the discovery of helium, the distinct spectral systems termed parahelium (singlet states) and orthohelium (triplet states) were thought to represent two different elements. One of Heisenberg's first quantum-mechanical calculations, though simplified, provided the first reasonable agreement of theory with observation[16]. In particular, it showed the importance of eigenfunction symmetry and provided the needed justification for the virtual nonexistence of singlet-triplet mixing, the basic physical mechanism underlying the exceptionally long lifetime of the $2\,^3S_1$ state studied in this work. While the theory of two-electron atoms has evolved into an enormous field in its own right, this thesis will attempt to summarize only those details pertinent to an understanding of the $2\,^3S_1$ state and the experimentally used $2\,^3P_J$ states. The discussion, except where otherwise noted, is based upon the standard reference of Bethe and Salpeter[17].

1. Non-relativistic Theory

The energy levels of Li^+ are shown in Figure 3, where data from Herzberg and Moore's spectroscopic analysis have been used[18]. The situation for all other members of the helium isoelectronic sequence is similar. The starting point for understanding these observations is the non-relativistic Schrödinger equation for two electrons and an infinitely-heavy nucleus of charge Z:

$$\mathbf{H}u = -\frac{h^2}{8\pi^2 m}\left(\nabla_1^2 u + \nabla_2^2 u\right) - \left[\frac{Ze^2}{r_1} + \frac{Ze^2}{r_2} - \frac{e^2}{r_{12}}\right]u = \mathrm{E}u.$$

Here r_1 and r_2 are distances of the first and second electrons from the nucleus, r_{12} is their mutual separation, and ∇_1^2 and ∇_2^2 are the Laplacian operators in the coordinates of the two electrons. The problem is to determine the eigenfunctions $u(\mathbf{r}_1, \mathbf{r}_2)$ and their associated eigenvalues (energy levels) E. One can note immediately that the Schrödinger equation is invariant under interchange of the electron coordinates. This has the implication that all eigenfunctions are either symmetric (parahelium) or antisymmetric (orthohelium) under interchange of the coordinates. Since matrix elements of both the non-relativistic Hamiltonian and the electric dipole operator $-e(\mathbf{r}_1+\mathbf{r}_2)$ vanish between states of different symmetry, the non-mixing of para- and orthohelium (at least to this level of approximation) is seen to arise entirely from the symmetry properties of the Hamiltonian.

If we now include the electron spin, we can, in the non-relativistic case of no spin-orbit interaction, construct wavefunctions which are simply products of a spatial wavefunction and a spin wavefunction. Since the Pauli exclusion principle requires that the total wavefunction be antisymmetric under interchange of the two electrons, we find that the parahelium states must be multiplied by the single antisymmetric spin function (S = 0)

$$S_P = \frac{1}{\sqrt{2}}\left[\alpha(1)\beta(2) - \beta(1)\alpha(2)\right],$$

and hence these are singlet states. Likewise, the orthohelium states must be multiplied by one of the three symmetric spin functions (S = 1)

$$S_+ = \alpha(1)\alpha(2)$$
$$S_0 = \frac{1}{\sqrt{2}}\left[\alpha(1)\beta(2) + \beta(1)\alpha(2)\right]$$
$$S_- = \beta(1)\beta(2),$$

and hence are triplet states. The energy differences between singlet and triplet states are due to the spatial wavefunction symmetry and not the electron spin, as can be verified from simple first-order perturbation theory[19].

The most accurate wavefunctions and energies are given by variational methods. One such method, the variation-perturbation procedure, gives results valid for the entire isoelectronic sequence. For this reason, it was used for the calculations of the $2\,^3S_1$ - $1\,^1S_0$

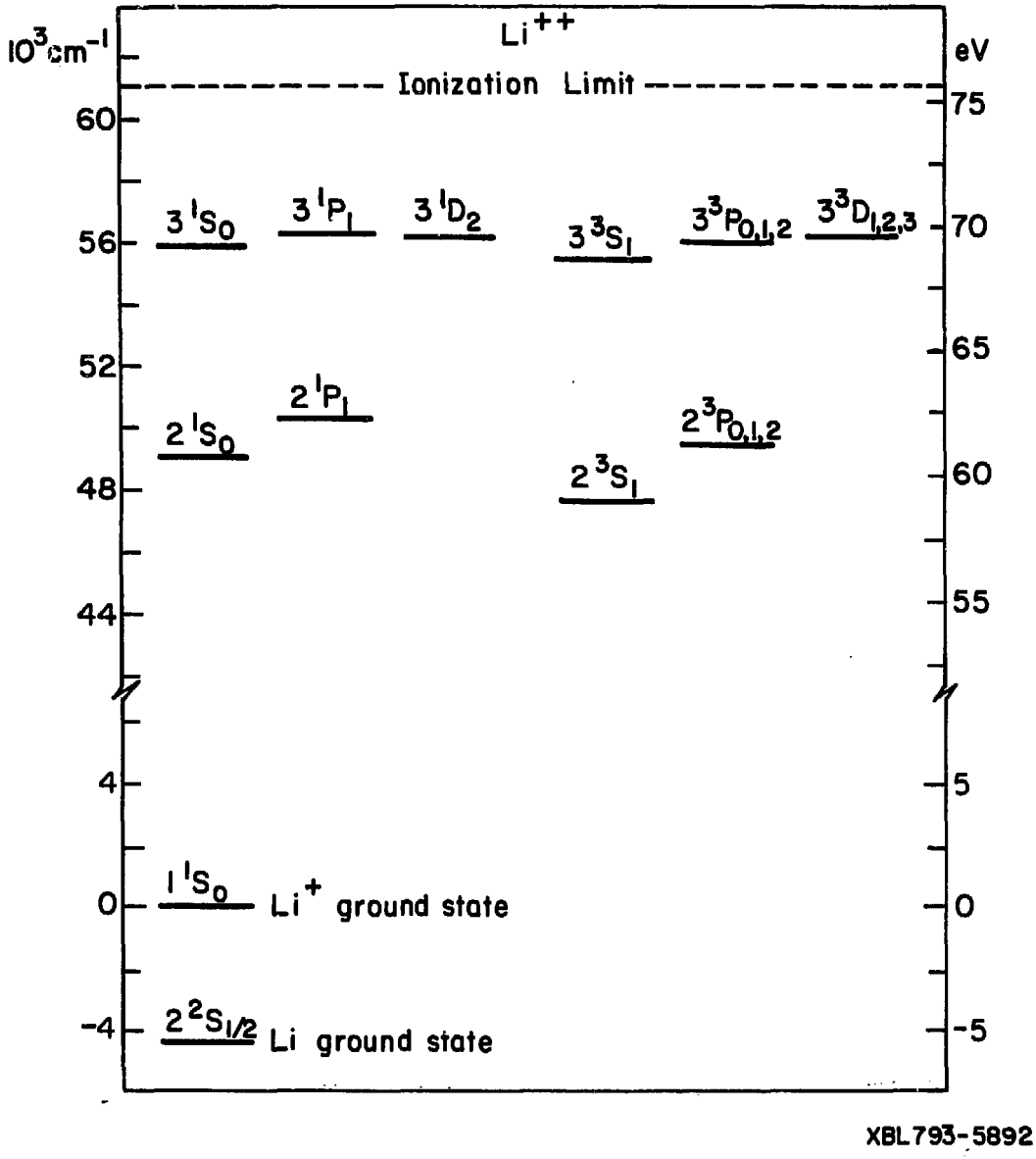


Figure 3. Energy level diagram of Li^+.

transition rate. One begins by altering the unit of length and of energy to become

$$\rho = 2Zr \qquad\qquad \epsilon = \frac{E}{2Z^2}.$$

In these units the Schrödinger equation becomes

$$\left(\mathbf{H}_0 + \lambda \mathbf{H}_1\right) u = \epsilon u,$$

where $\mathbf{H}_0 = -\frac{h^2}{4\pi^2 m}\left(\nabla_1^2 + \nabla_2^2\right) - \left(\frac{e^2}{\rho_1} + \frac{e^2}{\rho_2}\right)$, $\mathbf{H}_1 = \frac{e^2}{\rho_{12}}$, and $\lambda = \frac{1}{Z}$. We can then expand ϵ and u in inverse powers of Z by ordinary perturbation theory:

$$u = u_0 + \sum_{n=1}^{\infty} u_n Z^{-n} \qquad\qquad \epsilon = \epsilon_0 + \sum_{n=1}^{\infty} \epsilon_n Z^{-n}.$$

One easily obtains $\epsilon_0 = -1$ *Ry* in zeroth-order. Each higher order of perturbation theory determines u_n and ϵ_n by finding the stationary values of

$$J_n = \langle u_n | \mathbf{H}_0 - \epsilon_0 | u_n \rangle + 2\langle u_n | \mathbf{H}_1 - \epsilon_1 | u_{n-1} \rangle - 2 \sum_{r=0}^{2n-1} \epsilon_r \sum_{q=n-r}^{r} \langle u_q | u_{2n-r-q} \rangle$$

with respect to arbitrary variations of u_n. The trial wavefunctions at each level are expanded in the elliptic coordinates

$$s = r_1 + r_2 \qquad t = r_1 - r_2 \qquad u = r_{12}$$

and the variational equations are solved numerically. Excited states can be determined by this method if they are orthogonal to all lower states. This is automatically satisfied for $2\,^3S$ and $2\,^3P$ if they are constructed with the proper symmetry.

To compare the calculations with experiment (Table 1), it is necessary to include relativistic corrections, as discussed in the next section, and the Lamb shift. These were calculated by Pekeris[20] using variational wavefunctions. Table I shows both the straightforward variational calculations by Pekeris, using 444 parameters for $1\,^1S_0$ and 308 for $2\,^3S_1$, and variation-perturbation calculations by Knight and Scherr[21], using sixth-order perturbation theory for $1\,^1S_0$ but only third-order for $2\,^3S_1$. Both $1\,^1S_0$ calculations agree and are considerably more accurate than experiment, and the variational calculation for $2\,^3S_1$ likewise agrees with experiment. The variation-perturbation procedure for $2\,^3S_1$ only went through third-order but nonetheless resulted in an energy accurate to slightly better than 0.1%. Note, however, that the variation-

perturbation results can be applied to any Z, whereas the traditional variational procedure must be re-calculated for each Z. Since the third-order results are easy to generate and of reasonable accuracy, their use in calculating matrix elements should result in satisfactory values. This was confirmed by work of Sucher[15].

2. Relativistic Theory - The Breit Equation

The most extensively used equation for calculating details of two-electron atoms is the Breit equation:

$$\left(E - \mathbf{H}_{(1)} - \mathbf{H}_{(2)} - \frac{e^2}{r_{12}}\right)U = -\frac{e^2}{2r_{12}}\left[\alpha_1\cdot\alpha_2 + \frac{(\alpha_1\cdot\mathbf{r}_{12})(\alpha_2\cdot\mathbf{r}_{12})}{r_{12}^2}\right]U$$

where

$$\mathbf{H}_{(i)} = -e\phi(\mathbf{r}_i) + \beta_i mc^2 + \alpha_i\cdot\left(c\mathbf{p}_i + e\mathbf{A}(\mathbf{r}_i)\right)$$

and the wavefunction U has sixteen spinor components. This is similar to the Dirac equation, with the $\mathbf{H}_{(i)}$ being Dirac Hamiltonians, but is not fully Lorentz invariant. The right-hand side is the leading term for the relativistic corrections to the electron-electron interaction, but the Breit equation cannot be used for higher order corrections.

To obtain a workable form of the Breit equation, one makes the Pauli approximation by dropping the "small" components of the spinor. This leads to the equation

$$\left(\mathbf{H}_0 + \mathbf{H}_1 + \cdots \mathbf{H}_6\right)U = EU$$

where

$$\mathbf{H}_0 = -eV + \frac{1}{2m}\left(p_1^2 + p_2^2\right)$$

$$\mathbf{H}_1 = -\frac{1}{8m^3c^2}\left(p_1^4 + p_2^4\right)$$

$$\mathbf{H}_2 = -\frac{e^2}{2(mc)^2}\frac{1}{r_{12}}\left[\mathbf{p}_1\cdot\mathbf{p}_2 + \frac{\mathbf{r}_{12}\cdot(\mathbf{r}_{12}\cdot\mathbf{p}_1)\mathbf{p}_2}{r_{12}^2}\right]$$

$$\mathbf{H}_3 = \frac{\mu_B}{mc}\left\{\left[\mathbf{E}_1\times\mathbf{p}_1 + \frac{2e}{r_{12}^3}\mathbf{r}_{12}\times\mathbf{p}_2\right]\cdot\mathbf{s}_1 + \left[\mathbf{E}_2\times\mathbf{p}_2 + \frac{2e}{r_{12}^3}\mathbf{r}_{21}\times\mathbf{p}_1\right]\cdot\mathbf{s}_2\right\}$$

$$\mathbf{H}_4 = \frac{ieh}{2\pi(2mc)^2}\left(\mathbf{p}_1\cdot\mathbf{E}_1 + \mathbf{p}_2\cdot\mathbf{E}_2\right)$$

Table 1. Ionization Potentials in $^{7}Li^{+}$

	$1^{1}S_{0}(cm^{-1})$	$2^{3}S_{1}(cm^{-1})$
Knight-Scherr (Variation-perturbation method)	610079.58	133938.72
Pekeris (Variational method)	610079.62	134044.12
Experimental	610079.4±3.0	134044.19±.10

$$\mathbf{H}_5 = 4\mu_B^2\left\{-\frac{8\pi}{3}(\mathbf{s}_1\cdot\mathbf{s}_2)\delta^{(3)}(\mathbf{r}_{12}) + \frac{1}{r_{12}^3}\left[\mathbf{s}_1\cdot\mathbf{s}_2 - \frac{3(\mathbf{s}_1\cdot\mathbf{r}_{12})(\mathbf{s}_2\cdot\mathbf{r}_{12})}{r_{12}^2}\right]\right\}$$

$$\mathbf{H}_6 = 2\mu_B\left(\mathbf{B}_1\cdot\mathbf{s}_1 + \mathbf{B}_2\cdot\mathbf{s}_2\right) + \frac{e}{mc}\left(\mathbf{A}_1\cdot\mathbf{p}_1 + \mathbf{A}_2\cdot\mathbf{p}_2\right).$$

The physical significance of these terms is:

$\mathbf{H}_0$ is the ordinary non-relativistic Hamiltonian.

$\mathbf{H}_1$ is the relativistic mass correction.

$\mathbf{H}_2$ is the relativistic electron-electron interaction correction.

$\mathbf{H}_3$ is the spin-orbit interaction.

$\mathbf{H}_4$ is the Darwin term from Dirac theory.

$\mathbf{H}_5$ is the spin-spin interaction.

$\mathbf{H}_6$ is the interaction with an external magnetic field.

Some of these terms will be seen to be necessary to get an accurate operator for the magnetic moment which will give a non-zero transition rate for $2\,^3S_1$ - $1\,^1S_0$.

Terms in the Hamiltonian other than $\mathbf{H}_0$ produce the small relativistic corrections, mentioned in the preceding section, to the $1\,^1S_0$ and $2\,^3S_1$ energy levels. For triplet states with $L \neq 0$, the terms $\mathbf{H}_3$ and $\mathbf{H}_5$ (spin-orbit and spin-spin interactions) cause a fine structure splitting of states with different $\mathbf{J} = \mathbf{L} + \mathbf{S}$. In a two-electron atom, at least for small Z, spin-other orbit (included in $\mathbf{H}_3$) and spin-spin interactions are of comparable magnitude to the spin-orbit interaction and result in fine structure intervals which do not obey the Landé interval rule. In fact, for He and Li^+ the usual order of states is not even obeyed. Matrix elements of $\mathbf{H}_3$ and $\mathbf{H}_5$ evaluated with variational wavefunctions give good agreement with the observed fine structure.

Since inclusion of spin-orbit and spin-spin terms destroys pure LS coupling, the state $2\,^3P_1$ has small admixtures of $n\,^1P_1$ for $n = 2,3,4,...$ and is given by

$$|2\,^3P_1>_{true} = |2\,^3P_1> + \sum_{n=2}^{\infty}\frac{<n\,^1P_1|\mathbf{H}_{s-o} + \mathbf{H}_{s-s}|2\,^3P_1>}{E(2\,^3P_1) - E(n\,^1P_1)}|n\,^1P_1>.$$

This mixing allows a weak intercombination E1 transition $2\,^3P_1$ - $1\,^1S_0$ to the ground state in addition to the allowed E1 decay $2\,^3P_1$ - $2\,^3S_1$. Variational wavefunctions allow accurate

calculation of the coefficients in the expansion of $|2\,^3P_1>_{true}$ as well as of the dipole matrix element $<1\,^1S_0|er|2\,^3P_1>$ needed to find the transition rate[22]. For Li^+, one obtains transition rates

$$A(2\,^3P_1 - 2\,^3S_1) = 2.28\times10^7\ \text{sec}^{-1}$$
$$A(2\,^3P_1 - 1\,^1S_0) = 1.81\times10^4\ \text{sec}^{-1}.$$

The intercombination transition is important in the present work since it provides a means for determining the number of $2\,^3S_1$ ions.

3. Hyperfine Structure

The final detail needed for a complete understanding of the energy levels in the two-electron atom is the hyperfine structure. A nucleus with angular momentum I and magnetic moment $\mu = g_I\mu_N\mathbf{I}$, where $\mu_N = \dfrac{eh}{4\pi M_p c}$ is the nuclear magneton, interacts with the magnetic field produced by the electrons according to the Hamiltonian

$$\mathbf{H}_{hfs} = 2g_I\mu_N\mu_B\sum_i\left[\frac{1}{r_i^3}(\mathbf{l}_i - \mathbf{s}_i) + \frac{3}{r_i^5}(\mathbf{r}_i\cdot\mathbf{s}_i)\mathbf{r}_i + \frac{8\pi}{3}\mathbf{s}_i\delta^{(3)}(\mathbf{r}_i)\right]\cdot\mathbf{I}.$$

The hyperfine structure in two-electron atoms is almost entirely due to the inner 1s electron, for which only the Fermi-Segré term, proportional to $\delta^{(3)}(\mathbf{r})$, is non-zero. To first approximation, this causes a splitting between levels F and F+1 (where $\mathbf{F} = \mathbf{I} + \mathbf{J}$) in $2\,^3S_1$ of

$$\Delta E = \frac{4}{3}(F+1)Z^3\alpha^2 g_I\frac{m}{M_p}\,Ry.$$

Corrections include: (1) a factor $1+\epsilon$ due to the small interaction of the outer electron, (2) a factor $(1+\dfrac{m}{M_{nuc}})^{-3}$ due to finite nuclear mass, (3) a factor $1+\Delta_{qed}+\Delta_{nuc}$ due to radiative corrections and nuclear structure effects. All but Δ_{nuc} can be calculated, and one can estimate for Li^+, based on detailed calculations for ^3He [23], that $\Delta_{nuc} \sim 1\times10^{-4}$. Using measured values of g_I one obtains the $2\,^3S_1$ splittings for Li^+ shown in Table 2. The estimated error, based on uncertainties in g_I and $1+\epsilon$, is a few MHz. These values for $^7Li^+$ are in agreement with recent measurements in a Doppler-tuned ion-beam experiment[24]. Similar calculations give the hyperfine structure for the $2\,^3P_J$ states[25], also in agreement with observation[18]. The fine struc-

ture and hyperfine structure splittings are shown in Figure 4. Note that the hyperfine structure splittings in $^7Li^+$ (I=3/2) are considerably larger than in $^6Li^+$ (I=1). A knowledge of these splittings is needed to understand the optical pumping effects of exciting the $2\,^3S_1$ - $2\,^3P_1$ transition with a laser.

B. CALCULATION OF THE $2\,^3S_1$ RADIATIVE LIFETIME

Since the $2\,^3S_1$ - $1\,^1S_0$ transition has $J = 1 \rightarrow 0$ and no parity change, the only possible single-photon decay (neglecting hyperfine mixing) is magnetic dipole. The transition rate for such a decay is given by

$$A = \frac{8\pi}{3}\frac{\omega^3}{hc^3}\left|<1\,^1S_0|\mu|2\,^3S_1>\right|^2.$$

In the non-relativistic case $\mu = \frac{e}{2mc}(\mathbf{L} + 2\mathbf{S})$, which will not mix $1\,^1S_0$ and $2\,^3S_1$ because of the orthogonal wavefunctions. It is possible for the decay to proceed due to configuration interactions which mix higher states (in this case autoionizing states) with $1\,^1S_0$ and $2\,^3S_1$, but Breit and Teller showed that the transition rate in this case is far less than for two-photon decay[2]. One can also show that hyperfine mixing, such as the E2 transition arising from the mixing of $n\,^1D_2$ with $2\,^3S_1$, is too weak to be of any consequence[7].

The discovery of single-photon decay gave rise to an investigation of relativistic corrections, both to the wavefunction and to the operator μ. A systematic method of proceding is to perform multiple Foldy-Wouthuysen transformations on the Dirac one-electron Hamiltonians until all terms of order $m(Z\alpha)^4$ are obtained (second Pauli approximation), and then to pick out those terms which are linear in the vector potential A and thus contribute to single-photon processes. In addition, one includes those parts of $\mathbf{H}_0, \cdots, \mathbf{H}_6$ from Section II.A.2. which originated from the Breit interaction, lets $\mathbf{p} \rightarrow \mathbf{p} + \frac{e}{c}\mathbf{A}$, and keeps only the terms linear in A. If now $\mathbf{A} = \epsilon e^{-i\mathbf{k}\cdot\mathbf{r}}$, a multipole expansion consistent with the above requires keeping the "finite wavelength" correction terms of order $(kr)^2$. One obtains then for the M1 parts of A,

Table 2. Hyperfine Splittings of the 2^3S_1 Level in Li^+

		Theory (GHz)	Experiment (GHz)
$^6Li^+$:	ΔE(0-1)	3.000	-
	ΔE(1-2)	6.000	-
$^7Li^+$:	ΔE(1/2-3/2)	11.886	11.872±.012
	ΔE(3/2-5/2)	19.810	19.798±.024

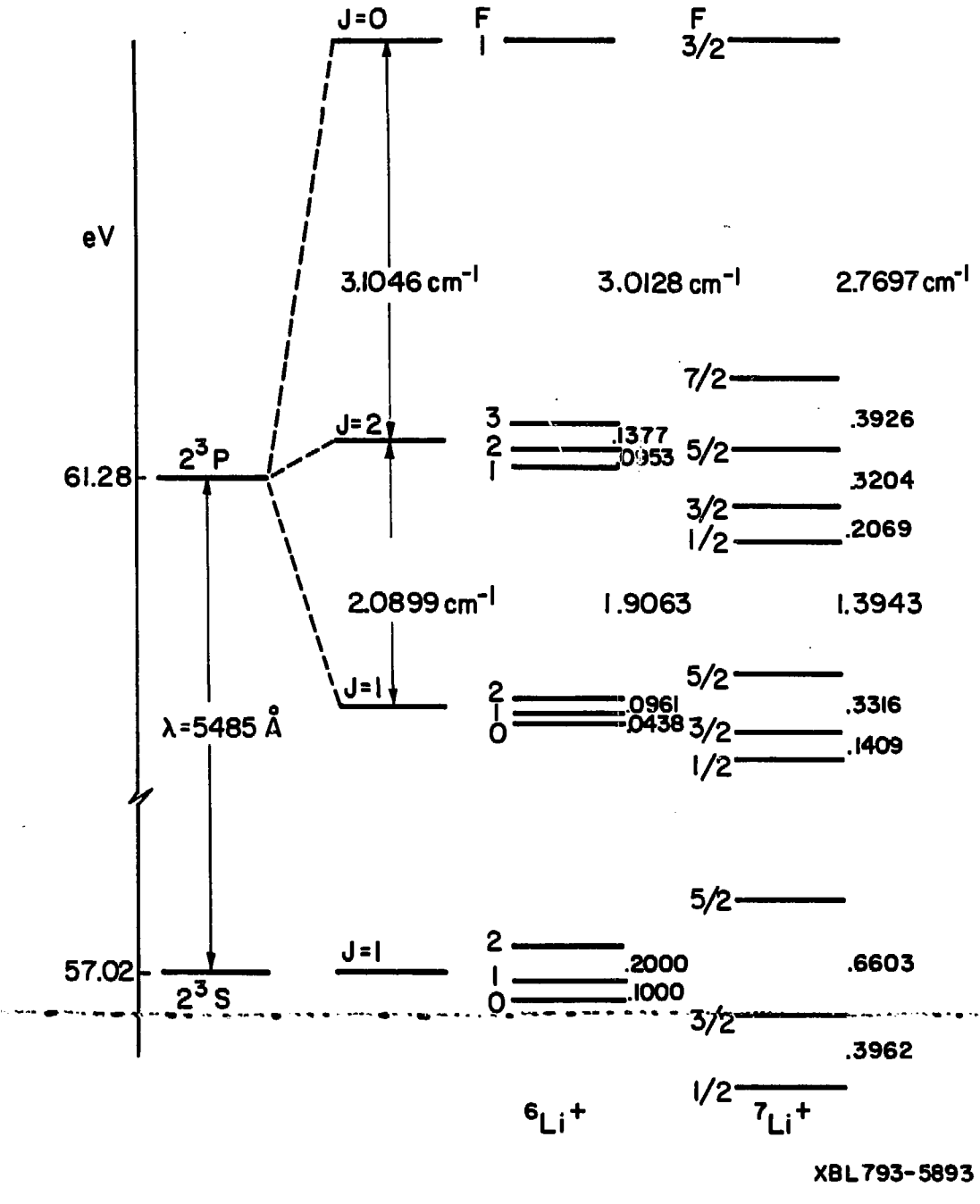


Figure 4. Fine and hyperfine structure in the 2^3S_1 and $2^3P_{0,1,2}$ multiplets for $^6Li^+$ (I=1) and $^7Li^+$ (I=3/2).

$$\mathbf{A} = \frac{i}{2}(\boldsymbol{\epsilon}\times\mathbf{k})\times\mathbf{r}\left(1 - \frac{1}{10}k^2r^2\right).$$

Algebraic manipulation of the remaining terms of the Hamiltonian into the form $\mathbf{H}_m = -i(\boldsymbol{\epsilon}\times\mathbf{k})\cdot\boldsymbol{\mu}$ gives the relativistic magnetic dipole operator

$$\boldsymbol{\mu} = \mu_B\sum_i\left(\mathbf{l}_i + 2\mathbf{s}_i - \frac{p_i^2}{2m^2c^2}(\mathbf{l}_i + 2\mathbf{s}_i) + \frac{1}{2m^2c^2}\mathbf{p}_i\times(\mathbf{p}_i\times\mathbf{s}_i) + \frac{1}{10}\frac{\omega^2}{c^2}[\mathbf{r}_i\times(\mathbf{r}_i\times 2\mathbf{s}_i) - r_i^2(\mathbf{l}_i + 2\mathbf{s}_i)]\right.$$
$$\left. - \frac{Ze^2}{mc^2r_i^3}\mathbf{r}_i\times(\mathbf{r}_i\times\mathbf{s}_i) + \frac{\omega}{2mc^2}\mathbf{s}_i\right)$$
$$+ \mu_B\frac{e^2}{2mc^2r_{12}}\left(\frac{1}{r_{12}^2}\left[\mathbf{r}_{12}\times[\mathbf{r}_{12}\times(2\mathbf{s}_1 + 2\mathbf{s}_2)] + (\mathbf{r}_1\times\mathbf{r}_2)\mathbf{r}_{12}\cdot(\mathbf{p}_1 + \mathbf{p}_2)\right] - (\mathbf{r}_1\times\mathbf{p}_2) - (\mathbf{r}_2\times\mathbf{p}_1)\right).$$

The initial terms, L + 2S, are recognized as the non-relativistic operator. All remaining terms arise from the order $m(Z\alpha)^4$ correction.

To evaluate the transition rate, one needs the matrix element of μ between $1\,^1S_0$ and $2\,^3S_1$. From symmetry considerations, only those terms in μ which are antisymmetric in the spin variables give a non-zero contribution. This is a large simplification, and more algebra eventually leads to

$$<1\,^1S_0|\mu|2\,^3S_1>_{m=0} = \mu_B<1\,^1S_0|\frac{-2}{3m^2c^2}(p_1^2 - p_2^2) - \frac{1}{6}\frac{\omega^2}{c^2}(r_1^2 - r_2^2) + \frac{Ze^2}{3mc^2}(\frac{1}{r_1} - \frac{1}{r_2})|2\,^3S_1>.$$

Drake[7] evaluated this using the variation-perturbation wavefunctions described in Section II.A.1. and thus obtained transition rates for all Z. For Li^+ the resulting rate and associated lifetime are

$$A = 2.039\times10^{-2}\ \text{sec}^{-1} \qquad \tau = \frac{1}{A} = 49.04\ \text{sec.}$$

Dimensional analysis shows that the transition rate scales as

$$A \sim \alpha(Z\alpha)^{10}\frac{mc^2}{h}.$$

The difference in reduced mass of the $^6Li^+$ and $^7Li^+$ isotopes studied causes their transition rates to differ by only $\sim$1 part in 10^4, much too small to be observed.

The present work is in reasonable agreement with these results, though the fact that observed lifetimes for both Z = 2 and Z = 3 are slightly longer than predicted by theory is somewhat disturbing and will be considered in the conclusion.

III. METHODS OF MEASURING THE RADIATIVE LIFETIME

A. DIRECT DETERMINATION OF THE SPONTANEOUS DECAY CURVE

Of the several possible methods of measuring the radiative lifetime, the most straightforward, at least in principle, is simply to detect spontaneously emitted photons as a function of time and thus construct a decay curve. This approach has the additional advantage of being most analogous to the beam-foil experiments and would reveal any nonexponential behavior of the decay. For a signal characterized by

$$S(t) = S_0 e^{-t/\tau(t)},$$

the "lifetime" at any instant of time t is defined by

$$\frac{1}{\tau(t)} = -\frac{d}{dt}\left[\ln S(t)\right].$$

For a true exponential decay, the graph of $\ln S$ *vs* t is a straight line with slope $-1/\tau$ independent of t.

The general procedure for obtaining a spontaneous decay curve would be to create and store some number of metastable Li^+ ions, store photon counts as a function of time in bins which are T seconds wide, measure the background and subtract it from the data, and finally perform a least squares analysis of the data to determine the lifetime τ_{3s_1}. Since the number of photons detected in one interval T is much less than the total number of metastable ions, the counts obey Poisson statistics[26]. The probable error (standard deviation) associated with an interval which has accumulated n counts in many repetitions is then $\sigma = \sqrt{n}$.

In order to compare this approach with other methods of obtaining the lifetime, it is useful to estimate the time required to obtain a given signal-to-noise ratio. In particular, consider the time needed for the bin at $t = \tau = 50$sec to have a signal-to-noise (S/N) of 10. If the signal rate is

$$\frac{ds}{dt} = \dot{s}_0 e^{-t/\tau}$$

and the background rate is

$$\frac{db}{dt} = \dot{b}_0 = \text{constant},$$

then in n cycles, a data bin T seconds wide ($T \ll \tau$) at $t = \tau$ collects

$$s(\tau) = n\dot{s}_0 e^{-1}\tau\left(1 - e^{-T/\tau}\right) + nT\dot{b}_0 \cong nT\left(\dot{s}_0 e^{-1} + \dot{b}_0\right)$$

counts, while the number of counts in a background bin is

$$b(\tau) = nT\dot{b}_0.$$

Then the "signal" is

$$S = s - b = nT\dot{s}_0 e^{-1}$$

while the "noise", statistical plus background, is

$$N = \sqrt{nT\left(\dot{s}_0 e^{-1} + \dot{b}_0\right) + nT\dot{b}_0} = \sqrt{nT\left(\dot{s}_0 e^{-1} + 2\dot{b}_0\right)}.$$

The requirement S/N = 10 becomes

$$\text{S/N} = \dot{s}_0 e^{-1}\sqrt{\frac{nT}{\dot{s}_0 e^{-1} + 2\dot{b}_0}} = 10.$$

Typical values of the parameters are: T = 5 sec, $\dot{s}_0 = 1$ sec^{-1}, $\dot{b}_0 = .3$ sec^{-1}. Solving for n then gives $n = 140$ cycles. Since each cycle consists of a data collection period of $\simeq$60 sec, a background collection period of equal length, and several seconds spent filling the trap, the total time required for a 10% measurement is estimated to be

$$T_{10\%} \cong 5 \text{ hours}.$$

While this is not prohibitively long, a faster method of obtaining data would clearly be desirable.

B. DIRECT DETERMINATION OF THE NUMBER OF REMAINING METASTABLES

An alternative method of measuring the lifetime is to determine the number of metastables remaining at time t. This number has the same $e^{-t/\tau}$ dependence as the spontaneous decay curve. The advantage to this method is that counting N metastables in time $T \ll \tau_{^3S_1}$ yields much better S/N than counting $\frac{dN}{dt} \cdot T \ll N$ photons, as was the case in the preceding section. A means whereby N can be determined is shown in Figure 5. Radiation at 5485Å from a laser excites the ions from $2\,^3S_1$ to $2\,^3P_1$, from where they have a branching ratio of $\simeq$1:1200 for decaying to $1\,^1S_0$ by emitting a 202Å photon which can be detected. By repeatedly undergoing interaction with the laser beam until the intercombination decay occurs, all metastables ions are depleted in a characteristic time τ_I, emitting N photons in the process. If $\tau_I \ll \tau_{^3S_1}$, then the number of photons counted is directly proportional to the number of metastables present at the instant the laser was turned on. This, of course, is a destructive measurement, so a full measurement of $N(t)$ requires filling the ion trap many times and increasing after each fill the time delay t before the laser is turned on.

To estimate τ_I, a simple model can be used. A more detailed calculation, including Doppler widths, hyperfine structure, ion densities, etc., is described in Appendix A. Ignoring these for now, consider a laser beam of radiation density/frequency ρ and of cross section L^2, equal to the ion cloud cross section, impinging on the ions. Neglecting spontaneous decay of $2\,^3S_1$, which will be justified if $\tau_I \ll \tau_{^3S_1}$, the rate equations governing the populations are

$$\frac{dN}{dt} = A\left[N' + \beta(N' - N)\right]$$
$$\frac{dN'}{dt} = -A\left[N' + \beta(N' - N)\right] - A'N'.$$

N and N' are, respectively, the $2\,^3S_1$ and $2\,^3P_1$ populations, A and A' are the allowed and intercombination decay rates of $2\,^3P_1$ discussed in Section II.A.2., and

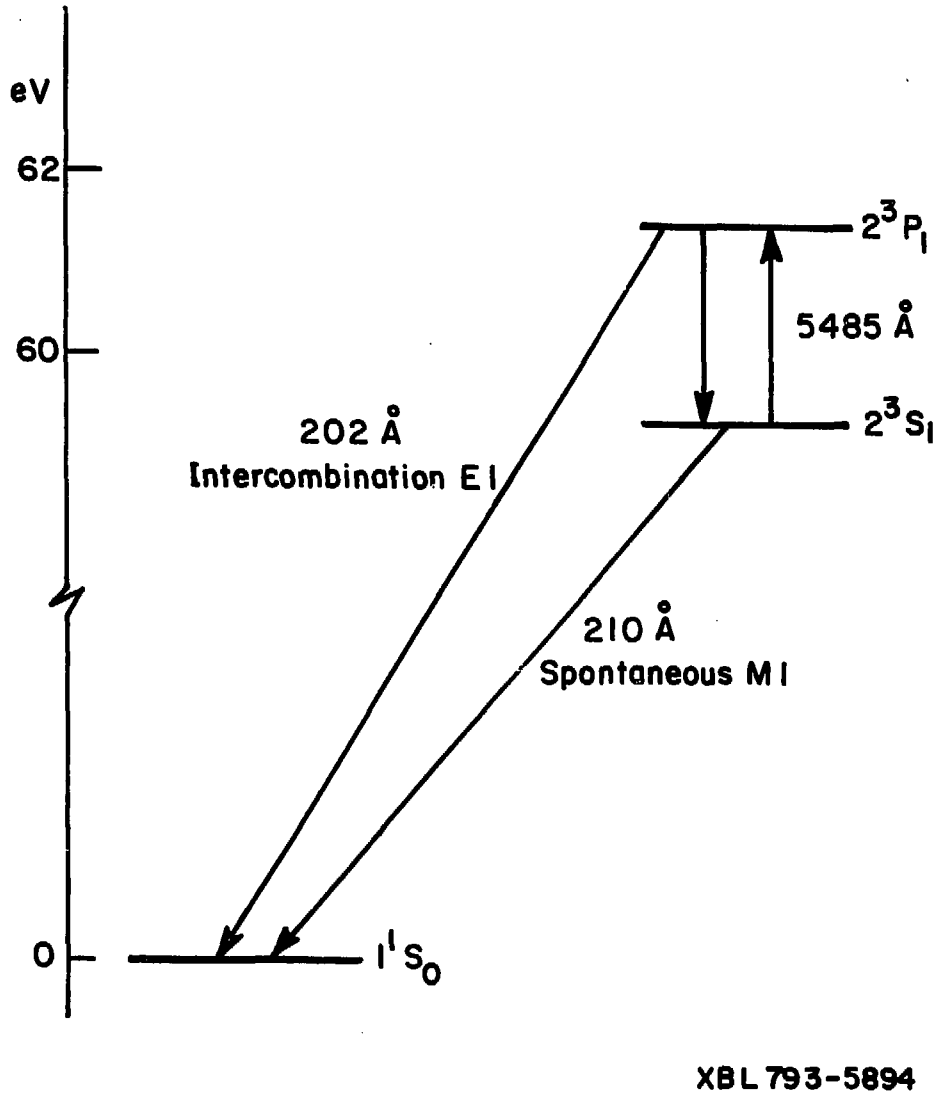


Figure 5. Levels involved in the 5485Å laser-induced intercombination decay at 202Å.

$$\beta = \frac{2\pi^3 c^3 \rho}{h\omega^3}$$

comes from the relation between the Einstein A and B coefficients. All experimentally reasonable situations give $\beta << 1$ (stimulated emission negligible), in which case an approximate solution for the metastable population is

$$N(t) = N_0 e^{-\beta A' t},$$

which yields

$$\tau_l = \frac{1}{\beta A'}.$$

Typical parameters are $L^2 = 2$ cm^2 and a laser power P = 50 mW with a bandwidth $\delta\lambda = .1$Å, resulting in $\beta = 7.5 \times 10^{-4}$. With $A' = 1.81 \times 10^4 \text{sec}^{-1}$, the estimate for the laser depletion time is

$$\tau_l = .075 \text{ sec.}$$

Consideration of hyperfine structure and Doppler widths slows this process somewhat, but the measured values of $\tau_l \cong .2$ sec confirm the basic physics of this model and satisfy $\tau_l << \tau_{^3S_1}$.

The signal-to-noise for this method can be estimated along the same lines as in the preceding section. Consider data bins T seconds wide, where $T << \tau_{^3S_1}$, but $T >> \tau_l$ so that all remaining metastables are counted. Then in n cycles, the bin at $t = \tau$ has received

$$s(\tau) = n\int_{\tau}^{\infty} \dot{s}_0 e^{-t/\tau} dt + nT\dot{b}_0 \cong n\tau\dot{s}_0 e^{-1} + nT\dot{b}_0$$

and again

$$b(\tau) = nT\dot{b}_0.$$

This results in

$$S/N = \tau\dot{s}_0 e^{-1} \sqrt{\frac{n}{\tau\dot{s}_0 e^{-1} + 2T\dot{b}_0}},$$

which, for the parameters used before, gives S/N $\simeq$ 10 for $n = 6$. With delays up to 60 sec, as before, the time required by one cycle is

$$t_{cycle} = 2 \cdot \left[0 + 5 + 10 + \cdots + 60\right] = 780 \text{ sec},$$

where the factor of 2 includes the time spent collecting background. Allowing a few seconds for

each filling of the trap, the time needed for a 10% measurement is estimated to be

$$T_{10\%} \cong 1\frac{1}{2} \text{ hours.}$$

This is a substantial gain over the estimated 5 hours needed to measure τ_{3S_1} by observing the spontaneous decay, and for this reason the experiment was designed to utilize this approach. The major constraint is that the number of ions created during each fill must not vary. This would not be a problem when measuring spontaneous counts since each fill is for a separate complete measurement.

C. INDIRECT DETERMINATION OF THE RADIATIVE LIFETIME

Unfortunately, the possibility of other loss mechanisms dominating the $2\,^3S_1$ lifetime was not fully appreciated during the design phase of the experiment. Immediately upon beginning to collect data, however, it became apparent that the observed metastable lifetime, even at the best obtainable vacuum of $\simeq 5 \times 10^{-10}$ torr, was much less than the theoretical radiative lifetime:

$$\tau_{3S_1} \sim 5 \text{ sec} \ll \tau_{theory} = 49 \text{ sec.}$$

As will be discussed in Chapter VI, this loss is predominantly due to nonradiative quenching of the metastable ions in collisions with the background gas molecules. The direct methods of the preceding two sections can only measure the total metastable lifetime, τ_{3S_1}, and not the radiative lifetime separately. This section will discuss how the radiative lifetime may, nonetheless, be obtained.

In general, we note that, at any instant of time, the rate $\frac{dS}{dt}$ at which photons are emitted is related to the number N of metastables by

$$\frac{dS}{dt}(t) = \frac{1}{\tau_{rad}} N(t),$$

independent of any nonradiative losses. A simultaneous measurement of $\frac{dS}{dt}$ and N would

then allow the radiative lifetime to be determined indirectly. This is essentially the procedure used by Moos and Woodworth[10] to measure the $2\,^3S_1$ lifetime in He. While a simultaneous and instantaneous measurement is not experimentally feasible, a sufficiently good approximation can be made. Consider the case where, following ion creation, a total S_1 of spontaneous M1 photons are counted for a time T_1, then the laser is turned on and a total S_2 of M1 photons plus laser-induced photons are counted for a time T_2. To a first approximation, we have

$$\tau_{rad} = \frac{S_2}{S_1/T_1}.$$

A better expression is obtained from a detailed look at the several competing loss processes. Let the various loss rates be

$\frac{1}{\tau_{rad}}$ = radiative loss rate,

$\frac{1}{\tau_q}$ = nonradiative loss rate − quenching plus storage losses,

and $\frac{1}{\tau_l}$ = laser depletion loss rate.

Then while the laser is off, the total metastable lifetime $\tau_{^3S_1}$ is given by

$$\frac{1}{\tau_{^3S_1}} = \frac{1}{\tau_{rad}} + \frac{1}{\tau_q},$$

while with the laser on, the total depletion lifetime τ_d is

$$\frac{1}{\tau_d} = \frac{1}{\tau_{rad}} + \frac{1}{\tau_q} + \frac{1}{\tau_l}.$$

Either of the direct methods discussed in the preceding two sections can be used to measure $\tau_{^3S_1}$, although in practice the method of measuring the remaining metastables by laser depletion is used because of its superior S/N in a fixed amount of time. The depletion lifetime τ_d is determined by a least squares analysis of the decay curve observed when the laser is switched on. Details of the data collection are given in Chapter VI.

The rate equations for photon counting in the periods T_1 and T_2 can be written as

$$\text{In } T_1\text{:}\quad \frac{dS_1}{dt} = \epsilon_{210}\frac{N_0}{\tau_{rad}}\exp\left[-t/\tau_{3S_1}\right]$$

$$\text{In } T_2\text{:}\quad \frac{dS_2}{dt'} = \epsilon_{210}\frac{N_0\exp\left[-T_1/\tau_{3S_1}\right]}{\tau_{rad}}e^{-t'/\tau_d} + \epsilon_{202}\frac{N_0\exp\left[-T_1/\tau_{3S_1}\right]}{\tau_l}e^{-t'/\tau_d},$$

where ϵ_{210} and ϵ_{202} are, respectively, the efficiencies for counting the 210Å spontaneous photons and the 202Å laser-induced photons, N_0 is the initial number of metastable ions, and $t' = t - T_1$. Integrating these equations to obtain the number of photons counted during T_1 and T_2 results in

$$S_1 = \epsilon_{210}N_0\frac{\tau_{3S_1}}{\tau_{rad}}\left[1 - \exp\left[-T_1/\tau_{3S_1}\right]\right]$$

and

$$S_2 = \left[\frac{\epsilon_{210}}{\tau_{rad}} + \frac{\epsilon_{202}}{\tau_l}\right]N_0\exp\left[-T_1/\tau_{3S_1}\right]\tau_d\left[1 - e^{-T_2/\tau_d}\right].$$

Eliminating N_0 and solving for τ_{rad} gives a final expression for the radiative lifetime of

$$\tau_{rad} = \frac{\epsilon_{210}}{\epsilon_{202}}\frac{\tau_{3S_1}^2}{\tau_{3S_1} - \tau_d}\left[\left\{\exp\left[T_1/\tau_{3S_1}\right] - 1\right\}\frac{S_2'}{S_1} - \frac{\tau_d}{\tau_{3S_1}}\right],$$

where

$$S_2' = \frac{S_2}{1 - e^{-T_2/\tau_d}}$$

is the number of photons which would be counted if $T_2 \rightarrow \infty$. This analysis has assumed that the decays during both T_1 and T_2 are exponential, an assumption consistent with the data.

In practice, the first channel collecting laser-induced photons is artificially low due to the finite time ($\simeq$20 msec) required for the laser shutter to open. This fact complicates the determination of both the depletion time τ_d and the estimate S_2' of the number of photons which would be counted if the laser were on for an infinite time. The situation is as depicted in Figure 6, where just the data channels corresponding to laser-induced photons are shown. The experimentally measured number of counts in T_2 is just $S_2 = \sum_{n=0}^{T_2/T} s_n$. It is seen that τ_d can be

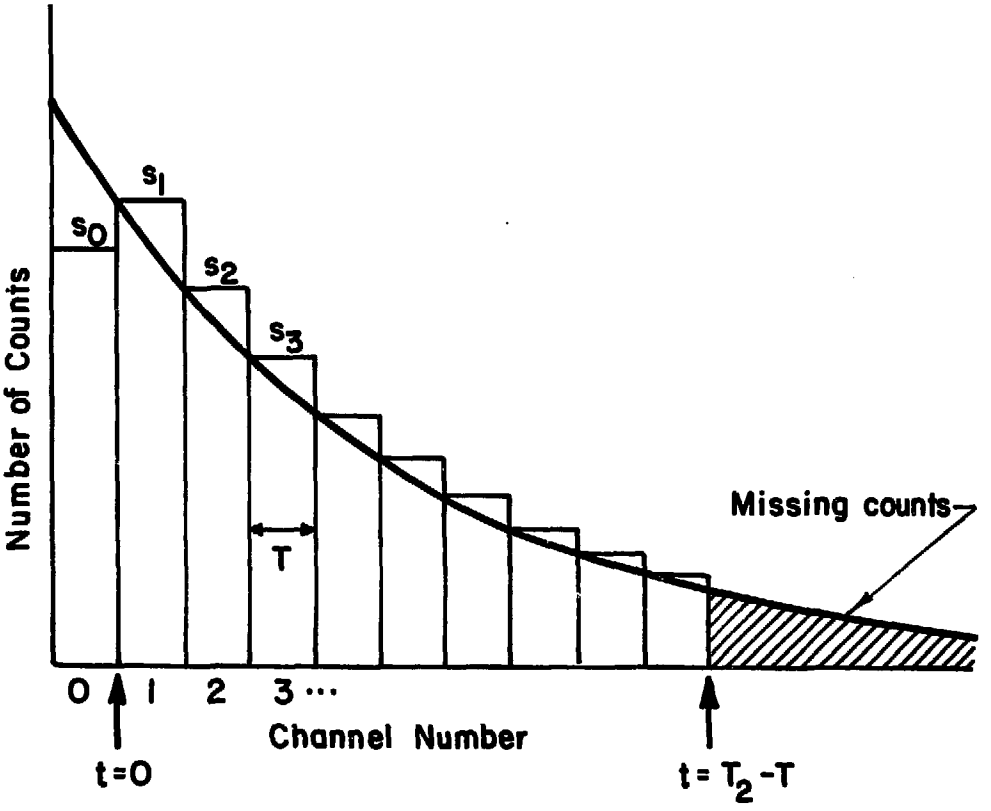


Figure 6. Laser-induced counts, showing the low signal in channel 0 due to the shutter opening and also the number of missing counts which must be estimated.

easily determined by simply ignoring the first channel when performing the least squares analysis of the decay. Estimating the number of "missing" counts is a bit trickier. If the least squares fit gives a count rate for $t \geqslant 0$ of

$$\frac{ds}{dt} = \frac{S_0}{\tau_d} e^{-t/\tau_d},$$

then the measured number of counts for $t \geqslant 0$, i.e. excluding the s_0 counts in channel zero, is

$$S_2 - s_0 = \int_0^{T_2-T} \frac{S_0}{\tau_d} e^{-t/\tau_d} dt = S_0\left[1 - e^{-(T_2-T)/\tau_d}\right].$$

The number which would be counted for all $t \geqslant 0$ is simply S_0, so adding in s_0 to include channel zero gives an estimate for the number S_2' of photons which would be counted in an infinite time:

$$S_2' = s_0 + \frac{S_2 - s_0}{1 - e^{-(T_2-T)/\tau_d}}.$$

This more accurate value for S_2' is used in the calculation of τ_{rad} rather than the previous expression for S_2' which did not take into account the finite time required to open the laser shutter.

The final item needed for a determination of the lifetime is an estimate of the error. The detector efficiency factor $\frac{\epsilon_{210}}{\epsilon_{202}}$ is not considered during the data analysis, the quantity evaluated being $\tau = \frac{\epsilon_{202}}{\epsilon_{210}} \tau_{rad}$. Since the various factors entering the expression for τ_{rad} are independent, an error analysis gives

$$\sigma^2(\tau) = \left(\frac{\partial\tau}{\partial S_1}\right)^2 \sigma^2(S_1) + \left(\frac{\partial\tau}{\partial S_2'}\right)^2 \sigma^2(S_2') + \left(\frac{\partial\tau}{\partial \tau_{^3S_1}}\right)^2 \sigma^2(\tau_{^3S_1}) + \left(\frac{\partial\tau}{\partial \tau_d}\right)^2 \sigma^2(\tau_d).$$

Evaluation of the derivatives results in an expression for the error of

$$\sigma^2(\tau) = \left(\frac{\tau_{rad}+\tau_l}{S_1}\right)^2\sigma^2(S_1) + \left(\frac{\tau_{rad}+\tau_l}{S_2'}\right)^2\sigma^2(S_2')$$
$$+\left[\left\{\frac{2}{\tau_{^3S_1}} - \frac{1}{\tau_{^3S_1}-\tau_d} - \frac{T_1}{\tau_{^3S_1}^2\left(1-\exp(-T_1/\tau_{^3S_1})\right)}\right\}\left(\tau_d+\tau_l\right) + \frac{\tau_l^2}{\tau_{^3S_1}^2}\right]\sigma^2(\tau_{^3S_1})$$
$$+\left[\left\{\frac{1}{\tau_{^3S_1}-\tau_d} + \frac{T_2}{\tau_d^2\left(\exp(T_2/\tau_d)-1\right)}\right\}\left(\tau_d+\tau_l\right) - \frac{\tau_l^2}{\tau_d^2}\right]\sigma^2(\tau_d).$$

The errors $\sigma(\tau_{^3S_1})$ and $\sigma(\tau_d)$ are evaluated in the least squares analysis routines by standard algorithms for computing the variance[26]. The errors $\sigma(S_1)$ and $\sigma(S_2')$ are Poisson values, including the effects of background subtraction. Since S_2 and S_2' usually differ by $< 1\%$, $\frac{\sigma^2(S_2')}{S_2'^2}$ is replaced by $\frac{\sigma^2(S_2)}{S_2^2}$ in the above expression.

This section has shown how the problem of nonradiative quenching can be sidestepped and has derived expressions for the radiative lifetime and the probable error associated with it. These expressions are based upon numerous quantities which can be experimentally determined. The remainder of this thesis will be concerned with the experimental details associated with the actual measurements of these quantities.

IV. ION TRAP THEORY AND PERFORMANCE

A. THE RF-QUADRUPOLE ION TRAP

The most stringent requirement of this work is the ability to confine ions for many seconds in a manner such that they have negligible interaction with any perturbing forces. A device which meets this requirement by utilizing electric and/or magnetic fields is an ion trap. Three general types of ion traps have been employed by different investigators: the Penning trap[27], which uses a strong magnetic field and DC electric fields; the electrostatic trap[28], which confines ions in orbits about a central wire; and the rf-quadrupole trap[27], which takes advantage of the ability of a radio frequency field to create a pseudopotential for ions. The use of a Penning trap for this experiment was not feasible because of the constraints imposed by the apparatus to be used. An electrostatic trap is attractive for many reasons, but led to concern that randomizing collisions of the ions would cause them to strike the center wire and result in inadequate storage times. The rf-quadrupole ion trap, which was thus chosen, was known to possess good storage properties, was compatible with existing equipment, and would provide the ions with a a relatively benign environment. This chapter will discuss the trapping, detection, and equilibrium properties of ions in an rf-quadrupole trap. More information can be found in Dehmelt's review articles[27]. Details of the trap construction are deferred to the next chapter.

The rf-quadrupole ion trap is an extension of the quadrupole mass filter developed by Paul[29]. A quadrupole potential, which is chosen for its simple properties and ease of construction, is generated by the hyperboloids of revolution shown in Figure 7. Specifying boun-

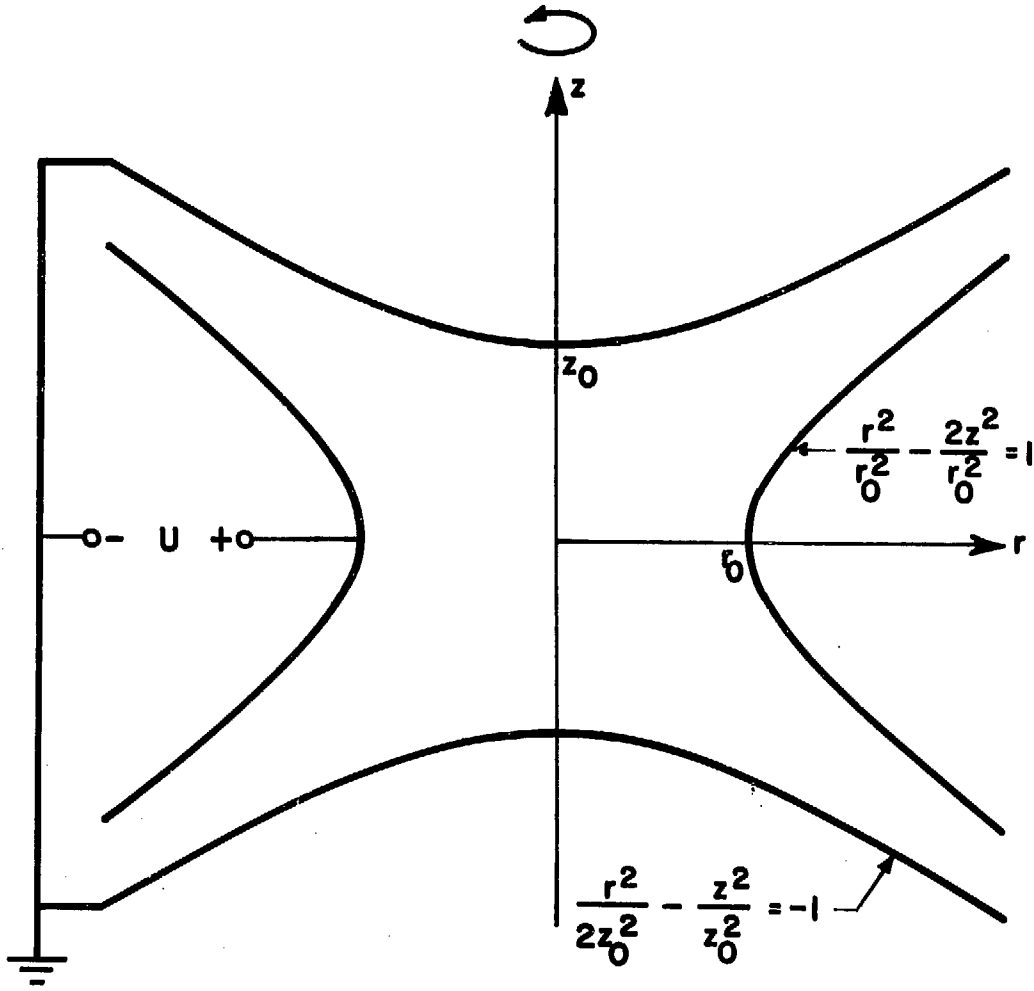


Figure 7. Geometry of the RF-quadrupole ion trap.

dary conditions of grounded end electrodes and a potential U on the ring electrode, the solution of Laplace's equation for the potential is

$$\phi = \frac{U}{r_0^2 + 2z_0^2}\left[r^2 - 2(z^2 - z_0^2)\right].$$

If the applied potential consists of both a DC and an AC voltage

$$U = U_0 - V_0 \cos\Omega t\,,$$

then the equations of motion for a mass m with charge e becomes

$$\ddot{z} = \left(\frac{e}{m}\frac{4U_0}{r_0^2+2z_0^2}\right)z - \left(\frac{e}{m}\frac{4V_0}{r_0+2z_0^2}\right)z\cos\Omega t$$

$$\ddot{x} = -\left(\frac{e}{m}\frac{2U_0}{r_0^2+2z_0^2}\right)x + \left(\frac{e}{m}\frac{2V_0}{r_0^2+2z_0^2}\right)x\cos\Omega t\,,$$

with a y-equation identical to the x-equation. If we define

$$2a_r = -a_z = \frac{16eU_0}{m(r_0^2+2z_0^2)\Omega^2}\,,$$

$$2q_r = -q_z = \frac{8eV_0}{m(r_0^2+2z_0^2)\Omega^2}\,,$$

and $$v = \frac{\Omega t}{2}\,,$$

then both the x- and z-equations of motion are of the form

$$\frac{d^2u}{dv^2} + (a - 2q\cos 2v)\,u = 0.$$

This is the Mathieu equation, which is known to possess well defined regions of the parameters a and q that result in bounded, stable motion[30]. Figure 8 shows the stability diagram obtained by requiring the values of a_z, a_r, q_z, and q_r to be such that the motion is stable in both the axial and radial directions. For an ion of fixed e/m, selection of the trap voltages and frequency locate the operating point on this diagram. Only if the operating point is in the interior of the closed region can trapping occur.

An approximate solution to the equations of motion[31], valid for $q \leqslant .4$ and $a << q$, may be obtained by dividing the motion into a guiding center motion $\bar{u}$ and a micromotion δ:

$$u = \bar{u} + \delta.$$

If we assume that $\delta << \bar{u}$ but $\frac{d\delta}{dt} >> \frac{d\bar{u}}{dt}$, then Mathieu's equation becomes

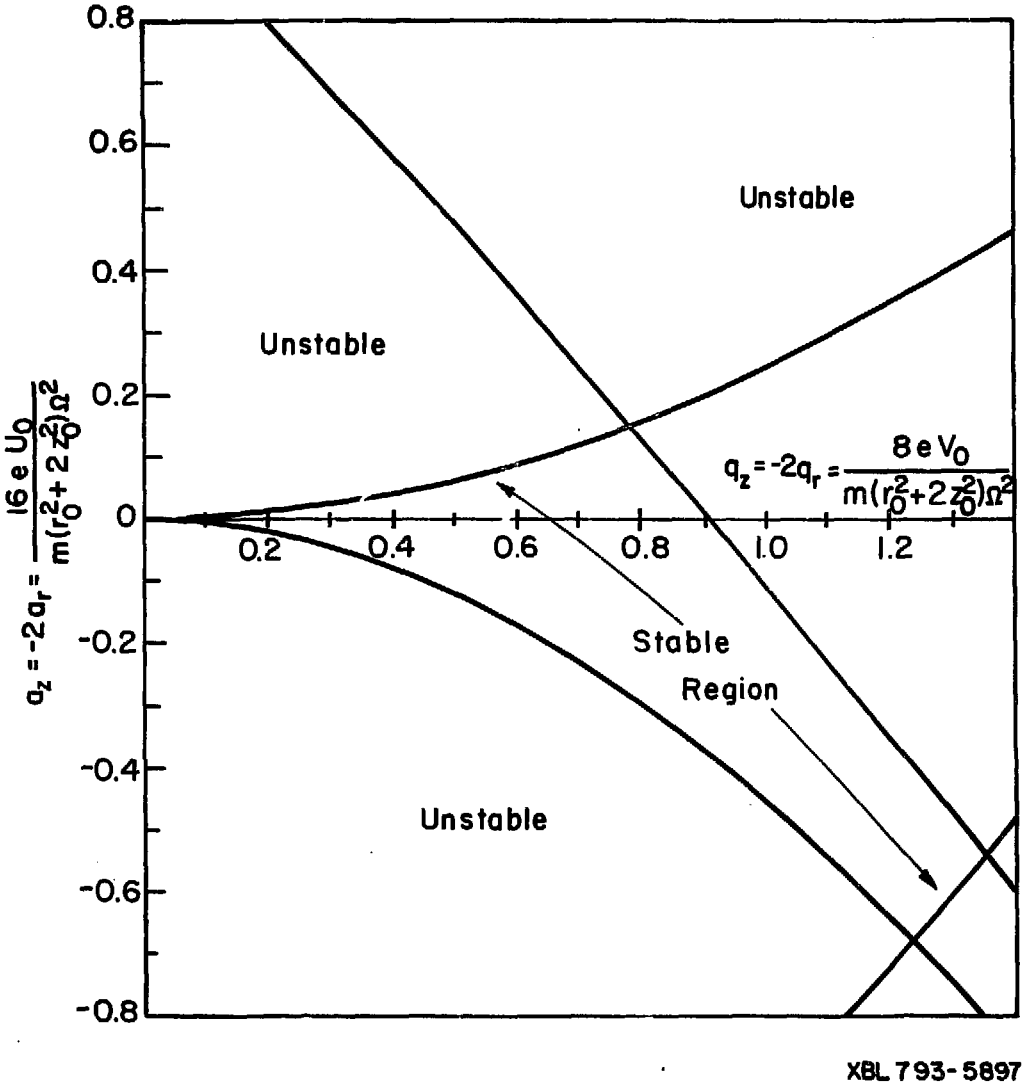


Figure 8. Stability diagram for the RF-quadrupole ion trap.

$$\frac{d^2\delta}{dv^2} = -(a - 2q\cos 2v)\bar{u}.$$

Since $a << q$ and $\bar{u}$ changes slowly, integration gives

$$\delta = -\frac{q\bar{u}}{2}\cos 2v\,.$$

The full equation of motion then can be written

$$\frac{d^2u}{dv^2} = -a\bar{u} + \frac{aq\bar{u}}{2}\cos 2v + 2q\bar{u}\cos 2v - q^2\bar{u}\cos^2 2v\,.$$

Averaging over one cycle of the drive frequency ($0 \leqslant v \leqslant \pi$) gives the equation for the slow micromotion:

$$\frac{d^2\bar{u}}{dv^2} + \left(a + \frac{q^2}{2}\right)\bar{u} = 0.$$

This is a simple harmonic oscillator equation. Changing variables back to t gives the oscillation frequency

$$\omega = \frac{\Omega}{2}\sqrt{a + \frac{q^2}{2}} << \Omega.$$

A reasonable way to picture the ion motion, then, is a slow harmonic motion at frequency ω, upon which is superimposed a small micromotion at the drive frequency Ω:

$$u(t) = A\cos\omega t\left[1 - \frac{q}{2}\cos\Omega t\right].$$

Note that the spectrum of the motion contains components at frequencies $\Omega \pm \omega$, arising from the $\cos\omega t \cdot \cos\Omega t$ term. This is the basis of the ion detection scheme described in the next section.

An alternative approach is to consider the pseudopotential created by the rf-field[32], a method valid for an arbitrary shape of the field. Dividing the motion again into a guiding center motion and a micromotion, the guiding center is found to behave as if in a potential given by

$$\phi_{pseudo} = \frac{e}{4m\Omega^2}\left|\mathbf{E}\right|^2.$$

The total effective potential seen by an ion is then given by

$$\phi_{eff} = \phi_{pseudo} + \phi_{DC}$$

$$= \frac{eV_0^2}{m(r_0^2+2z_0^2)^2\Omega^2}\left[x^2+y^2+4z^2\right] + \frac{U_0}{(r_0^2+2z_0^2)}\left[x^2+y^2-2z^2\right].$$

A constant term has been dropped in order to make $\phi_{eff} = 0$ at the trap center. Potential well depths in the axial and radial directions, defined as the potential differences between the trap edges and the center, are then easily determined to be

$$D_z = \left[\frac{4eV_0^2}{m(r_0^2+2z_0^2)^2\Omega^2} - \frac{2U_0}{(r_0^2+2z_0^2)}\right]z_0^2$$

$$D_r = \left[\frac{eV_0^2}{m(r_0^2+2z_0^2)^2\Omega^2} + \frac{U_0}{(r_0^2+2z_0^2)}\right]r_0^2,$$

which allows the potential to be written as

$$\phi_{eff} = D_r\frac{r^2}{r_0^2} + D_z\frac{z^2}{z_0^2}.$$

The axial macromotion can then be described by the harmonic equation

$$m\ddot{z} + \left[\frac{2eD_z}{z_0^2}\right]z = 0.$$

The oscillation frequency ω_z can be shown to be

$$\omega_z = \frac{\Omega}{2}\sqrt{a_z + \frac{q_z^2}{2}},$$

identical to the result derived above. A similar situation holds for the radial direction.

The optimum trapping parameters have been investigated both theoretically and experimentally. Iffländer and Werth[33] measured the number of ions stored as the trap parameters were varied. Their results, plotted on the stability diagram in Figure 9a, are in good agreement with calculation[34]. For the trap used in this work, a measurement, at fixed $q_z = .43$, of the Li^+ storage time as a_z was varied is shown in Figure 9b. This is a slice across the stability diagram, and the point of maximum stability agrees well with the results of Figure 9a. As a general rule of thumb, for a fixed q_z (or a_z), the value of a_z (or q_z) which results in a spherical potential well will give maximum stability.

A final effect to be considered is the possible influence of a magnetic field. An axial field B $\simeq$ 50 gauss is used in the experiment to keep the ionizing electron beam on the trap

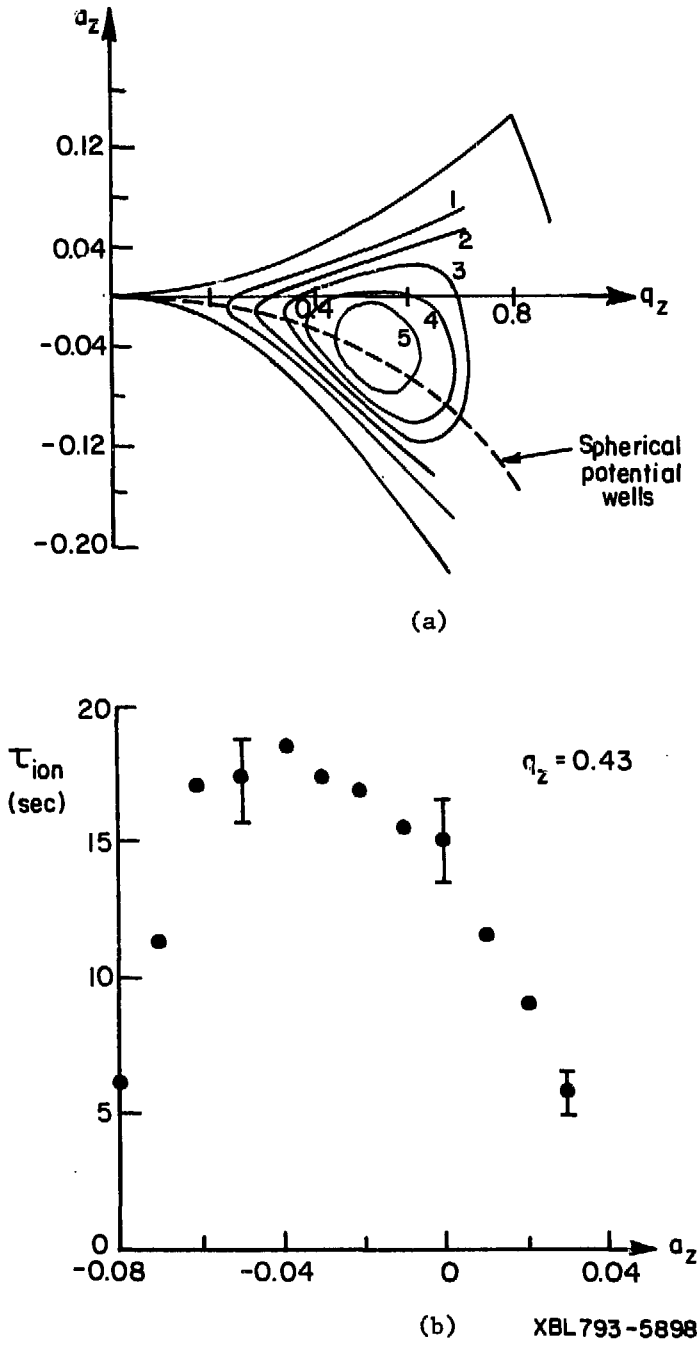


Figure 9. (a) Contours of the number of ions stored. (b) Storage lifetime as a_z is varied across the stability diagram for q_z=.43.

axis. This does not alter the z-equation of motion, but the x- and y-equations become

$$\ddot{x} = -\gamma\left(U_0 - V_0\cos\Omega t\right)x + 2\omega_L\dot{y}$$
$$\ddot{y} = -\gamma\left(U_0 - V_0\cos\Omega t\right)y - 2\omega_L\dot{x}$$

where

$$\gamma = \frac{2e}{m(r_0^2 + 2z_0^2)}$$

and $$\omega_L = \frac{eB}{2mc}$$

is the Larmor frequency. Changing variables to

$$u = x + iy$$
$$v = x - iy$$

uncouples the equations and leads to the Mathieu equation with q_r unchanged but with a new a_r' given by

$$a_r' = a_r + \frac{4\omega_L^2}{\Omega^2} = a_r + \Delta a_r.$$

Thus a magnetic field is equivalent in its affect on ion stability to a shift in the DC potential. For $^7Li^+$ with B $\simeq$ 50 gauss and typical values for the other trap parameters used in this work,

$$\frac{\Delta a_r}{a_r} \cong 5\times10^{-3}.$$

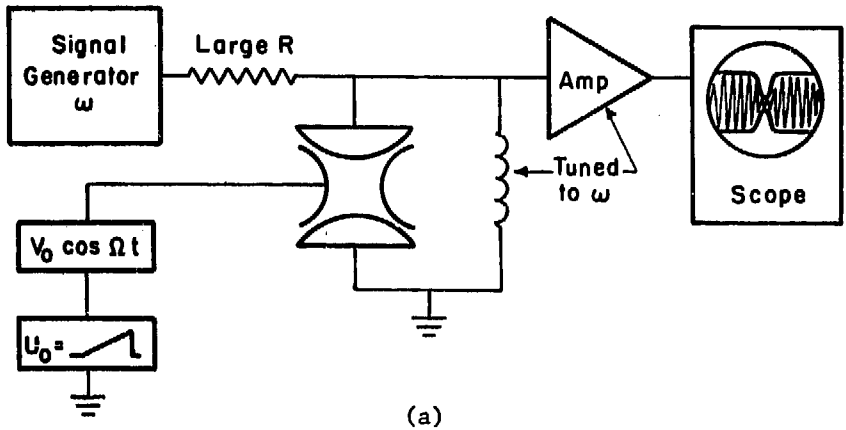
so the magnetic field effect is negligible. This is confirmed by observation, since no field dependent effects were ever noted.

B. THE ION DETECTION SYSTEM

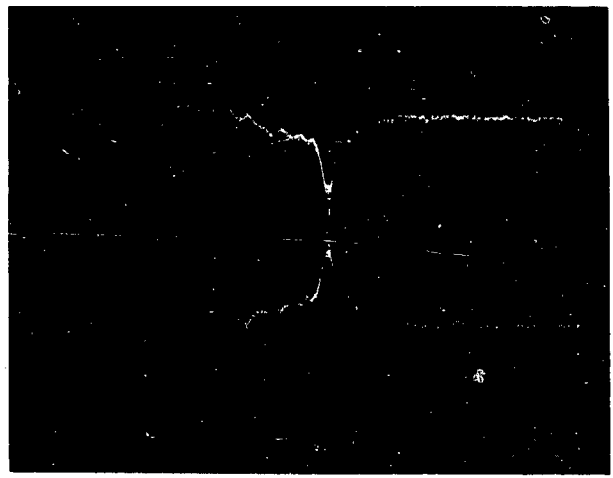
The ability to detect the stored ions is essential for monitoring the performance of the ion trap. Possibly the simplest scheme is to pulse the ions out of the trap and onto a collector of some sort by applying a high voltage to one electrode. Disadvantages of this technique are not only its destructive nature, but also the inability to distinguish various $\frac{e}{m}$ states (except for widely different $\frac{e}{m}$'s which have different times-of-flight). This latter difficulty can be cir-

cumvented by selectively pulsing out one $\frac{e}{m}$ state with resonant excitation, but the inability to measure stored charge nondestructively remains a major drawback. A very elegant method of nondestructive monitoring of a particular $\frac{e}{m}$ is the bolometric technique which has been used with Penning traps[35]. With this method, one essentially measures the excess "noise" produced by the random motion of the ions at their axial oscillation frequency. The primary difficulty of applying this technique to the rf-quadrupole trap is the large amount of rf-background at the drive frequency Ω, which tends to saturate sensitive preamps. While some bolometric measurements have been made of the ion temperature in an rf-trap[46], the author is not aware of any use of this technique for general monitoring of rf-trap ion storage.

A detection scheme which is well suited to rf-traps, and has been adopted for this work, is to detect the axial resonant excitation of a particular $\frac{e}{m}$. The most straightforward way to accomplish this is to apply an rf-excitation at frequency ω_z across the endcap electrodes and observe the power absorbed by the ions[36]. A typical method for performing this measurement is shown in Figure 10a. It was with this technique that we first detected the storage of ions in the trap. An inductance is placed across the capacitor formed by the two endcaps, creating a parallel LC circuit tuned to the frequency ω of an external signal generator. The LC circuit, which has high impedance at ω, is driven by a current source consisting of a large resistor in series with the signal generator. The voltage across the endcaps, which is a measure of the impedance, is detected by an amplifier which is tuned to ω in order to suppress pick-up from the drive frequence Ω. To detect the ions, the trap DC voltage is ramped over a range ~ 5 volts through the particular voltage which brings the ion axial resonant frequency ω_z into resonance with the excitation voltage at ω. As the ions come into resonance, they absorb power from the excitation voltage and effectively reduce the impedance of the LC circuit. This reduces the voltage across the endcaps and causes a momentary dip in the output of the amplifier. A typical oscilloscope trace of an ion signal is shown in Figure 10b. Repeated passage through the resonance shows this method of detection to be nondestructive for low excitation voltages,



(a)



XBB 793-3172

(b)

Figure 10. (a) Ion detection scheme using excitation at ω. (b) Observed ion signal.

although strong excitation can drive the ions out in one pass.

Experimental difficulties with making an automatic measurement of the absorption led to the adoption of a slightly different approach, namely sideband excitation[27]. This effectively removes the carrier frequency at ω and results in a signal whose peak height, which can be easily measured automatically, is proportional to the number of ion present. It was noted in the preceding section that the spectrum of the ion axial motion contains components at the frequencies $\Omega \pm \omega_z$, as well as at ω_z. The effect of exciting the ions with an axial electric field at frequency $\Omega + \omega$ can be seen by using the pseudopotential method, described in the preceding section. Consider for the moment the case $U_0 = 0$ and the application of an axial field at $\Omega + \omega$. The z-component of the total electric field is then

$$E_z = \frac{4V_0}{r_0^2 + 2z_0^2} z\cos\Omega t + E_1\cos(\Omega + \omega)t.$$

To get the z-terms of the pseudopotential we must average E_z^2 over one period of Ω. Since $\omega << \Omega$, then to $O(\omega^2/\Omega^2)$ we can use $<\cos^2\Omega t> = <\cos^2(\Omega + \omega)t>$. We also note that $\omega_z = q_z\Omega/2\sqrt{2}$ since $a_z = 0$. The pseudopotential then becomes

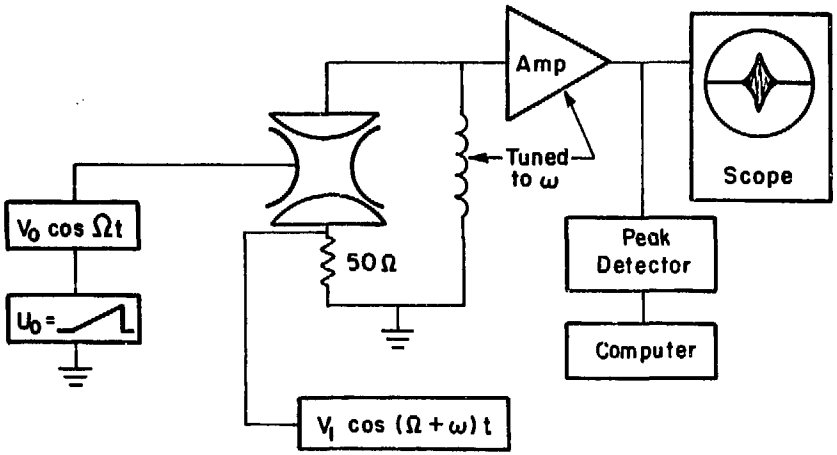
$$\phi_{pseudo} = D_z\frac{z^2}{z_0^2} + \frac{\omega_z}{\sqrt{2}\Omega}E_1 z\cos\omega t + \text{constant},$$

which gives the axial macromotion equation

$$\ddot{z} + \omega_z^2 z = -\frac{e}{m}\left(\frac{\omega_z}{\sqrt{2}\Omega}\right)E_1\cos\omega t.$$

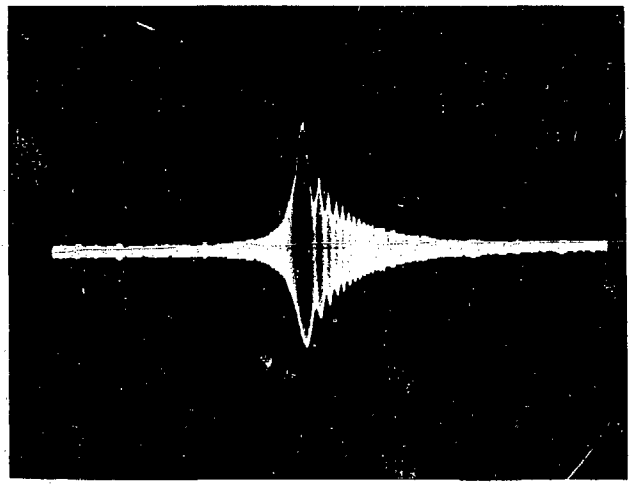
Excitation at the sideband frequency $\Omega + \omega$ is thus seen to be equivalent to excitation at ω with the amplitude reduced by the factor $\frac{\omega_z}{\sqrt{2}\Omega}$. The advantage is that the ion motion can now be detected at frequency ω without the addition of a carrier.

A scheme for performing this measurement is shown in Figure 11a. The excitation signal is applied across the endcaps and so is not purely an axial field, but since the radial extent of the ion cloud is small (see next section), the approximation of an axial field is good. Ramping the trap potential through the resonance $\omega_z = \omega$ and the use of a tuned circuit and amplifier is the same as for the previous detector. The signal, shown in Figure 11b, can be displayed on



(a)

XBL 793-5849



XBB 793-3171

(b)

Figure 11. (a) Ion detection scheme for excitation at the sideband $\Omega + \omega$. (b) Observed ion signal.

the oscilloscope and simultaneously measured by a peak-detector circuit. Electronic details are discussed in the next chapter.

It is of interest to relate the signal seen to the number of ions present. For excitation which is rapid compared to any relaxation process, the ion cloud moves coherently as a charge $Q = Ne$. For charge moving between the plates of a parallel plate capacitor (separation $2z_0$), the image current induced, neglecting end effects, is

$$i = \frac{Q}{2z_0}\frac{dz}{dt} = \frac{Ne}{2z_0} A\omega_z \cos\omega_z t$$

where A is the amplitude of the ion cloud's oscillation. On resonance, the LC circuit consisting of the trap electrodes and the inductor has an impedance R which is purely resistive. A voltage iR is developed across it and amplified for detection. Its maximum possible amplitude for strong excitation is when $A = z_0$, so the signal seen in that case is

$$S = \frac{NeR\omega_z G}{2},$$

where G is the detector gain. A determination of R and G allows the number of ions to be measured. A rough measurement for a detector used early in this experiment to observe N^+ ions created from the background gas indicated that typically

$$N_{\max} \sim 3 \times 10^5 \text{ ions.}$$

This value is consistent with the known ionizing electron beam current, assumimg production cross sections $\sigma \cong 10^{-16}\,\text{cm}^{-2}$. In general, however, the ions were excited rather weakly in order to obtain a nondestructive signal whose peak value was a relative ion signal which could be used for day-to-day monitoring as well as for measuring the ion storage times.

A final point of interest concerning ion detection is the rather unusual ion signal envelope observed, as seen in Figures 10b and 11b. Qualitatively, this behavior can be understood in a simple way. By ramping the DC trapping voltage, the ion's axial frequency becomes

$$\omega_z^2(t) = \omega_0^2 + \alpha t\,.$$

The equation of motion of the ion cloud in the presence of an excitation at frequency ω is then

$$\ddot{z} + 2\eta\dot{z} + (\omega_0^2 + \alpha t)z = A\cos\omega t,$$

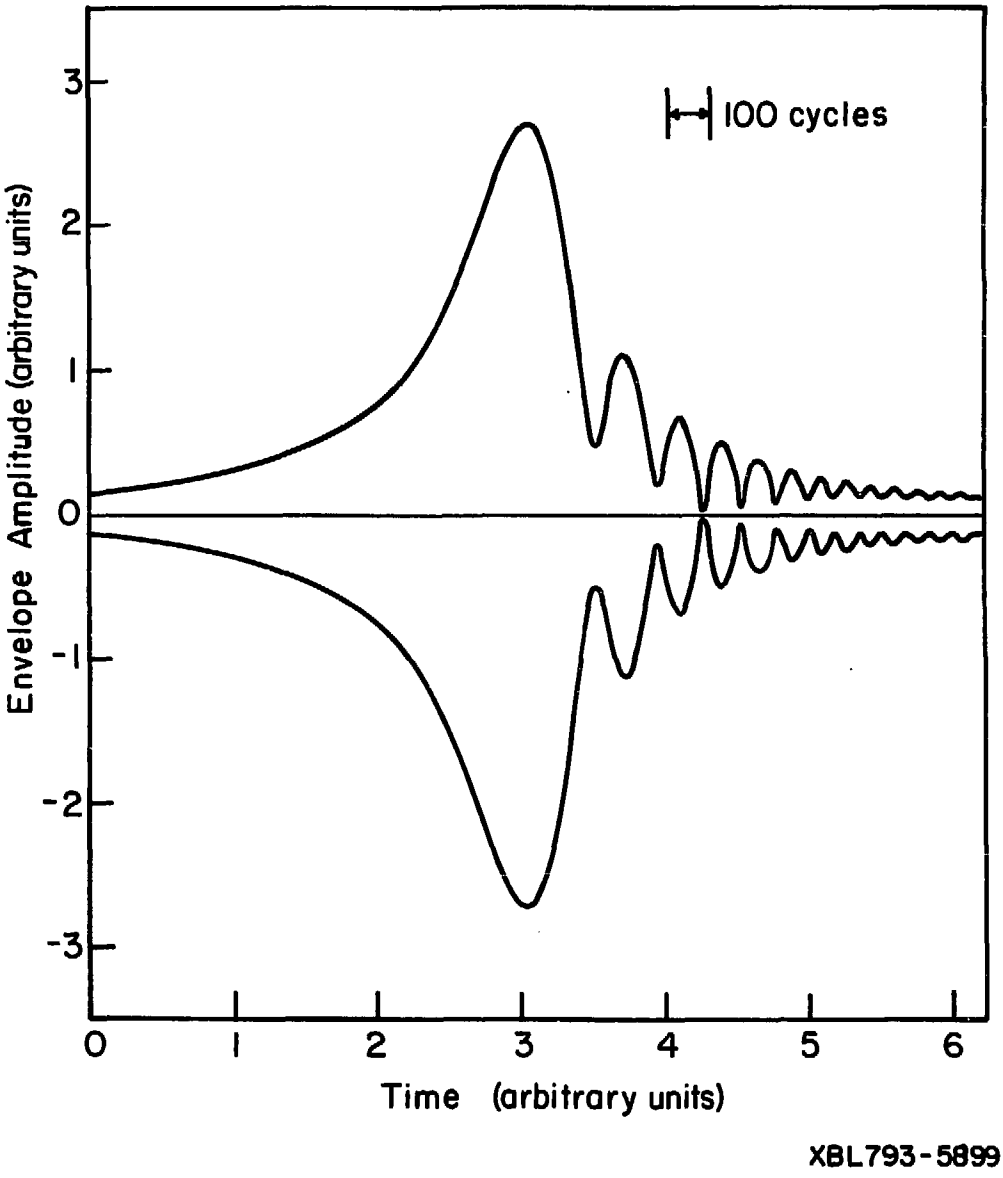


Figure 12. Computer solution for the envelope of a time-varying forced harmonic oscillator.

where η provides a weak damping to describe, at least qualitatively, the relaxation of the ion cloud and its subsequent loss of coherent motion. At any instant of time, the solution of this equation can be written as the sum of a homogeneous solution, oscillating at $\omega_z(t)$, and a particular solution, oscillating at ω. Initially ($t = 0$) the homogeneous solution is negligible, and the ions simply follow the excitation. But upon passing through resonance, $\omega_z(t_0) = \omega$, a large amount of energy is supplied to the ions. Shortly thereafter, at $t = t_0 + \delta t$, the homogeneous solution and the particular solution are both large. But $\omega_z(t_0+\delta t) \neq \omega$, so two slightly different frequencies are present and beats occur between them. As t continues to increase, the beat frequency becomes larger while simultaneously the damping term $e^{-\eta t}$ reduces the homogeneous solution. To verify this description, computer generated solutions to the equations of motion were obtained. Figure 12 exhibits a typical case, where just the envelope of the rapid oscillations is shown. The similarity with the observed ion signal envelope is quite good and justifies the simple description given here.

C. ION TRAP PERFORMANCE

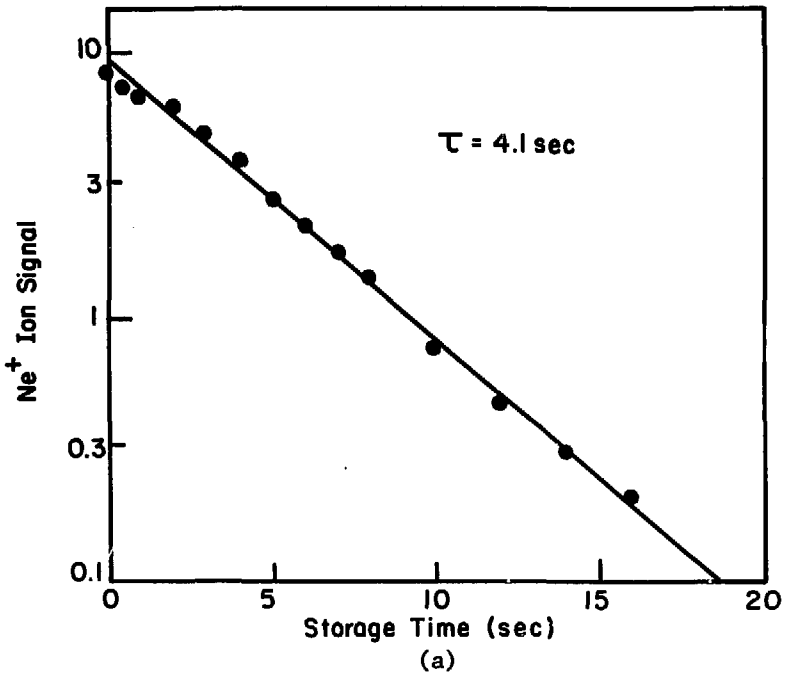
1. Ion Storage

The discussion up to this point has been very general, applicable to all rf-quadrupole traps. It is useful now to consider the particular trap used in this experiment. Table 3 lists the major trap parameters for the configuration used with Li^+ ions; the values used with ions created from the background gas do not differ substantially. Many of the details are described more fully in the next chapter.

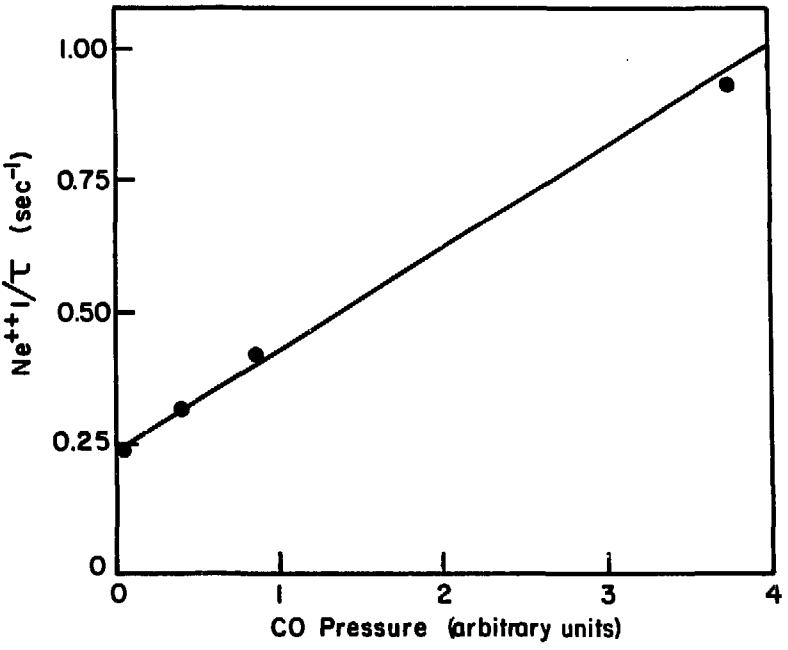
The initial testing of the trap utilized ions formed either from the residual background gas or from a particular target gas which was admitted through a leak valve. Figure 13 shows data obtained during a study of neon. Part a shows the decay of Ne^+ ions at a background gas (mostly neon) pressure of 2.5×10^{-8} torr. The signal was followed for four lifetimes and shows only minimal deviations from an exponential decay . Part b shows the

Table 3. RF-Quadrupole Ion Trap Parameters

Axial dimension	$z_0 = 3.0$ cm
Radial dimension	$r_0 = 3.0$ cm
Drive frequency	$\Omega = 2\pi \times 1.0$ MHz
AC drive amplitude	$V_0 = 250 - 400$ volts
DC drive amplitude	$U_0 = 0 - 30$ volts
Spherical well depth	$D = 8 - 18$ volts
Detection frequency	$\omega = 2\pi \times 100$ KHz
Detection ramp voltage	$\Delta U = 10$ volts in 200 msec
Electron current	$i_e = 10 - 30$ μamp
Electron energy	$E_e = 250 - 500$ volts
Electron pulse duration	$T_e = 1 - 2$ sec
Background pressure	$P \simeq 1 \times 10^{-9}$ torr
Total ions stored	$N \simeq 2 \times 10^5$
Metastable ions stored	$N^* \simeq 2 \times 10^4$
Ion cloud radius	$\Delta \simeq .6$ cm
Ion storage lifetime	$\tau = 15 - 30$ sec

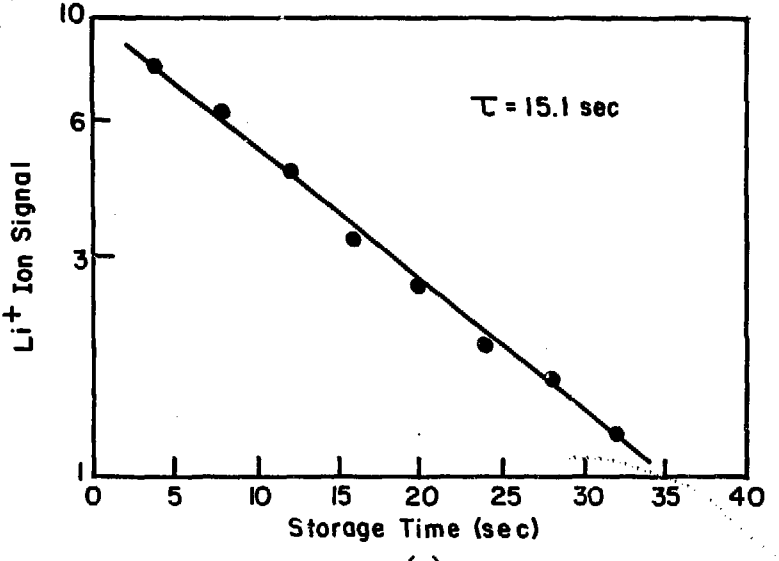


(a)



(b) XBL793-5900

Figure 13. (a) Ion signal decay of Ne^+. (b) Variation of the Ne^{++} loss rate as the background CO pressure is changed.



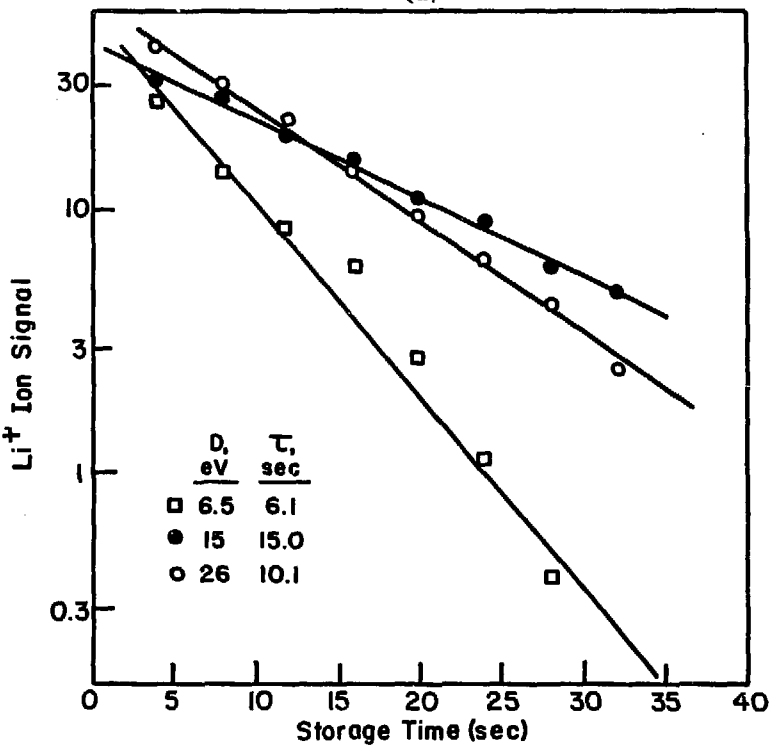


Figure 14. (a) Ion signal decay of Li^+. (b) Li^+ ion signal decay for potential well depths of 6.5, 15, and 26 eV.

variation of the Ne^{++} storage time as CO is admitted into the background. The loss rate varies linearly with the CO pressure, the expected behavior for loss mechanisms dominated by ion-background collisions.

Typical data for Li^+ is shown in Figure 14. A decay curve exhibiting very good exponential behavior is depicted in 14a. In 14b, the storage time is seen to depend on the depth of a spherical potential well. It was observed in Figure 9 that a spherical well provides maximum stability. Here we see that a well which is too shallow allows the ions to leak out, and that a very deep well also has increased losses, possibly due to strong rf-heating. Most data for the radiative lifetime were taken using a spherical well with $8 \leqslant D \leqslant 18$ volts.

A detailed understanding of the ion behavior in the trap requires a knowledge of the time scales involved for processes such as collisions or relaxation. Figure 15 describes a measurement of the relaxation in Li^+ ions. The trap DC potential was quickly shifted directly to the value which brought the ions into resonance with a weak excitation. After a few msec (a time short enough to prevent any ion loss), the excitation was abruptly switched off, allowing the ion signal to be observed as it decayed due to relaxation. Over a reasonably wide range of excitation times and amplitudes, the relaxation time was found to be

$$\tau_{relax} \cong 30 \text{ msec.}$$

Very strong excitation tended to increase τ_{relax} somewhat. We can use this value to determine the Q of the ions:

$$Q = \frac{\omega \tau_{relax}}{2} \cong 10^4.$$

This is approximately the number of oscillations which the entire ion cloud undergoes before any appreciable loss of coherence occurs. We can now estimate that after any disturbance of the ion cloud, such as its creation, it will relax to its quasi-equilibrium state in a time $t \sim \tau_{relax}$.

Collisional processes which are likely to affect the ions include both ion-ion and ion-neutral encounters. Ion-neutral elastic scattering is predominantly due to the interaction of the ion with permanent and induced dipole moments of the neutral. For the case of induced moments, the time between collisions can be estimated to be[27]

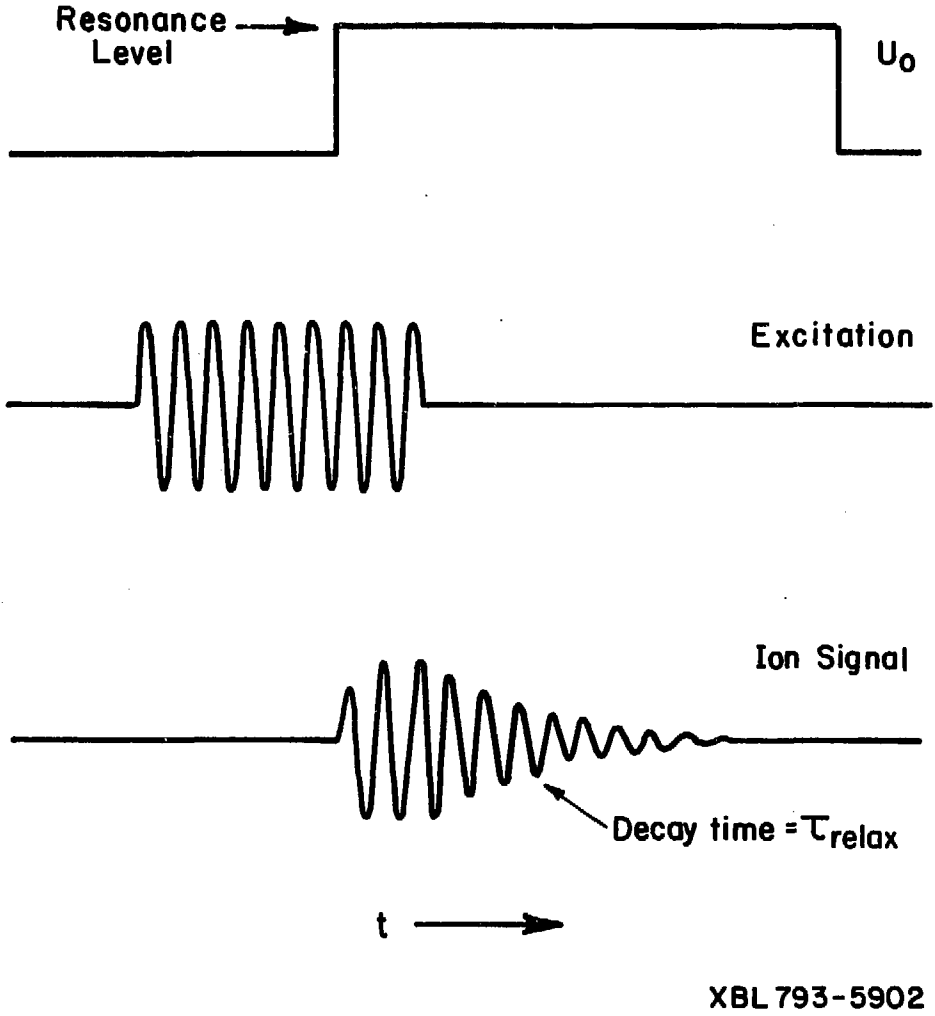


Figure 15. Time variation of the trap DC potential and the side-band excitation used to observe the ion relaxation.

$$T_{ion-neutral} \cong \frac{\sqrt{m/\alpha}}{2\pi en},$$

where n, α, and m are the density, polarizability, and mass of the neutral. For H_2 at a pressure of 1×10^{-9} torr, this gives $T_{ion-neutral} \cong 7$ sec, a major fraction of the total ion storage lifetime. Molecules with permanent dipole moments should not have significantly different collision times.

Ion-ion collision times can be roughly estimated on the basis of formulas derived for uniform plasmas[37]:

$$T_{ion-ion} \cong 4.1 \times 10^{10} A^{1/2} \left(\frac{kT}{e}\right)^{3/2} n^{-1} Z^4 (\ln \Lambda)^{-1},$$

where A and Z are the atomic weight and ionic charge, n the ion density, and $\Lambda = \frac{r_{max}}{r_{min}}$ is the ratio of the cutoff distance for the Coulomb interaction to that of closest approach. Since the dependence on Λ is not large, we can use $r_{max} = r_0$ and determine $r_{min} \cong 20\text{Å}$ from energy conservation, giving $\ln \Lambda = 16$. For $n = 5 \times 10^5$ and $T = 5000$ K, typical values for the ion trap, we find

$$T_{ion-ion} \cong .7 \text{ sec.}$$

These values present somewhat of a puzzle. Both ion-ion and ion-neutral collisions appear to be too infrequent to explain either the observed relaxation or storage times. The relaxation time, $\tau_{relax} \cong 30$ msec, is not too disturbing since the observed $Q \cong 10^4$ implies that the responsible process is very weak. This could be accomplished by slight anharmonicities in the effective potential which destroy the ion cloud's coherence without causing major alterations in the ion trajectories. The slow loss of ions from the trap, on the other hand, is generally considered to be due to a diffusion process involving many collisions. In this case, one can consider "hot" ions in the Boltzmann tail to be lost by "evaporation" when their energy becomes sufficient to strike an electrode. The estimated $T_{ion-neutral} \cong 7$ sec $\cong \frac{1}{2} T_{storage}$ clearly cannot provide the necessary number of collisions. That ion-ion collisions, though an order of magnitude more frequent, are not responsible is seen both by the existence of exponential

decays, which would not be the case for ion-ion induced loss, and by the fact that the ion distribution measurements, described below, are independent of the total ion number.

An alternative explanation is that the ions are lost in a single, large cross section event, e.g. charge exchange or a chemical reaction. (Additional processes affect the loss of metastable ions only and are responsible for the nonradiative quenching, discussed in Section VI.C.) Such events are known to occasionally have $\sigma \geqslant 10^{-14}$ cm^2, which is sufficiently large to provide the observed loss rate. Evidence for this explanation is presented in Figure 16, where the ion loss rate is plotted against the pressure of three typical residual gases. The loss rate clearly does not depend significantly on the CH_4 pressure, and there is even vague evidence that increased H_2, since it is lighter than Li, improves the storage, an effect previously observed for Hg^+ ions with a He buffer gas[27]. But the loss rate does indeed depend on the CO_2 pressure. Other measurements have shown a similar pattern for CO. This is reasonably good evidence that the ion loss is basically due to selective interaction with specific components of the residual gas.

2. Ion Distribution

To complete our understanding of the ion trap, we must inquire as to how the ions are distributed within the trap, what their temperature is, and how these are affected by space-charge. This information is particularly useful in the optical pumping model described in Appendix A. To investigate these questions, we made a detailed study of the ion distribution for various trapping parameters[38]. The laser scanning method and other details are presented in Appendix B; only the general results will be described here.

We find that for an ellipsoidal effective potential

$$\phi_{eff} = D_r \frac{r^2}{r_0^2} + D_z \frac{z^2}{z_0^2},$$

the ions have the Gaussian distribution function

$$n(r,z) = \frac{N}{r_0^2 z_0} \left[\frac{e^3 D_r^2 D_z}{(\pi kT)^3}\right]^{1/2} \exp\left[-(\frac{r}{\Delta_r})^2 - (\frac{z}{\Delta_z})^2\right]$$

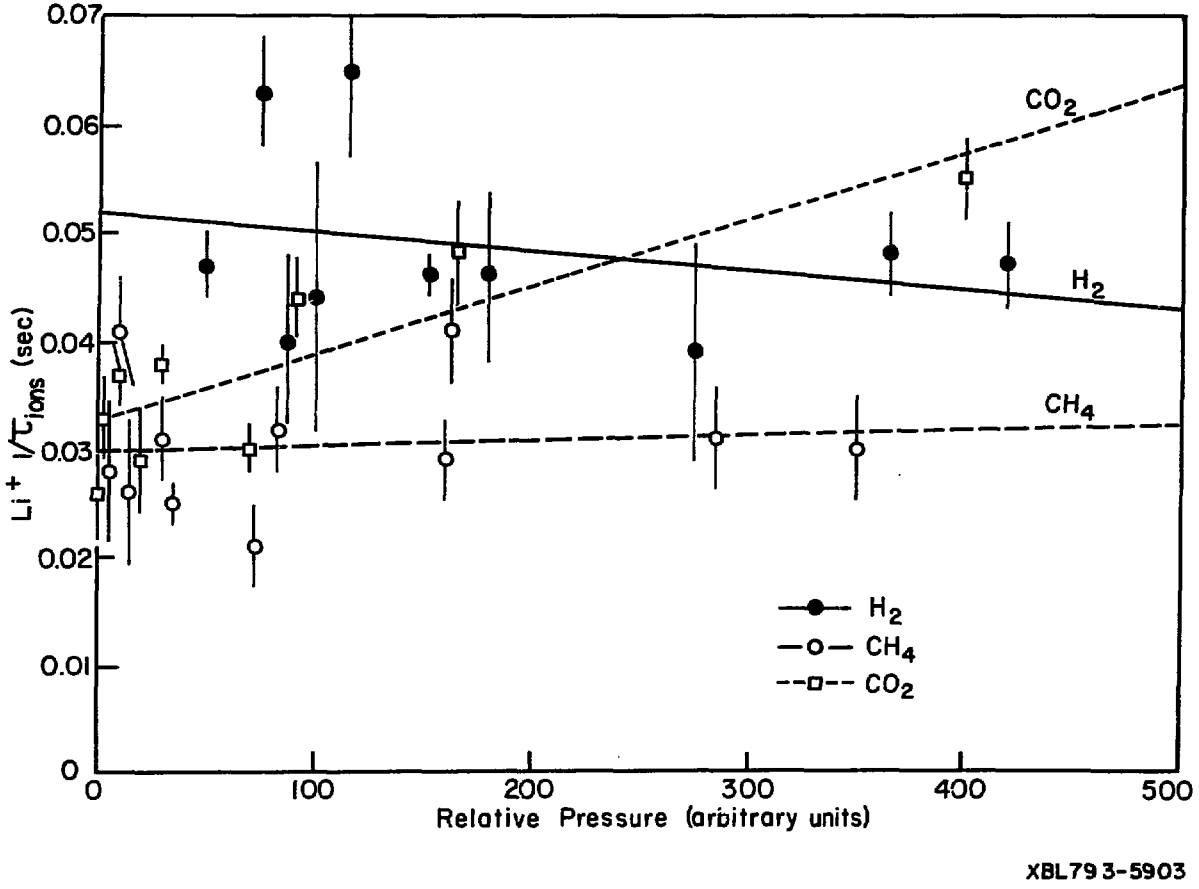


Figure 16. Li^+ storage loss rate as the residual gas is varied.

where

$$\Delta_r = r_0\sqrt{\frac{kT}{eD_r}}$$

and

$$\Delta_z = z_0\sqrt{\frac{kT}{eD_r}}.$$

For a spherical well, our measured values for the ion cloud radius Δ as a function of the well depth D are shown in Figure 17. The x's are an independent measurement made by comparing the $2\,^3S_1$ - $2\,^3P_1$ lineshapes with the results of the optical pumping model. From the measured values of Δ_r we can extract the ion temperature

$$T \cong 5000 \text{ K}.$$

This is substantially higher than the residual gas at room temperature, and apparently is maintained through strong rf-heating effects during collisions.

There have been various attempts[39] to model the complicated processes occuring in an rf-quadrupole ion trap, and they have succeeded in showing that if one neglects space-charge effects, then indeed the ions have a Maxwellian velocity distribution, and hence a well-defined temperature, and that the spatial distribution is Gaussian. We can obtain a better understanding, however, if we make a simple model with the *a priori* assumption that the ions can be described by a quasi-equilibrium at temperature T. Then the ions, seeing the trap potential plus a space-charge potential

$$\phi = D\frac{r^2}{r_0^2} + \phi_{sp.ch.},$$

obey a canonical distribution

$$dn = Ce^{-E/kT}d^3pd^3r$$

which is integrated over momentum space to give

$$n = K\exp\left[-\frac{r^2}{\Delta^2} - \frac{e\phi_{sp.ch.}}{kT}\right].$$

Poisson's equation for the density is

$$\nabla^2\phi_{sp.ch.} = -4\pi en = -4\pi eK\exp\left[-\frac{r^2}{\Delta^2} - \frac{e\phi_{sp.ch.}}{kT}\right].$$

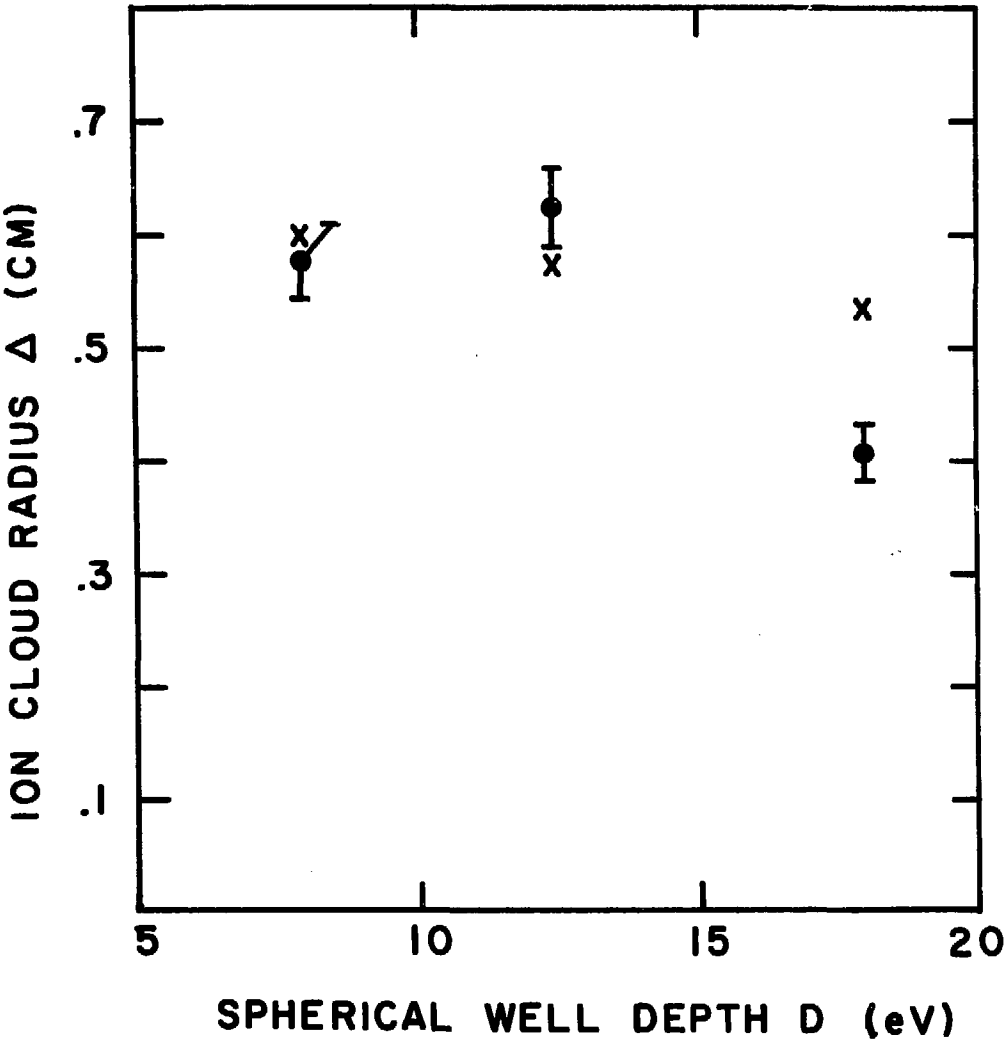


Figure 17. The ion cloud radius for three different spherical wells, measured by laser scanning (•) and by the $2^3S_1 - 2^3P_1$ linewidth (×).

Because of the spherical symmetry, this becomes an ordinary second-order differential equation which is easily solved numerically for a given temperature T. Results for parameters typical of this experiment are given in Figure 18. At $T = 0$, the ion cloud becomes a constant density sphere with the space-charge repulsion exactly balancing the trap potential well. As T increases, the sharp edge dissolves until, at $T \geqslant 10^3$ K, the ion cloud becomes approximately Gaussian (negligible space-charge effects) with $\Delta = .5$ cm, consistent with our observations.

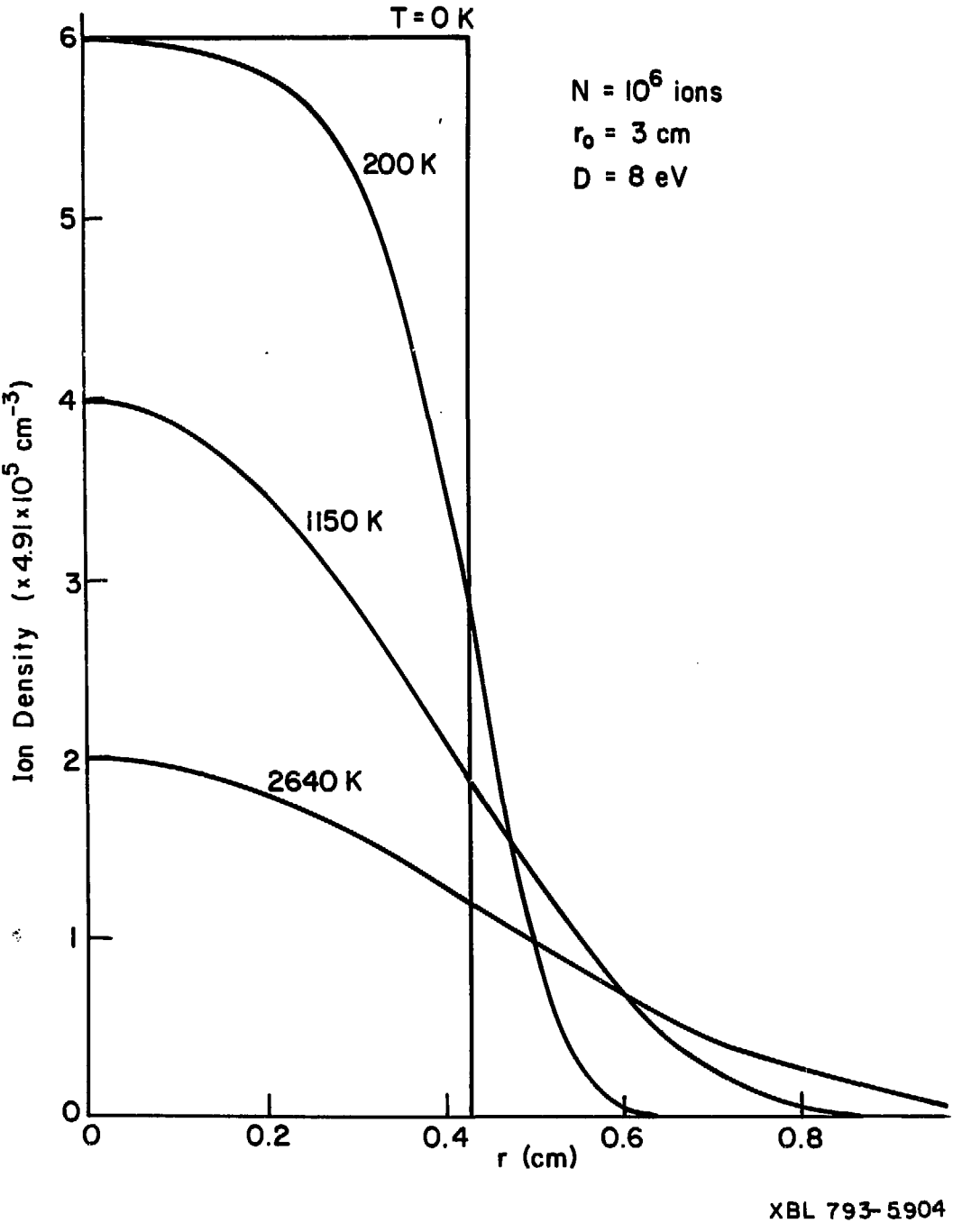


Figure 18. Ion density distribution for various ion temperatures.

V. EXPERIMENTAL METHODS

This chapter will consider, in some detail, the many separate experimental requirements for measuring the $2\,^3S_1$ radiative lifetime. The final section will describe how the diverse parts are simultaneously controlled by the computer. Details of the data accumulated are discussed in the next chapter. A block diagram of the entire experiment is shown in Figure 19.

A. THE VACUUM SYSTEM

The ability to produce and maintain an ultrahigh vacuum is an essential step for obtaining storage times of many seconds. An early decision to use a stainless steel system with oil diffusion pumps was made in order to utilize as much existing equipment as possible. While ion pumps or cryo pumps would likely have produced a lower ultimate pressure, the diffusion pumped system has been adequate. A diagram of the vacuum system is shown in Figure 20.

The division into three separate chambers was made to accommodate relatively high oven chamber pressures without degrading the pressure in the main chamber. The buffer chamber, which is blocked at both ends by stainless steel collimating disks with 1/8 inch diameter holes, has a baffled 2 inch CVC diffusion pump with an effective pumping speed $\simeq$50 l/sec. The oven chamber is pumped by a 700 l/sec 4 inch CVC pump, whose effective speed is roughly halved by a baffle which consists of a copper plate with water-cooled coils soldered onto the back. A manually operated gate valve separates the oven chamber from the rest of the system and allows the Li oven to be reloaded without having to let the entire system up to air. The oven chamber pressure, measured by a Veeco ion gauge, quickly drops to $\sim 10^{-5}$ torr after the Li oven is loaded. After several hours of running the oven, the pressure drops to $\sim 1 \times 10^{-6}$

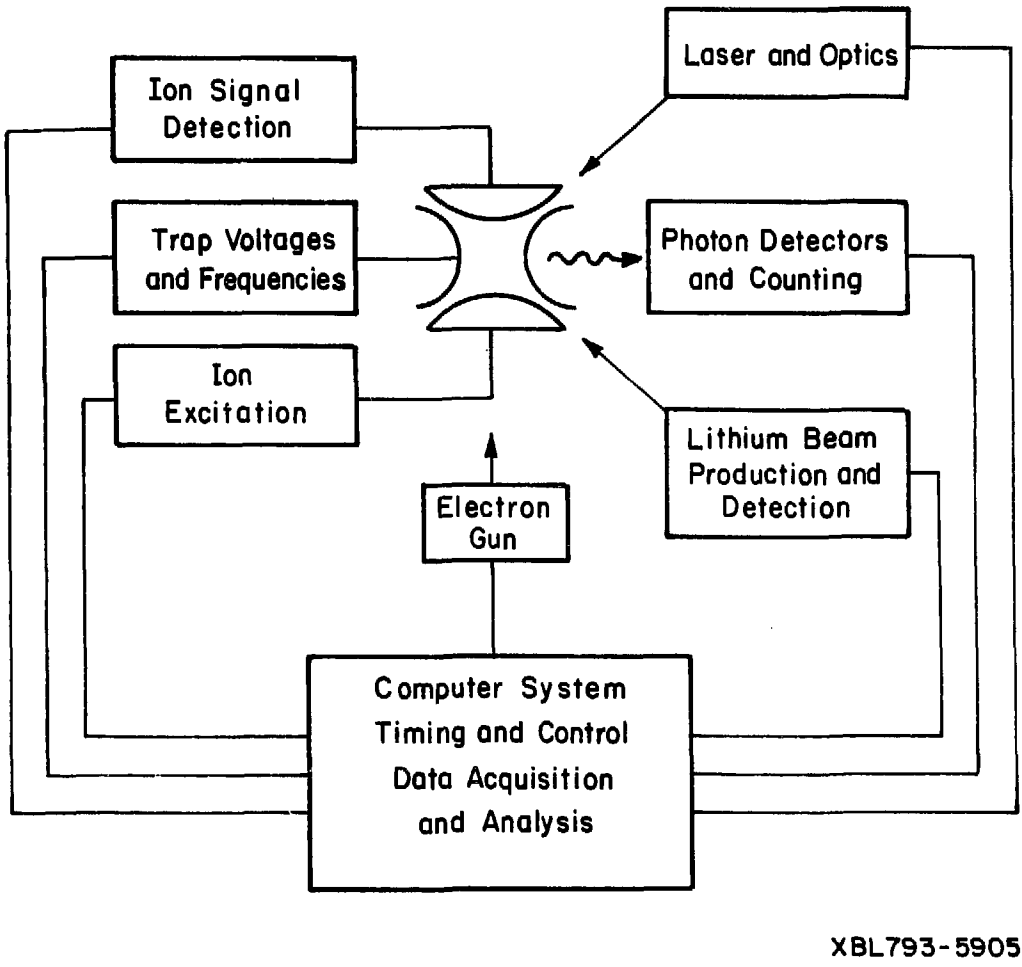


Figure 19. Block diagram of the Li^+ 2^3S_1 lifetime experiment.

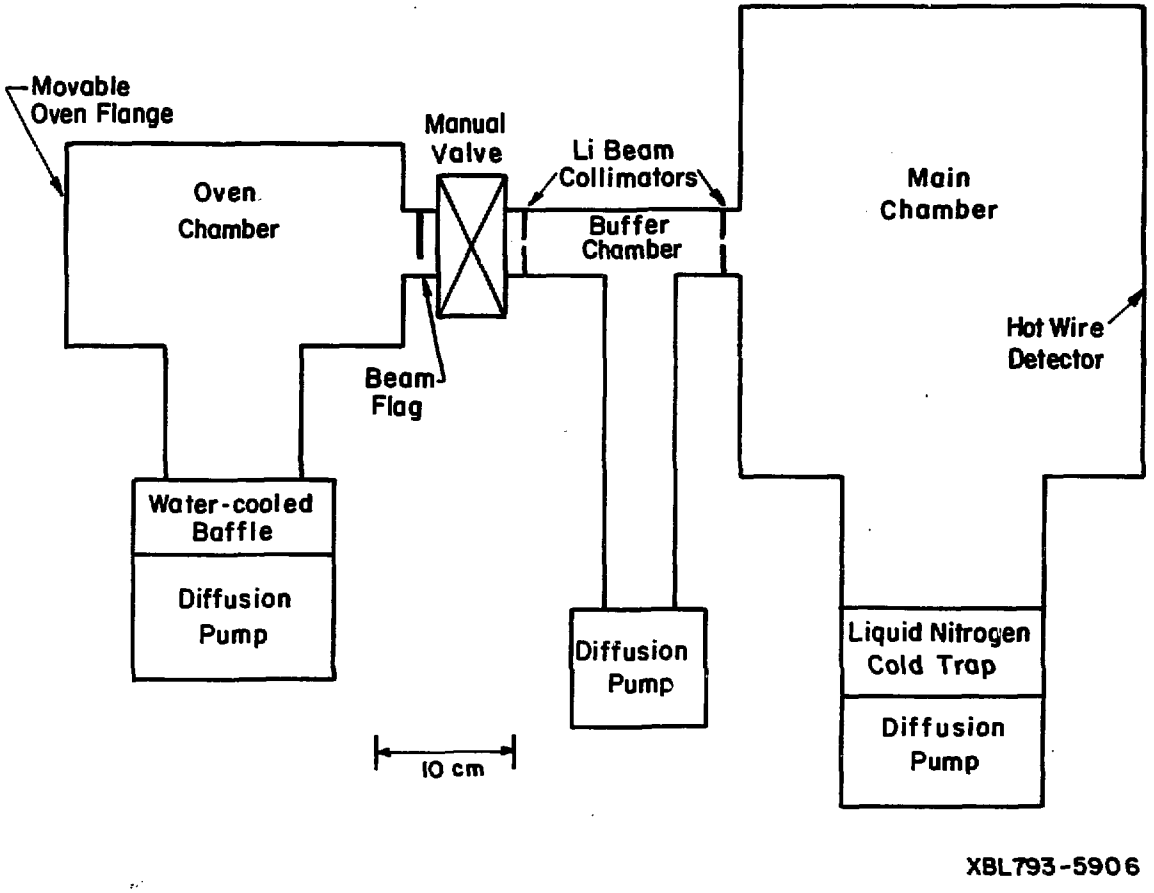


Figure 20. The vacuum system. The scale indicator is meant to provide only a rough guide.

torr and stabilizes, a value low enough to have negligible effect on the main chamber. Roughly every 200 hours of oven operation requires emersion of the oven chamber in water to remove Li deposits, and periodic pump cleaning is necessitated by the buildup of Li and Li-compounds in the oil.

The main chamber, where the pressure is critical, is pumped by a 1200 l/sec 4 inch NRC diffusion pump, baffled by a circular chevron cold trap which cuts the pumping speed by half. The cold trap is kept continuously full of liquid nitrogen by an automatic filling system. The pressure is measured by a Varian nude ion gauge which is mounted on the top flange of the system. Also attached to the system are an EAI quadrupole mass spectrometer, used to determine the residual gas composition, and a Granville-Phillips leak valve, which can admit trace quantities of gases for study.

The maxim "cleanliness is next to Godliness" is certainly true in the production of ultrahigh vacuums. The materials used in the construction of the ion trap, the photon detectors, and the necessary supports are copper, stainless steel, tantalum, and ceramic. The surfaces of the copper are cleaned in a bright-dip solution, consisting primarily of nitric acid. All screws in blind tapped holes are either slotted or drilled axially to minimize virtual leaks. Electrical connections are either mechanical or spot welded. Cotton gloves were worn during the final assembly of all parts, which were previously cleaned with acetone in an ultrasonic cleaner and then rinsed in trichloroethylene.

Oil backstreaming from the mechanical pumps during pumpdown is minimized by both a liquid nitrogen trap and a molecular sieve trap in the foreline. When a pressure $\simeq 10$ microns is reached, the diffusion pump cold trap is briefly cooled to stop the initial backstreaming and the pump is turned on. Pumping for several hours brings the pressure down to $5-10\times10^{-8}$ torr, at which time the cold trap can be filled and a pressure of $1-2\times10^{-8}$ torr reached.

Further pressure reduction requires baking the system. This is accomplished with an oven consisting of resistive heating elements mounted inside of an enclosure built of 1 inch

thick Maronite, an asbestos product. The oven is lowered over the main chamber, which is resting on a Maronite base, and heating tapes are wrapped around the cold trap and the buffer chamber. The system is baked at $\simeq$250°C for 5 - 7 days, then allowed to cool slowly to nearly room temperature before the cold trap is filled. This generally results in an ultimate pressure of $5-10\times10^{-10}$ torr which is fairly stable for a few weeks, but ultimately creeps up to $3-5\times10^{-9}$ torr if the system is not rebaked.

B. THE LI OVEN AND HOT WIRE DETECTOR

The creation of lithium ions is accomplished by passing a rather large ($\simeq$1/8 inch diameter) Li beam through the center of the ion trap, where it is intersected by an ionizing electron beam. The Li beam, after exiting the trap, strikes a hot wire detector which, by surface ionization, produces a current proportional to the beam flux. The beam is well defined by passing it through two 1/8 inch diameter collimators in the buffer chamber, and a computer-controlled solenoid-activated beam flag located in front of the oven allows the beam to be turned on and off automatically. The alignment, which is not crucial due to the large beam size, of the collimators, the ion trap center, and the hot wire detector is performed with a He-Ne laser. The oven itself, which is mounted on a movable flange, has its position optimized by maximizing the hot wire current.

Two separate resistive-heated ovens, shown in Figure 21a, have been used during this experiment. The first consisted of a thin-walled stainless steel crucible, clamped between heavy copper leads, through which an AC heating current of $\simeq$150 amps was passed directly. A 1/4 inch wide nozzle packed with $\simeq$1/4 inch long hypodermic needles provided a reasonably well directed beam. Though used for over a year, this oven had several drawbacks. The most serious were the heat loss to the copper leads, the corrosion of the crucible at the steel-copper connection, and the seepage of Li through the crucible flange which limited the lifetime of an $\simeq$1/4 gram load to $\leqslant$ 20 hours. The second oven eliminates these problems by using indirect

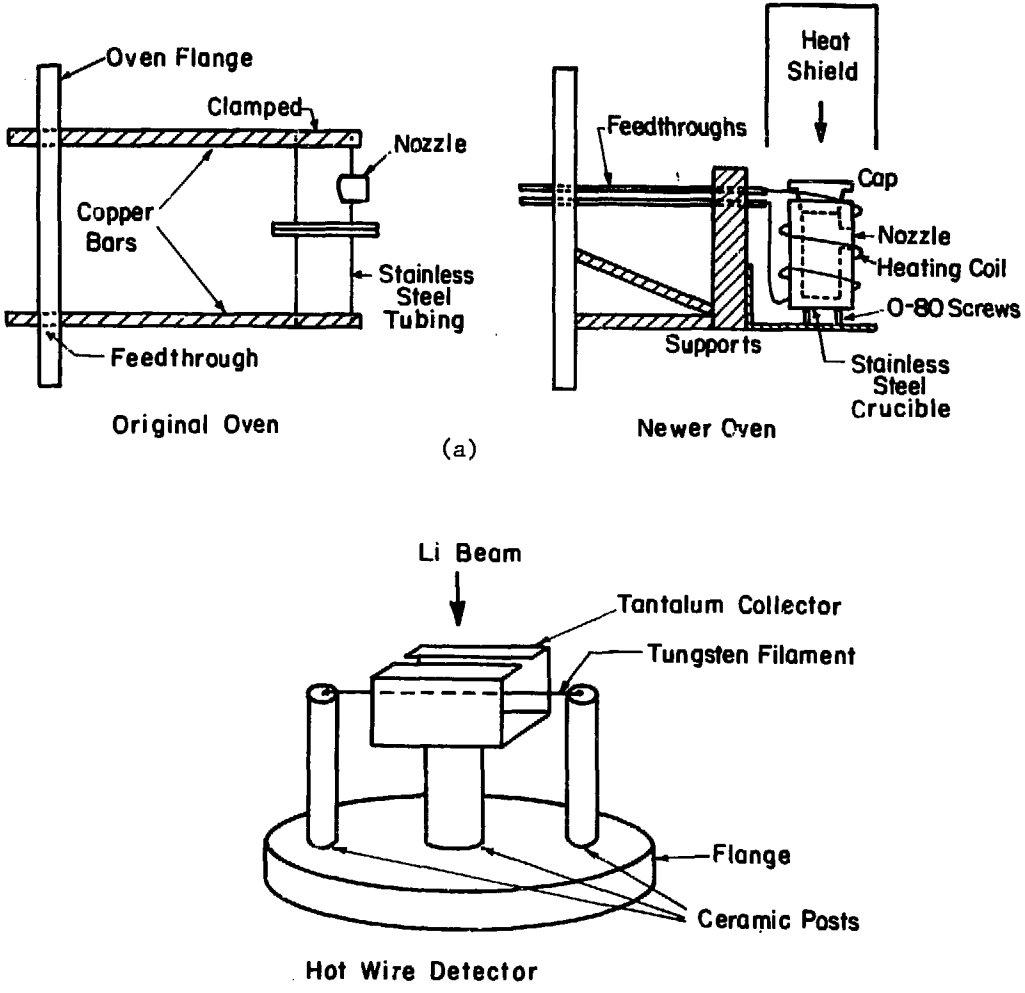


Figure 21. (a) The lithium ovens used in the experiment. (b) The lithium beam hot wire detector (electrical connections not shown).

heating, with a heating coil of 20 mil tantalum wire, of a stainless steel crucible with minimal heat conductivity to its support. The crucible is well sealed by a tight-fitting cap which is pressed in using a vise, and a hypodermic needle nozzle is again used. A tantalum heat shield is placed around the crucible and heating coil in order to minimize radiation losses to the walls. This oven, which requires $\simeq$120 watts of power, has worked well, with each oven load lasting $\simeq$60 hours.

The hot wire detector, shown in Figure 21b, consists of a 3 mil tungsten filament surrounded by a tantalum collection electrode. The filament is heated by $\simeq$3/4 amp and is biased at +20 volts in order to drive the Li ions onto the collector, whose output is routed directly to a picoammeter. Since the ionization efficiency is near 100% for Li atoms striking the wire, an estimate of the Li beam density can be made. The ion trap is reasonably well filled in a one second period when the Li oven is run near 600°C, the Li vapor pressure then being $\simeq$.1 torr. At this temperature, the hot wire detector records $\simeq 3 \times 10^{-10}$ amp current, corresponding to $\simeq 2 \times 10^{9}$ ions/sec. The ratio of the area presented by the filament to the cross section $A = .10$ cm^2 of the entire beam is $\simeq$1/40, so the beam intensity must be $I = 8 \times 10^{10}$ atoms/sec. At T = 600°C the beam velocity is $v \cong 10^5$ cm/sec, which leads to an estimate for the beam density of

$$n_L = \frac{I}{Av} \cong 8 \times 10^6 \text{ cm}^{-3}.$$

The beam condenses immediately upon striking a surface and does not contribute to the residual gas pressure.

C. THE ION TRAP AND ELECTRON GUN

The central piece of equipment, around which the entire experiment is built, is the ion trap itself. Figure 22 shows the trap, its mounting, and the electron gun assembly. The endcaps, made of OFHC copper, were cut on a tracer lathe which followed an accurate template produced by a numerically-controlled milling machine. The lower cap has a 1/2 inch diameter

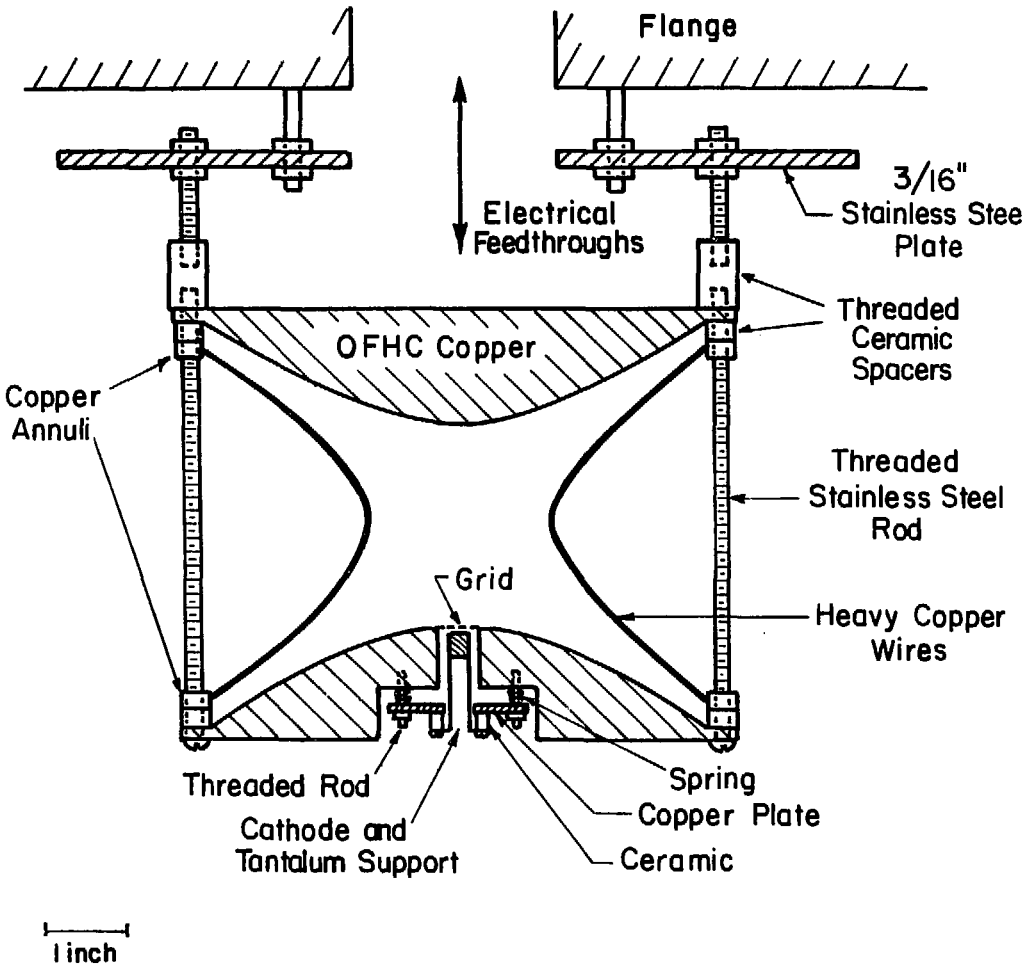


Figure 22. Detailed view of the ion trap and its mounting.

hole covered by a fine-mesh tungsten grid which is spot welded to a cylindrical tantalum insert. The ring electrode is made from 18 heavy copper wires, spaced every 20°, which were bent into hyperbolas on a template and are held by screws in two accurately spaced copper annuli. The shape of the equipotential surface is improved by 21 equally spaced 6 mil copper wires which encircle the framework formed by the heavy wires, thus making the ring electrode a loose, highly transparent mesh. Four stainless steel rods separate the two annuli, and each endcap electrode is attached to the ring by using tapped 3/8 inch ceramic spacers and stainless steel screws. Tabs for making electrical connections extend outward from some screws.

The trap assembly is mounted by means of 4 ceramic spacer - stainless steel rod combinations to a 3/16 inch stainless steel plate which is suspended from the top flange of the vacuum system. The spacings can be adjusted so that both the plate and the trap are accurately parallel with the flange. The mounting is rotated so as to avoid locating the stainless steel rods in front of any of the eight ports and to allow the lithium beam to pass between the heavy wires of the ring electrode. Electrical feedthroughs are located in the center of the top flange. Connections are made with tantalum wires which pass through a $2\frac{1}{2}$ inch diameter hole in the steel plate and are bent around to their destinations, where they are mechanically attached.

The electron gun used initially was an $\simeq$1/4 inch long 3 mil tungsten filament, spot welded to a tantalum support and mounted 2-3 mm behind the grid of the lower endcap. Typical emission characteristics of this filament are shown in Figure 23, which plots the current striking the upper endcap, for various magnetic fields, as a function of the filament heating voltage. The focusing value of the magnetic field is obvious. A problem with this filament, though, was an apparent instability which caused the electron beam to diverge too much and not always intersect the Li beam. The result was a very erratic behavior of the number of ions stored from cycle to cycle. This was alleviated by switching to a 1/4 inch diameter Spectramat dispenser cathode which emits electrons uniformly over the entire cathode surface and can thus produce larger currents before space charge instabilities become a problem. The cathode is heated by a $\simeq 1\frac{1}{2}$ amp 60 Hz current, producing an electron beam current of $\simeq$30 μamp. The

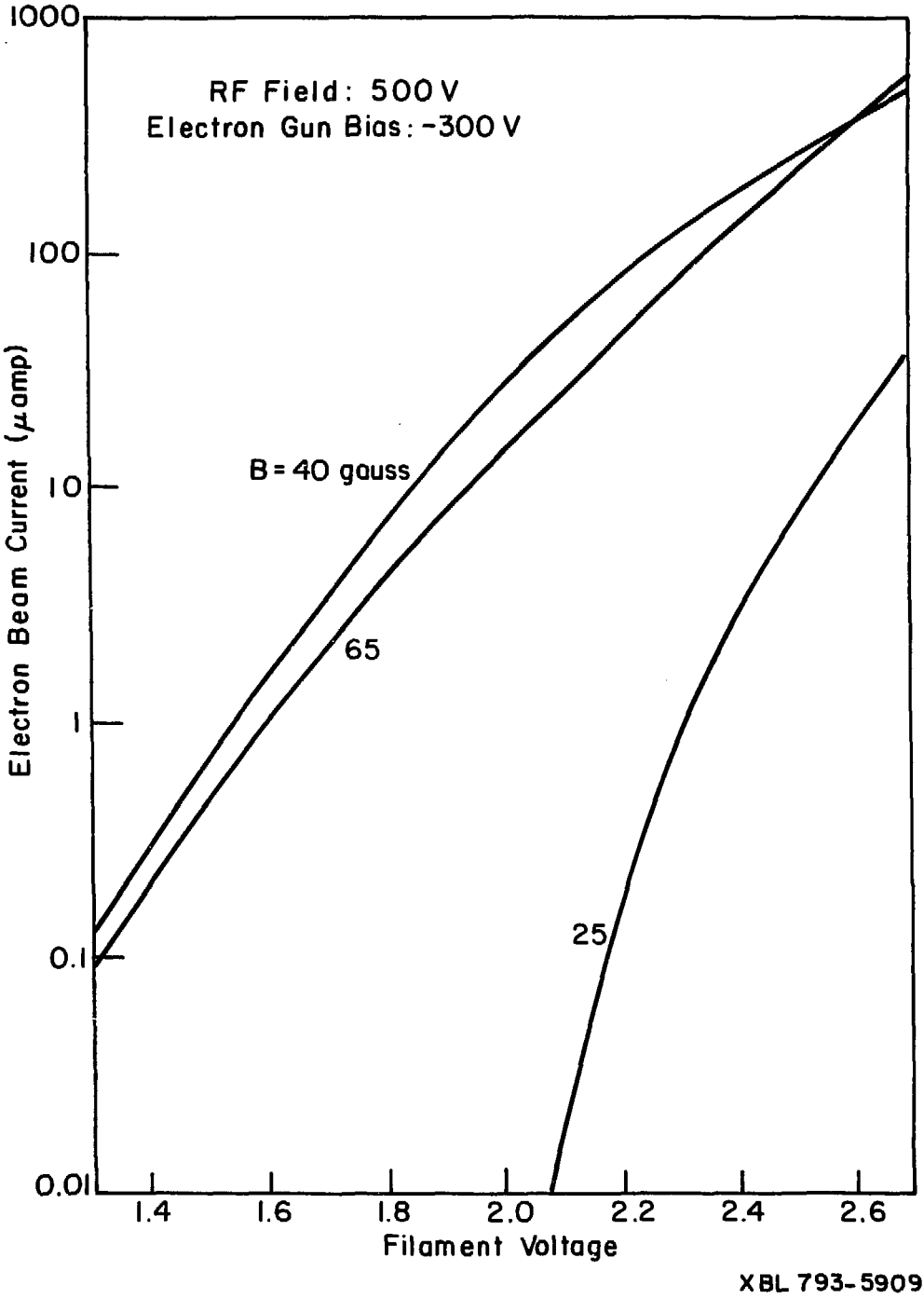


Figure 23. Electron gun emission curves for three different magnetic field strengths.

current is controlled by a computer-actuated relay which switches the cathode bias between +30 volts in the OFF state and a large negative voltage, typically -500 volts, in the ON state. These conditions produce the maximum possible ion signal, corresponding to $\cong 2 \times 10^5$ ions, with a filling time of 1 - 2 sec. Longer times or increased currents produce no further gain, presumably due to complex factors such as the electron beam divergence and the electrons' perturbing effect on the trapping potentials.

D. THE MAGNETIC FIELD

As mentioned previously, a small axial magnetic field is needed to keep the electron beam tightly focused in the presence of the rf-field. The production of a field, however, is constrained by the need to be able to easily assemble and disassemble the coils in order to bake the vacuum system. This prevents the use of a simple pair of coils around the top and bottom of the main vacuum chamber. A scheme whereby these requirements are met is shown in Figure 24a. Eight coils, wrapped on 1 inch diameter steel, fit between the vacuum chamber ports. Two steel rings fit over the ends of all the coils, providing magnetic continuity and smoothing the field to where it is nearly axially symmetric. Parallel currents in the coils cause lower order radial fields to cancel and produce a roughly axial field, as shown figuratively in the diagram.

A Hall probe was used to map the z-component of the magnetic field over a region the size of the trap. Figure 24b shows that over a distance comparable to the ion cloud radius ($r \leqslant .6$ cm), the field is nearly uniform. A relation between the field strength and the magnet current, good to a few percent, was found to be

$$B(\text{gauss}) = 4.0 \times I(\text{amp}).$$

Typical operating currents were 12.5 - 15 amp, corresponding to a field of 50 - 60 gauss. Fields as low as 30 gauss did not appreciably alter the ion creation rate, but the lower fields resulted in a significantly higher background rate in the photon detectors. This was attributed to the possibility that less well focused electron trajectories allowed some electrons to strike and charge up

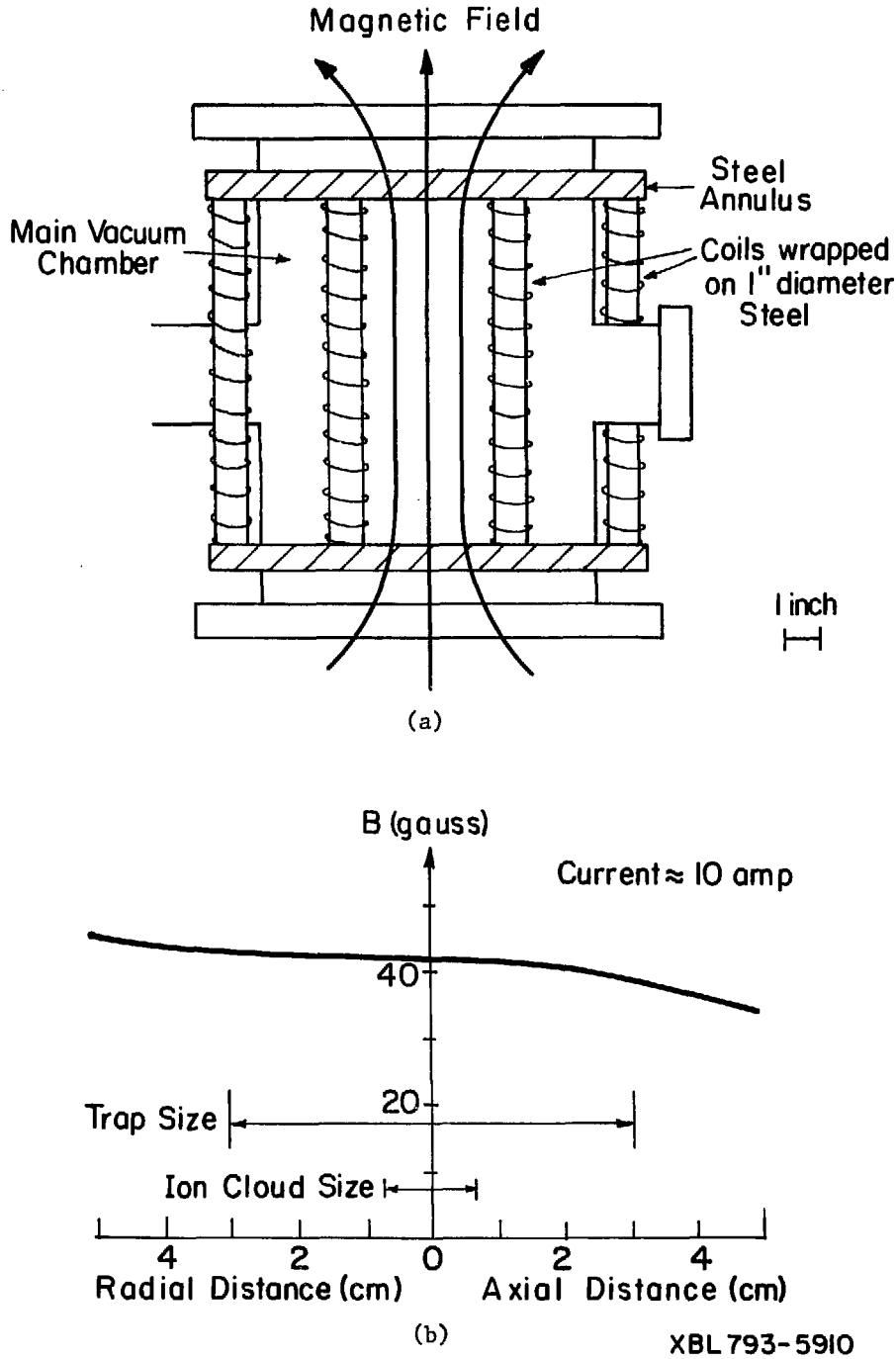


Figure 24. (a) Production of the magnetic field. (b) Field behavior measured both axially and radially from trap center.

detector surfaces.

E. ION TRAP ELECTRONICS

The electronics associated with the experiment are fairly complex, and for that reason their discussion has been divided into several parts. This section describes the electronics directly associated with the ion trap. The photon detection system is deferred until the next section, while the computer interface is the subject of Section V.G.

1. Trap Voltages and Frequencies

A diagram of the ion trap electronics is given in Figure 25. Operation of the trap requires the generation of the potential $U = U_0 - V_0 \cos\Omega t$, which is applied to the ring electrode. The source of the rf is a General Radio 1 MHz crystal oscillator. This is amplified in two stages, the second of which uses a 1 KW triode amplifier whose output tuned circuit was changed to a parallel LC network to emphasize voltage rather than power. A maximum plate voltage of 1 KV results in an rf-amplitude of $\simeq$550 volts.

The DC voltage is required to perform several functions, and its generation is correspondingly more complex. Besides supplying the proper potential during storage to maintain a spherical well, the DC voltages must also shift to different levels during the trap fill (in order to minimize storage of background gas ions), ramp through the ion resonance for detection, and switch rapidly to a large negative voltage in order to empty the trap. To accomplish this, all of the functions except the dump pulse are provided by three power supplies added in series. The first of these is a Kepco programmable power supply which produces level shifts, e.g. to a different potential for filling the trap, under control of a computer interfaced digital-to-analog convertor. Added to this is a DC power supply which is adjusted, while the programmable supply is at zero, to provide the most positive needed potential. Finally a function generator is added to provide a single adjustable ramp when triggered by the computer. This summed DC voltage is passed through a transistor switch which, when gated by the computer,

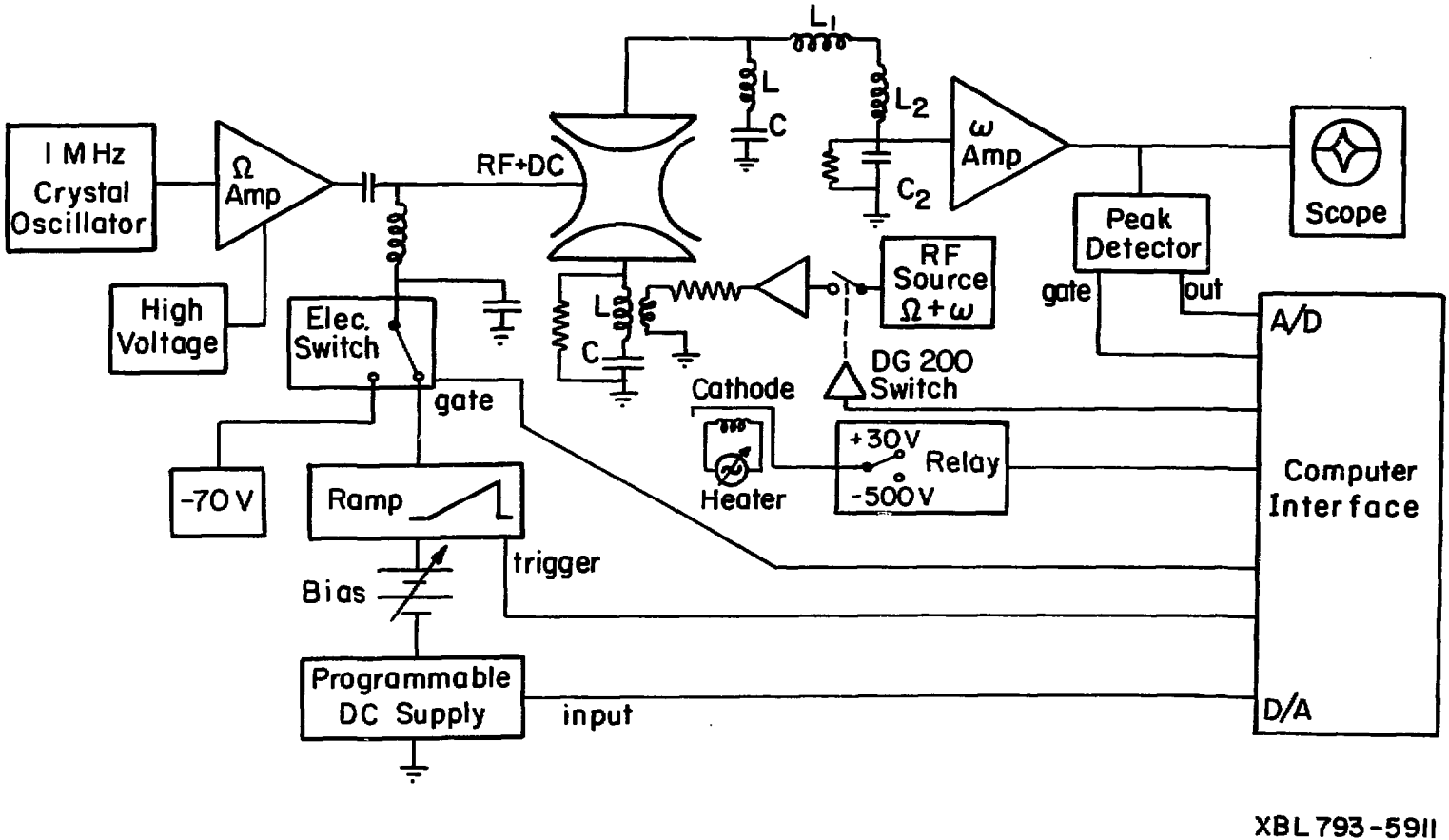


Figure 25. Electronics associated with the creation, storage, and detection of ions.

can switch to a -70 volt supply for 10 msec to provide the dump pulse. A schematic diagram of this switch is shown in Figure 26.

The rf and DC signals are summed through a capacitor and rf-choke as shown. To prevent rf-currents from flowing across the ring-endcap capacitance and creating large rf-voltages on the endcap electrodes, both endcaps are connected to ground through an LC shunt which is tuned to Ω. This reduces the endcap rf-amplitude to $\leqslant$ 10 V when a 500 V rf-signal is applied to the ring. In addition, resistors to ground are attached to the lower endcap and across capacitor C_2 to provide a DC return for the electron current.

2. Ion Excitation and Detection

The method of sideband excitation and resonance detection was described fully in Section IV.B. The source of sideband voltage is a Tektronix constant amplitude rf-generator, tuned to $\Omega + \omega$. A computer controlled Siliconix DG-200 FET switch passes the sideband voltage only during the excitation period. A power amplifier drives current through a few coils of wire which are wrapped around the inductor of the lower endcap Ω-shunt, thus providing a weak coupling to the trap. This typically produces a sideband amplitude of $\simeq$1 volt on the endcap.

Inductor L_1 is tuned with the endcap capacitance to produce the parallel LC circuit resonant at ω. Series resonance network L_2C_2, also tuned to ω, has no effect on L_1 since its resonance impedance is near zero. It is used as a means of coupling out the ion signal at ω without loading down the parallel resonance, and the circuit additionally helps filter out the residual endcap voltage at Ω.

The tuned amplifier and peak detector are shown in Figure 27. The μ739 operational amplifier was chosen for the first two stages on the basis of its low noise characteristics. The input resistance was made as low as possible, limited by the requirement of not loading the series LC input circuit, so as to minimize Johnson noise. The LM318 operational amplifiers were chosen because of their ability to handle 20 volt peak-to-peak signals at 100 KHz. The tuning sections of stages two and three are not particularly elegant but work adequately and can

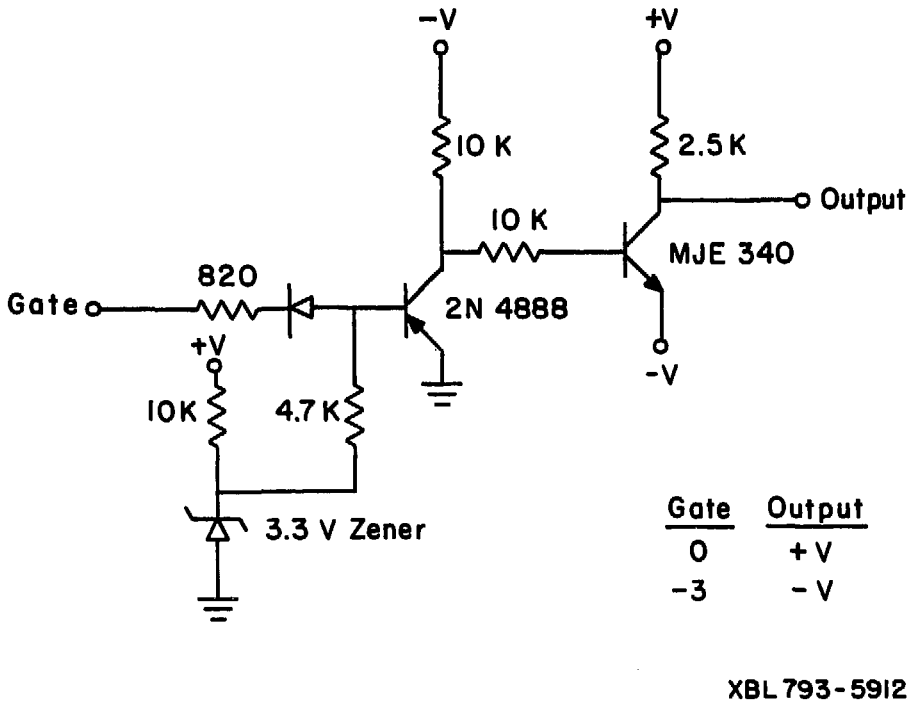


Figure 26. Schematic diagram of electronic switch used to provide the DC dump voltage to the ring electrode.

T_w wall temperature

$|\vec{V}|$ modulus of secondary motion vector velocity at a point in the flow

V_B surface average longitudinal velocity at ϕ plane

v_ϕ longitudinal velocity component

v_r radial velocity component

v_z axial velocity component

z axial direction in cylindrical coordinates

θ non-dimensional temperature at a point in the flow $\left(\frac{T_w - T}{\bar{T}_w - T_{in}}\right)$

θ_B non-dimensional mass average temperature at ϕ plane $\left(\frac{\bar{T} - T_{in}}{\bar{T}_{in}}\right)$

μ viscosity

ρ density

τ_w wall shear stress

ϕ longitudinal direction in cylindrical coordinates

be easily adjusted by the addition of small capacitors. The tuned elements do, however, increase the high frequency roll-off of the amplifiers and make them susceptible to oscillation. Placing capacitors across the power supply inputs to each integrated circuit and taking care to minimize stray capacitance kept the circuit stable. The resonant frequency is 103 KHz with an overall peak gain of $\simeq 10^5$ and Q $\simeq$ 30. The noise level is $\simeq$50 mV, mostly at the 1 MHz rf-frequency, and the maximum signal has an $\simeq$12 volt amplitude. "Typical" Li^+ ion signals are 1 - 2 volts, exhibiting good S/N.

The peak detector is a modified half-wave rectifier. The voltage-follower arrangement of operational amplifiers eliminates voltage drops across the diodes, and the high input impedance of the μ741 allows the capacitor to hold its voltage with a barely perceptible drop in 1 sec, far longer than required. The peak detector is reset by the computer controlled closing of a DG-200 FET switch, discharging the capacitor. The detector output is routed to the computer's analog-to-digital convertor.

F. THE PHOTON DETECTION SYSTEM

1. Detector Operation

The photon detection system consists of a grazing incidence light pipe to improve collection, a thin aluminum foil which serves as a filter, an electron multiplier to detect photons, and an electronic counting system. These are shown in Figure 28. Two identical systems are used, located 180° apart in the trap's horizontal midplane. The distance from the trap center to the first dynode of the detector is $\simeq$12 cm. The detectors were set back this distance to minimize interference from the rf and magnetic fields, and they are further protected by a mu-metal shield around the vacuum system ports in which they are housed.

To regain some of the solid angle which was lost by having to locate the detectors back 12 cm, light pipes were installed in front of the detectors. The pipes are made by evaporating a 200Å platinum coating on the inside of a glass cylinder, shaped as shown in the

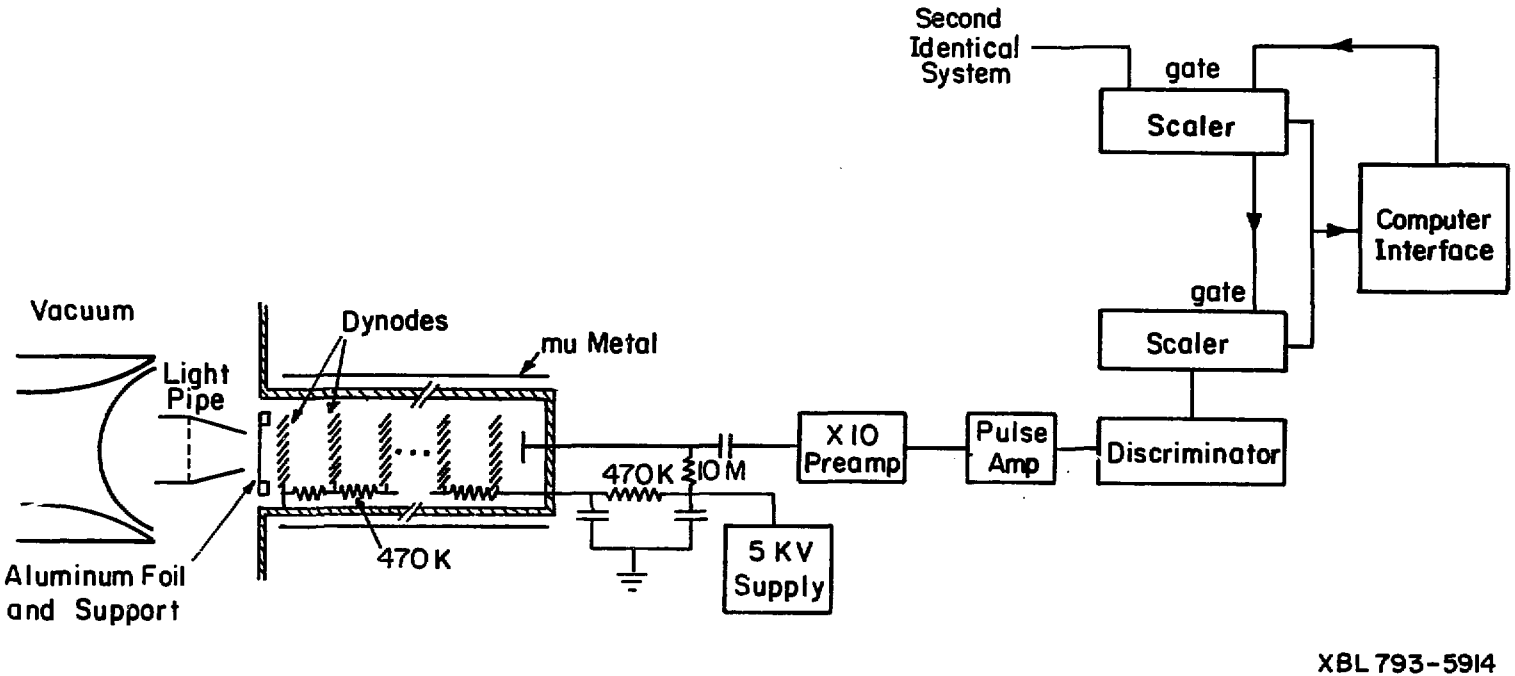


Figure 28. Photon detection and counting system.

diagram with a front diameter of 4.0 cm. They are clamped onto the ring electrode stainless steel support rods and maintained at the ring potential so as not to produce a perturbing electric field.

The principle upon which the light pipes are based is that vacuum ultraviolet radiation, incident at grazing angles upon a heavy metal surface, is reflected at near 100% efficiency[40]. Gold surfaces, for example, have a 114Å reflectance which falls off nearly linearly with grazing angle, being 100% at 0° and dropping to zero at ≃30°. A reasonable guess for the 200Å reflectance of a platinum surface would be a linear fall-off from 100% at 0° to zero at ≃60°. With this in mind, the light pipes were designed such that all rays originating at the trap center and entering the pipes would strike the 1 inch diameter detector after at most one bounce of $< 25°$, thus insuring reflectance of $\geqslant 2/3$. The fraction of photons collected both from an entire Gaussian ion cloud with $\Delta_r = .5$ cm and from a 2 mm diameter cylinder (i.e. a laser beam) passing through such a cloud was determined by a computer integration, using the 0° - 60° reflectance model noted above. Any difference between the collection efficiency of the two volumes was less than the 1% numerical error. The collection gain provided by the light pipes was found to be 7.5 for this model, resulting in an estimated 2 - 4% of all isotropically emitted photons striking one of the two detectors, depending on the size of the aluminum foil used.

The aluminum foil filter was found to be necessary to prevent the counting of ions as they were slowly lost from the trap. An 800Å thick coating, which is ≃65% transmitting at a wavelength of 200Å[41], is evaporated onto a glass slide, floated off in water, and then picked up on an aluminum support. The diameter of the foils used have been .75 inch and 1 inch. A holder mounted directly on the electron multiplier assembly locates the foil about 1/2 cm in front of the first dynode. Extreme care must be exercised during the manipulation of the detectors and during the vacuum system pumpdown to avoid rupturing the foils.

The photon detector itself is an EMI windowless electron multiplier, consisting of 24 BeCu venetian blind dynodes. It is mounted on a $4\frac{1}{2}$ inch flange which has feedthroughs for

the anode and last dynode. The biasing resistor chain is made of 470K metal film resistors which are spot welded directly to the dynodes. The first dynode is grounded directly to the multiplier's supports, and a positive high voltage, filtered by large capacitors located immediately adjacent to the feedthrough, is applied to the anode and last dynode as shown. Output pulses are AC-coupled through a shielded network to a preamp which is also located adjacent to the feedthroughs, thus minimizing excess counts arising from electrical noise.

The output pulses are amplified, passed through a discriminator, and routed to a scaler which is gated on by the computer during the counting phase. The counts from the two systems are wire-ORed together and sent to the computer. The maximum uniform pulse rate for which computer registration is 100% accurate is $\simeq 10^4$ sec^{-1}. Experimentally, the maximum observed count rate of randomly arriving pulses is 50 - 100 sec^{-1} during the first $\simeq$.1 sec of measuring S_2 (see Section III.C.), leading to an estimate that $\leqslant$ .5% of the pulses contributing to S_2 are missed.

The operating points of the detection system are determined as follows. The pulse amplification gain is set to give saturating pulses at a moderate high voltage and the discriminator is set at 2 - 3 times the amplifier noise level. Using the count rate observed when the ion gauge is used as a stable "signal", the high voltage is adjusted to give maximum S/N. This is 5000 volts for an older detector and 4500 volts for a newer one. The discriminator is then optimized by observing the $2\,^3P_1$ - $1\,^1S_0$ intercombination photons. The resulting noise level for the two detectors together, above which the spontaneous M1 photons must be seen, is typically 10 counts/minute.

2. Detector Calibration

While the absolute efficiency of the photon detection system is not a factor, the ratio of the efficiencies at the two wavelengths observed, $\frac{\epsilon_{202}}{\epsilon_{210}}$ is important. To determine this quantity, both detectors with foils in place were compared over the range 196Å - 228Å to a calibrated Channeltron electron multiplier. This was performed with a Ne IV discharge source and a 2.47 meter GCA/McPherson VUV grazing incidence monochrometer. The spectrum used is

CALCULATION PROCEDURE AND TEST CASES

The calculation procedure used to compute the flows in this study has already been described in [9]. Extension of the procedure to arbitrary orthogonal coordinate geometries and, especially, its application to developing curved pipe flows of strong curvature have been documented by Humphrey [10]. The latter reference contains general finite difference forms of the conservation equations for mass, momentum and transferable scalar quantities (species and energy). Detailed information concerning

shown in Figure 29. Both digital recordings of the peaks and valleys as well as slow wavelength scans were used, interchanging our detectors with the calibrated detector. During the slow scans, a count rate meter was used to average the detector response. The total photon flux, which was quite stable, was measured from the calibrated detector output and used to determine the efficiencies of our detectors. No significant differences between the two detectors were discovered. The efficiencies determined from the digitally recorded data are slightly higher than those determined from the scans, but both methods give the same $\frac{\epsilon_{202}}{\epsilon_{210}}$. The Channeltron calibration curve is shown in Figure 30a and the averaged calibration of our detectors, as measured from the scans, is shown in Figure 30b. The straight line is a least square fit from which the efficiency ratio is determined.

The major question is the determination of the errors. As Figure 30a shows, the absolute error of the Channeltron is roughly 13%, but its relative error, the only concern here, is considerably better and is conservatively estimated to be $\simeq$4%. With that in mind, a summary of the calibration data is shown in Table 4. The final value adopted for the efficiency ratio of our detectors is

$$\frac{\epsilon_{202}}{\epsilon_{210}} = .87 \pm .05,$$

where the quoted error represents one standard deviation.

It is of interest to use the measured efficiency to estimate the number of metastable ions stored. A laser-induced photon signal immediately following ion creation has typically 20 counts. A measured efficiency of 3% at 210Å combined with an estimated $\simeq$3% collection efficiency yields an estimate of the number of metastables:

$$N^* \cong 2 \times 10^4.$$

This is roughly 10% of the total number of ions, a not unreasonable value since an ion formed in any triplet state immediately decays to $2\,^3S_1$.

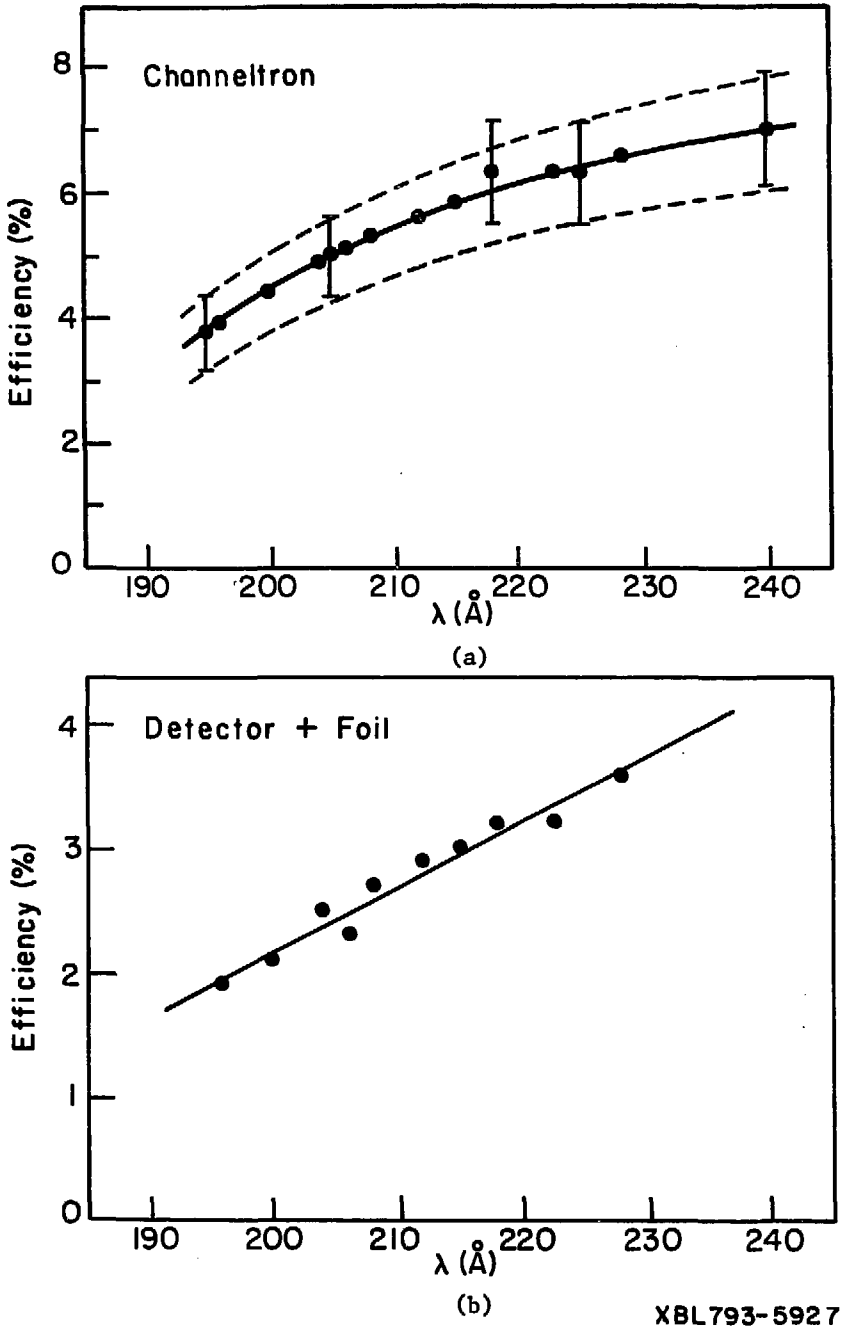


Figure 30. (a) Absolute calibration curve of the Channeltron electron multiplier. (b) Calibration of photon detectors with 800Å aluminum foil filters.

Table 4. Detector Calibration

	$\varepsilon_{202}/\varepsilon_{210}$
Average of 4 rate meter scans (both detectors)	.85
Average of 2 digital recordings (both detectors)	.89
Average of 2 rate meter scans and 1 digital recording (one detector)	.87

	Estimated Error
Channeltron relative efficiency	4%
Statistical measurement	3%
Least squares fitting error	3%
Total RMS error	6%

Calibration result: $\varepsilon_{202}/\varepsilon_{210} = .87 \pm .05$

G. THE LASER AND OPTICAL SYSTEM

The laser system is relatively independent of the remainder of the experiment and can, to some extent, be considered a "black box" which can be made to produce 5485Å radiation. Only when a fairly detailed look is taken, such as in Appendix A, do the narrow linewidth and polarization aspects of the laser become important. The main conclusion of Appendix A is that the laser's plane of polarization should be inclined at an angle $\theta = \cos^{-1}\left(\frac{1}{\sqrt{3}}\right)$ with respect to the magnetic field in order to produce an isotropic distribution of the 202Å intercombination radiation.

The components of the optical system are shown in Figure 31. The heart of the system is a tunable dye laser which can be brought into resonance with the $2\,^3S_1$ - $2\,^3P_1$ transition at 5485Å. The laser uses a folded cavity configuration with the dye in a thin jet tilted at Brewster's angle with respect to the optical axis. Pumping is achieved with 4 watts of output from a Coherent Radiation CR-5 Ar^+ laser. The dye is Rhodamine 110 in an ethylene glycol solution, and it was found advantageous to pass it both through a water bath heat exchanger to maintain constant temperature and through a hydraulic dampener to remove pressure fluctuations. A new dye solution will produce 150 - 200 mW power when all tuning elements are in the cavity, with the power dropping to 40 - 50 mW after $\simeq$100 hours use.

Rough tuning of the wavelength is accomplished by a birefringent filter in the cavity. This gives a linewidth $\Delta\lambda = .1 - .2$ Å, quite sufficient to locate the Li^+ transition, but the wavelength tends to drift with time. Further line narrowing and tuning are achieved with a Fabry-Perot etalon having a free spectral range of 2.0Å. This reduces the linewidth to $\Delta\lambda \cong .02$ Å and considerably improves the stability.

A weak beam reflected from the birefringent filter is used to monitor the wavelength. It is reflected from a wobbling mirror to produce a spot moving in a circular pat-

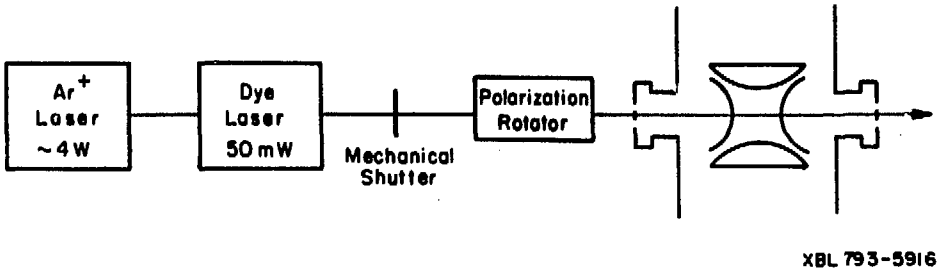


Figure 31. The dye laser and optical system.

tern. During a portion of the circle it passes across an etalon, with a free spectral range of .25Å, which is mounted in front of a photodiode. The changing angle of incidence as the spot moves is completely equivalent to the more usual case of tilting the etalon. The photodiode output as a function of time, which is easily displayed on an oscilloscope, then shows fringes which obey the etalon formula[42]

$$m\lambda = 2nd\cos\theta(t),$$

where d is the etalon thickness and n its index of refraction. This can be used to eliminate residual wavelength drifts by making occasional fine tuning adjustments of the internal etalon which keep the order spacing constant. In addition, comparison of the spacing between orders allows a relative calibration, so that wavelength changes can be measured with an accuracy $\simeq$.005Å as the internal etalon is tilted to scan the wavelength over a small range. This procedure is followed to measure the lineshape of the transition.

The laser beam is directed, using dielectric coated mirrors to minimize reflection losses, into the vacuum and is adjusted to pass between the wires of the ring electrode. After exiting the chamber, it can be either blocked or reflected back to increase the effective power. The laser beam's passage is controlled by a mechanical shutter, consisting of a computer-actuated relay with a long lever arm attached to it. To avoid optically pumping the metastable ions into an aligned state, it is necessary, as discussed in Appendix A, to have the laser's plane of polarization tilted at an angle $\theta = \cos^{-1}\left(\frac{1}{\sqrt{3}}\right) \cong 55°$ away from the magnetic field axis. Since the laser output is vertically polarized, parallel to the field, the laser is passed through a polarization rotator before entering the vacuum system. In addition, a telescope can be placed in the beam to expand it from its normal $\simeq$1 mm diameter up to $\simeq$4 cm in order to check for systematic errors related to the laser beam - ion cloud interaction.

II. THE COMPUTER SYSTEM

1. Timing and Control

The brain, as it were, of the entire experiment is a PDP 11/10 minicomputer. The computer times and directs the complex sequence of events, which varies for different aspects of the experiment. It also collects all data concerning ion signal levels, photon counts, and background; provides real time monitoring of data collection on a display oscilloscope and periodically outputs other monitoring information; and manipulates and analyzes the data, using a least squares routine. The analysis program also stores the results from the various types of data collecting sequences, to be described in the next section, until all of the information needed to determine the radiative lifetime is available. It then performs the calculations, including an error analysis, and types the result.

Needless to say, the computer interface and programs are quite complex and took several years to evolve into their final forms. It is not, however, necessary to present a detailed description in order to understand the general structure. A block diagram of the interface is given in Figure 32. The main flow of information is out of the computer, and this is accomplished with the use of a 16-bit buffer register which responds to a particular address that can be referenced by the computer. As the need arises to control an event, the computer alters the appropriate bit from a logical 0 to a logical 1 or vice versa. Each bit in the buffer is connected to the experiment through a driver circuit which provides 0 volts (logical 0) or +3 volts (logical 1) and sufficient current to trigger a simple one-transistor switch which, in most cases, is the actual physical device used to switch the higher voltages necessary to gate a function generator, close a relay, etc. Other information transferred out of the computer includes an analog signal from a 10-bit digital-to-analog convertor, used to control the programmable DC power supply described in Section V.E.1., and two other D/A signals which control a scope display of the photon counting data as it is accumulated.

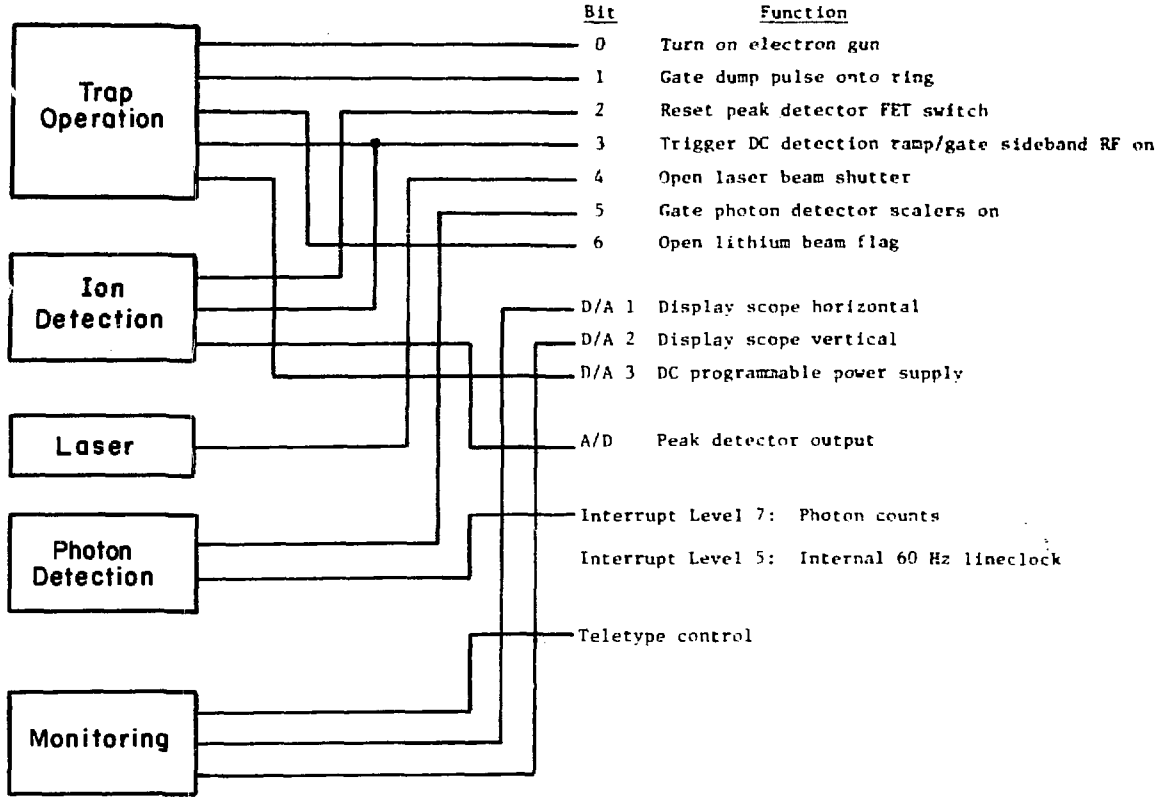


Figure 32. Main components of the computer interface.

Two sources of information flow into the computer. One is the output of the ion signal peak detector. In this case the computer has controlled the sequence of events necessary to produce an ion signal, and the detected peak height, presented to the analog-to-digital input, is being held on a capacitor. The computer, when it reaches the appropriate step in its program, then queries the A/D convertor and stores the digital value obtained. The other case, the arrival of a pulse signifying the detection of a photon, is an event over which the computer has no control. This is handled by applying the pulse to the input of the highest priority interrupt circuit. Its arrival causes an instantaneous ($\leqslant$ 3 μsec) halt of the computer's activity (usually running the display scope monitor) and forces a jump to a service routine which performs such functions as noting the time and incrementing various storage registers. Control then reverts to the computer's previous activity. The $\simeq$100 μsec operation time of the service routine is the basis for the 10^4 sec^{-1} maximum count rate mentioned in Section V.F.1.

Figure 33 shows a typical timing sequence generated by the computer, in this case one appropriate to measuring S_1 and S_2, the spontaneous and laser-induced photons. Following ion creation is a short delay, allowing the ion cloud to stabilize and such electrically noisy events as closing the beam flag to occur. The photon counting scalers are then gated on, and after an appropriate period, usually 2 sec, the laser is turned on. When counting is through, the scalers are shut off and the computer measures the ion signal for monitoring purposes, taking $\simeq$ .2 sec. The cycle is finally ended by applying a dump pulse to the ring electrode for 10 msec to empty the trap. It is then repeated for a background measurement, the only difference being that the Li beam flag is not opened so that no Li^+ ions are created. Other types of cycles exist for measuring the ion storage time, in which case the photon counting is omitted and the delay is automatically incremented each cycle, and for measuring the total metastable lifetime with the laser, for which the laser-induced photon counting is coupled with the variable delay.

Two different timebases are used to control events. During such operations as filling the trap or detecting ions, where timing is not critical, a programmed loop which takes 10 msec to complete is the basis for timing. Each event is controlled by presetting a register with the

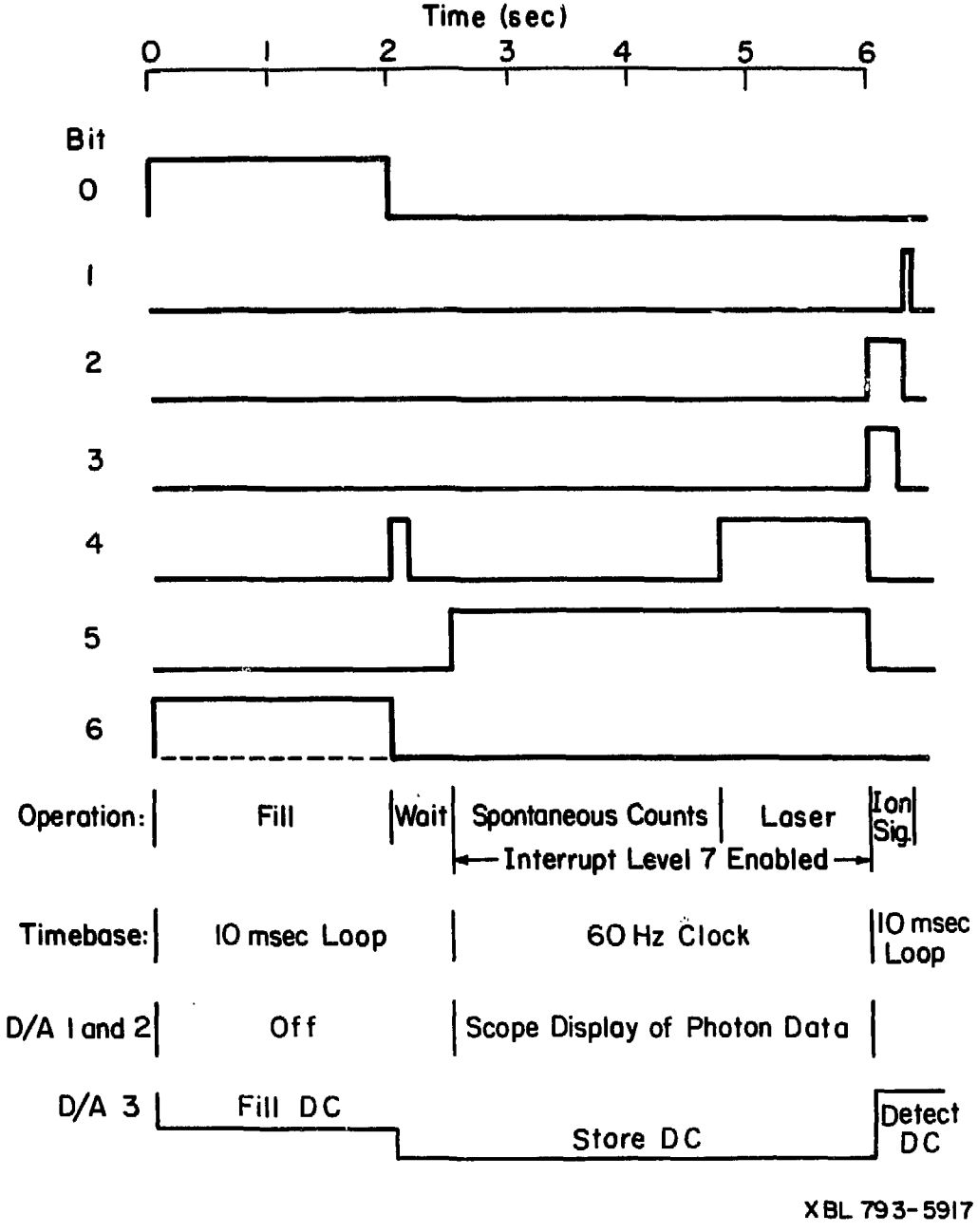


Figure 33. Typical timing sequence performed by the computer.

length, in units of 10 msec, which the event should last. More accurate timing during the photon counting is provided by an internal 60 Hz lineclock. Every $\frac{1}{60}$ sec the clock causes an interrupt, in a manner similar to that for the photon pulses, to a service routine which keeps track of the present data channel (which was pre-assigned a width in units of $\frac{1}{60}$ sec) as well as of the total elapsed time.

2. Operating and Analysis Programs

The computer programs can be broadly subdivided into operating and analysis programs, though the distinction is not absolute since some data manipulation occurs in the operating section. The operating program is written directly in machine language and is roughly 2000 words long. The analysis routines, however, are written in Basic; the Basic interpreter and programs occupy the remaining 6000 words of the computer memory. Only a general description of the programs will be given here.

A simplified flowchart of the operating program is shown in Figure 34. The program is quite complex, with many interactions and branches between the various parts. The many separate routines are independently written to maintain flexibility, and overall structure is provided by: the mainline program, which initializes everything; a table with approximately 40 entries providing such information as subroutine addresses, timing values, current system status, etc.; a set of eight flags turned on or off by different routines in order to indicate their status to other routines; and the computer switch register, which uses various combinations of switches to indicate which sequence is to be followed. The three major sequences are: (1) Measure the ion storage lifetime; (2) Measure the total metastable lifetime τ_{3S_1} with the laser; (3) Measure S_1, S_2, and τ_d, the depletion time, by counting spontaneous M1 and laser-induced photons separately.

As far as the data collection aspects are concerned, the computer functions essentially as a multichannel analyzer. As photon counts arrive they are added to the current channel, and at preset times the channel number is advanced by one. Separate channels are main-

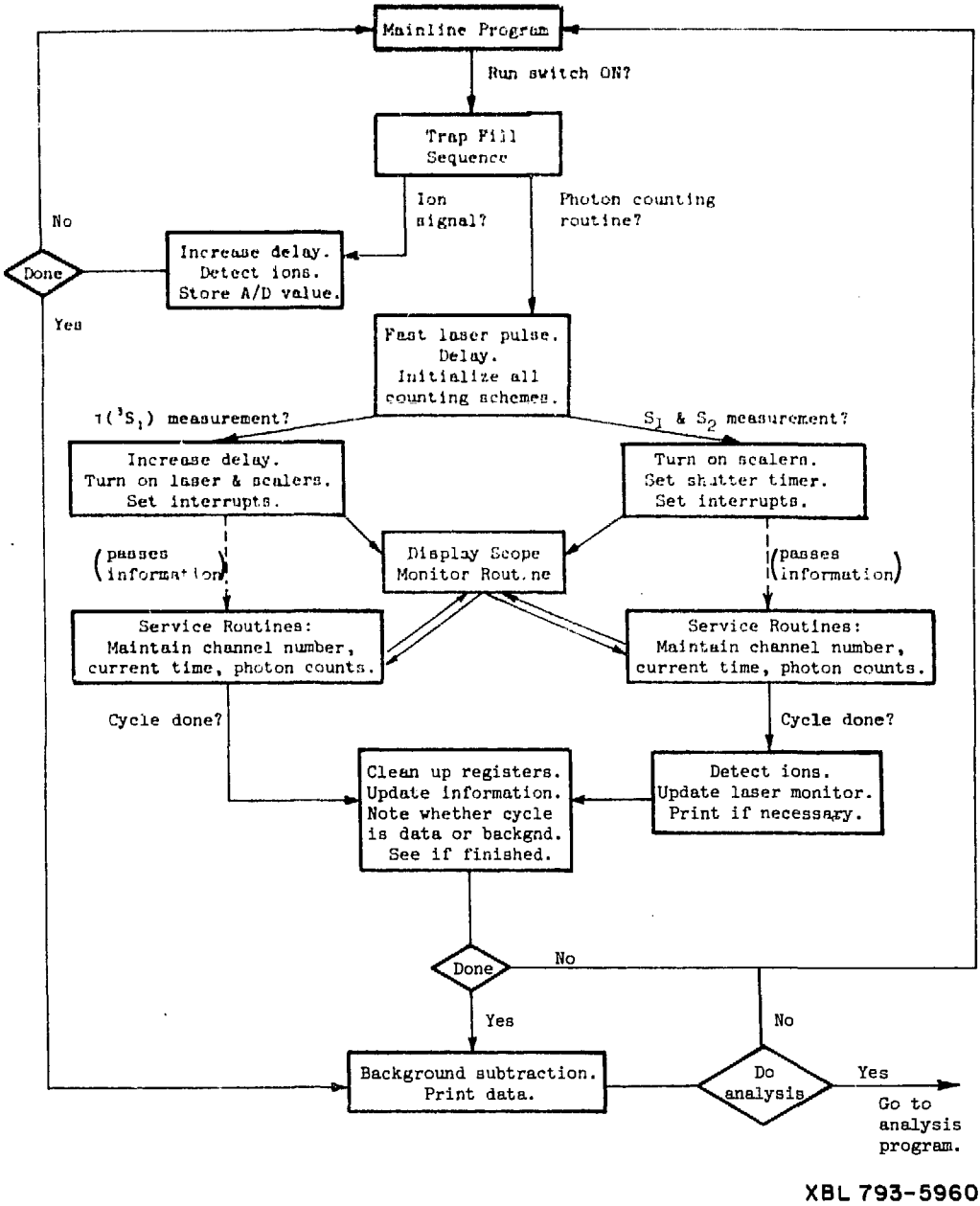


Figure 34. Flowchart of the operating program.

tained for the background. For the case of measuring $\tau_{^3S_1}$ with the laser, the average background is determined and subtracted from each channel prior to performing the analysis. When measuring S_1 and S_2, however, background subtraction is deferred until the analysis program in order to consider the backgrounds in T_1 and T_2 separately.

During the lengthy ($\simeq$1 hour) data collection runs used to measure S_1 and S_2, a special subroutine is used to monitor the laser for any drifts. A normalized laser signal is formed by summing the laser-induced photon counts for the previous 20 cycles and dividing by the summed ion signals, which are measured at the end of each cycle. This number, which is printed on the teletype, remains reasonably constant as long as the laser is stable. A decreased value indicates that the laser has drifted slightly off the resonance center, and data collection is halted while the laser is re-adjusted. This monitoring program is also used in a stand-alone capacity for the initial laser tuning performed before data collection is begun and for any re-adjustments made during the collection.

Data collection ends either with the setting of a front panel switch or when a preset criterion, such as the number of cycles to be completed, is reached. Any background subtraction is then performed, the data is printed on the teletype, and the computer transfers control to the analysis program. This was facilitated by modifying the Basic interpreter to allow it to more-or-less start in the middle without automatically erasing information from previous analyses. Figure 35 provides a flowchart of the analysis procedure. A machine language subroutine is used to retrieve such information from the operating program as data, channel widths, etc. The switch register is then queried to determine which sequence of events is being followed, and this information is parameterized by the variables F1 and F2.

The least squares analysis of the exponential decays is performed by fitting the logarithm of the data to a straight line, using standard procedures for the case where the uncertainty of the data is due to statistical fluctuation[26]. The main values of interest are the lifetime of the decay and its probable error. The reduced chi square value is also calculated to check the goodness of fit. The accuracy of the procedure was ascertained by the use of contrived data and by

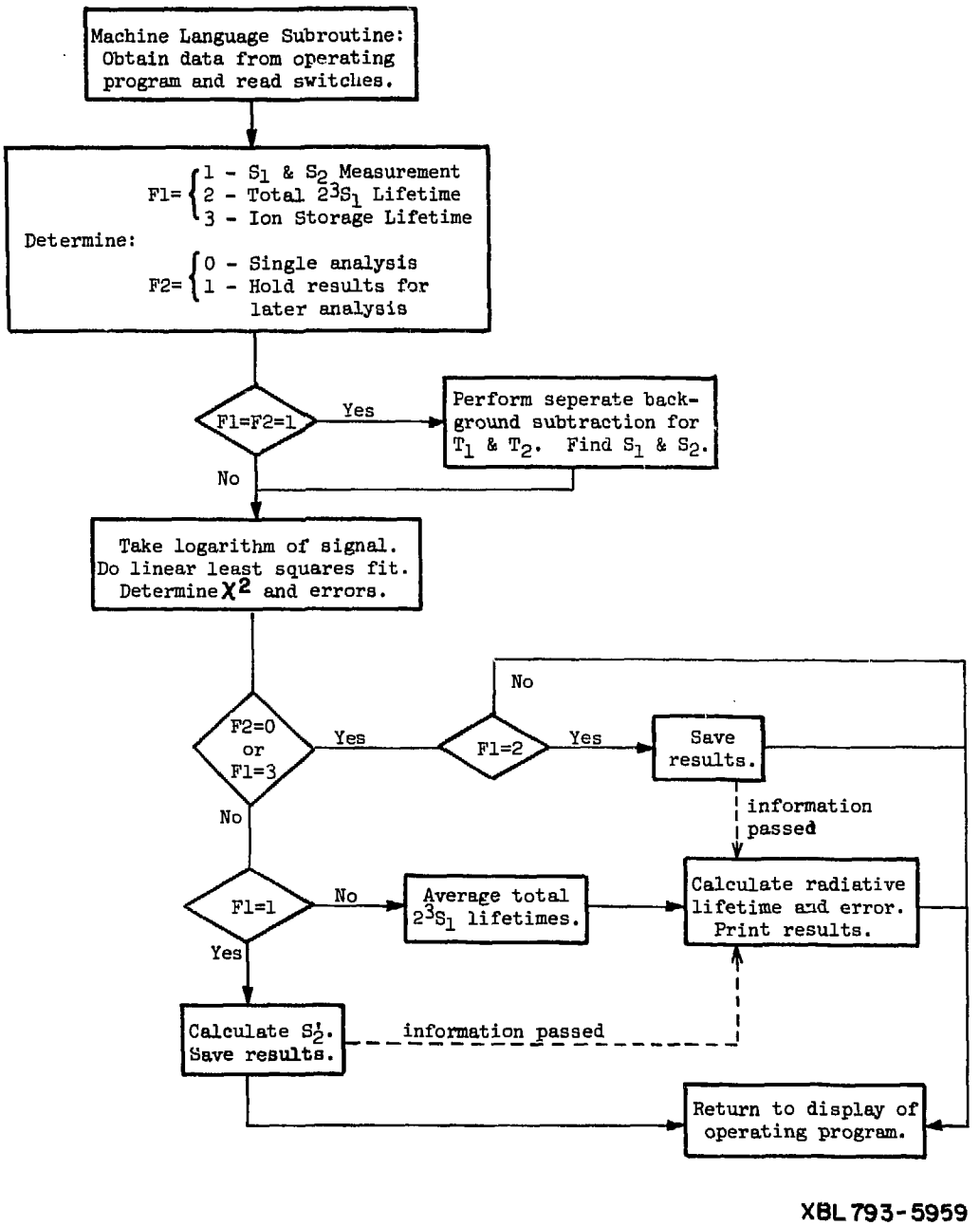


Figure 35. Flowchart of the analysis program.

independent checks of real data.

If the data was collected for a single purpose, such as measuring the ion storage time or checking the rate of laser depletion, the analysis ends after printing the least squares results. When the radiative lifetime is being measured, however, a specific sequence of measurements, each discussed in Chapter III, is made: (1) Measure the total $2\,^3S_1$ lifetime τ_{3S_1}; (2) Measure S_1, S_2, and the total depletion time τ_d; (3) Remeasure τ_{3S_1}. The analysis program recognizes these steps and saves the results of each until it has concluded step three. It then averages the two values of τ_{3S_1} and uses the result, along with the other stored information, to compute $\tau = \frac{\epsilon_{202}}{\epsilon_{210}} \tau_{rad}$ and $\sigma^2(\tau)$, using the formulas developed in Section III.C. At whichever point the analysis ends, the computer returns to the operating program's display scope section to exhibit the background subtracted data and await further operating instructions.

VI. EXPERIMENTAL RESULTS

A. THE DETECTION OF SPONTANEOUS M1 PHOTONS

Numerous experimental difficulties, such as high dark rates in the photon detection system and counts apparently due to residual gas ions, had to be overcome before the spontaneous $2\,^3S_1$ decay at 210Å was observed. It was during this phase of the experiment that we discovered the previously mentioned needs to keep the magnetic field at nearly 50 gauss and to fill the trap at a DC voltage high enough to exclude ions from the background gases. A small signal was finally seen that could unambiguously be traced to lithium since it vanished when the lithium beam flag was kept closed. Subsequent investigation showed that the observed signal abruptly vanished if the Li^+ ions were resonated out of the trap by a strong sideband voltage, providing further evidence that the signal was real. This is shown in Figure 36.

While the evidence tended to indicate that we were, indeed, seeing spontaneous photons, one disturbing fact remained: the signal exhibited a decay time of $\simeq$5 sec while the ion storage time was $\simeq$20 sec. To check the possibility that the signal might be nonexponential, having a 5 sec fast decay followed by a long tail, data were accumulated out to storage times of 23 sec, as shown in Figure 37. Though the background rate was not as good as later obtained, and even exhibits a slight curvature, it was clear that the signal was decaying reasonably exponentially with no indication of a tail. The integrated signal rate is $\simeq$3/cycle. This was the first indication that the metastables were being quenched, though many other explanations were considered at the time and considerable work was needed to decide among them. One thing which was fairly clear, though, was that a spontaneous decay curve measurement of τ_{rad}

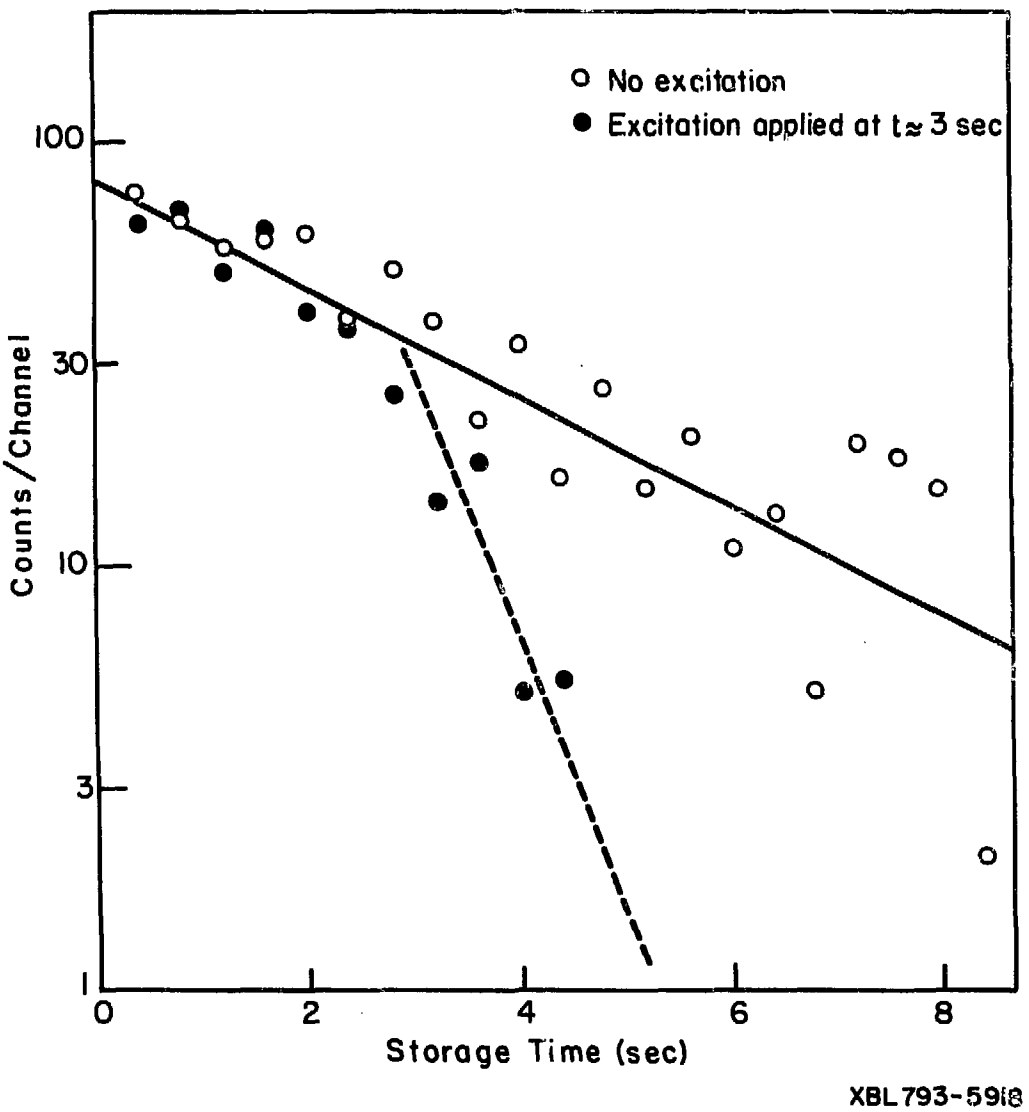


Figure 36. Spontaneous M1 photon signal, showing the effect of resonant expulsion of Li^+ from the trap.

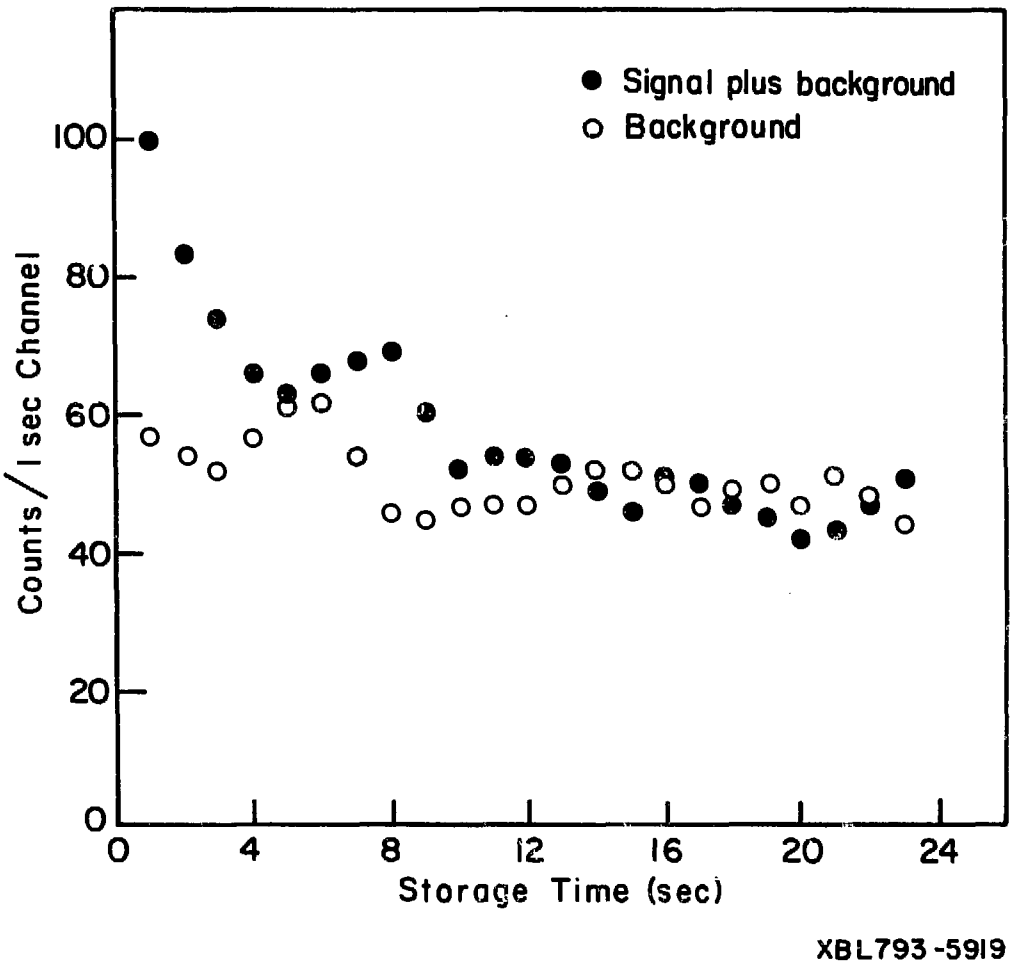


Figure 37. Spontaneous photon signal and background collected for 23 sec.

no longer seemed feasible.

B. THE DETECTION OF LASER-INDUCED PHOTONS

Work was then begun on the laser depletion of metastables, as discussed in Section III.B. The laser, which initially used a prism tuning element, was adjusted with a 1/4 meter spectrometer to be near the transition wavelength of 5485Å. Small tuning adjustments were then made until the photon count rate was observed to rise. The signal, once found, was very erratic as a result of laser instabilities, but installation of a birefringent filter tuning element in the laser cavity improved the signal considerably. Somewhat later, an etalon was introduced into the cavity to produce still further gains in linewidth narrowing and stability.

Quite good signal-to-noise was obtained almost immediately, and depletion times $\tau_d \cong .3$ sec were observed for laser powers of 100 mW, in reasonable agreement with the simple theory of Section III.B. Figure 38 shows the immense improvement over detecting spontaneous photons. In this case, spontaneous photons are seen for the first second, then the laser is turned on (taking a finite time, which is why the first channel of laser-induced counts is lower than the second) and the metastables are quickly depleted as each is forced to emit a 202Å photon. One striking observation was that, while the spontaneous photons produced only about 3 counts/cycle, laser depletion resulted in 20 - 30 counts/cycle. This large difference was the first direct evidence that the metastables were being lost by some nonradiative process.

Further study of the laser depletion process led to the measurement of the transition lineshape for different conditions. One such lineshape, made for $^6Li^+$, is shown in Figure 39a. In this case the laser, with power P, was tuned with the internal etalon, the measured τ_d was corrected for the total metastable lifetime τ_{3S_1} to obtain the laser depletion time τ_l, and the power-independent value $\frac{1}{\tau_l P}$ was plotted versus λ. The broken line indicates the expected lineshape for pure absorption, where the various hyperfine levels are populated in proportion to

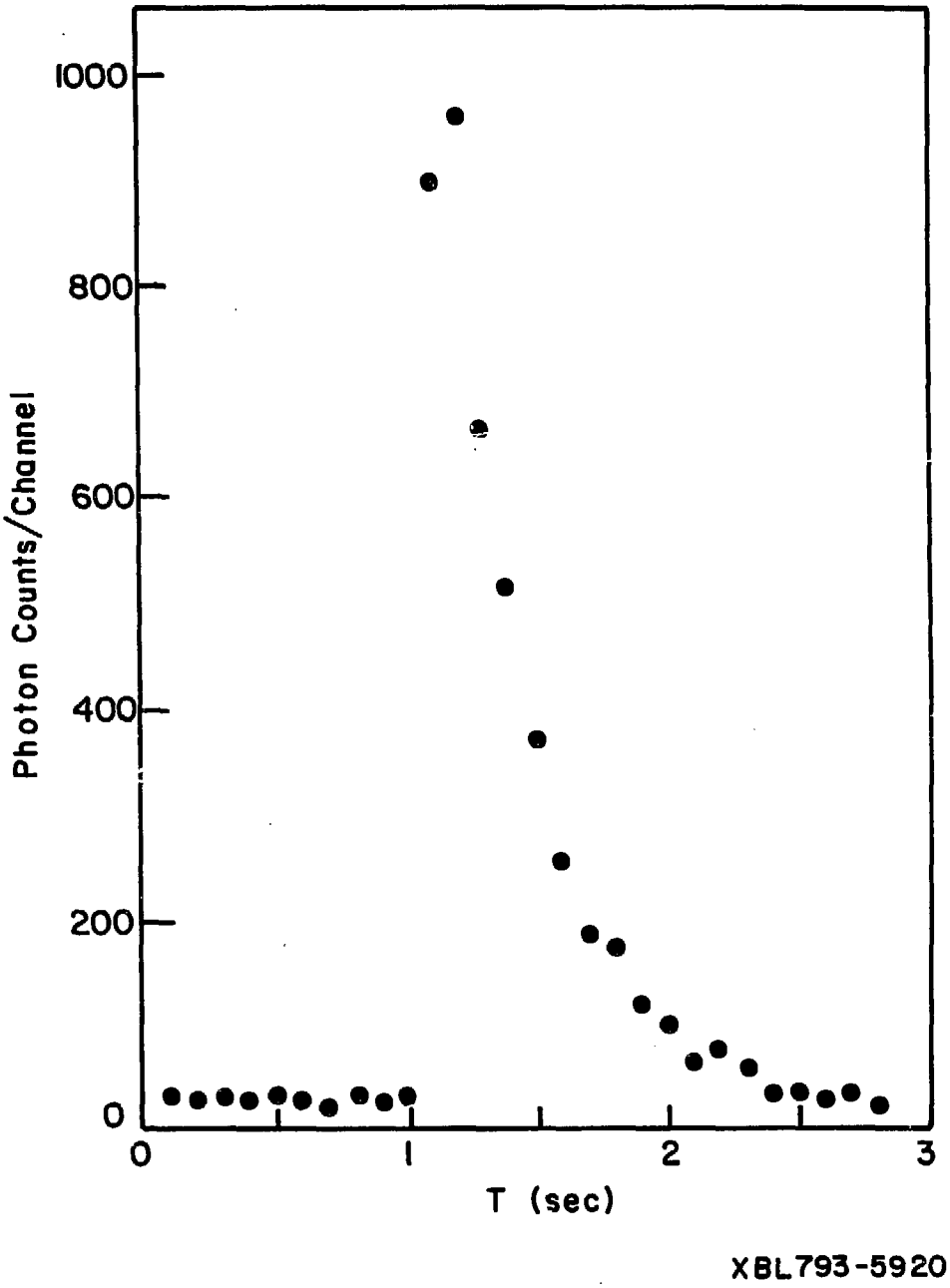


Figure 38. Photon counting signal when the laser shutter is opened at T = 1 sec. The counts for T < 1 sec are spontaneous, those for T > 1 sec are laser-induced plus spontaneous.

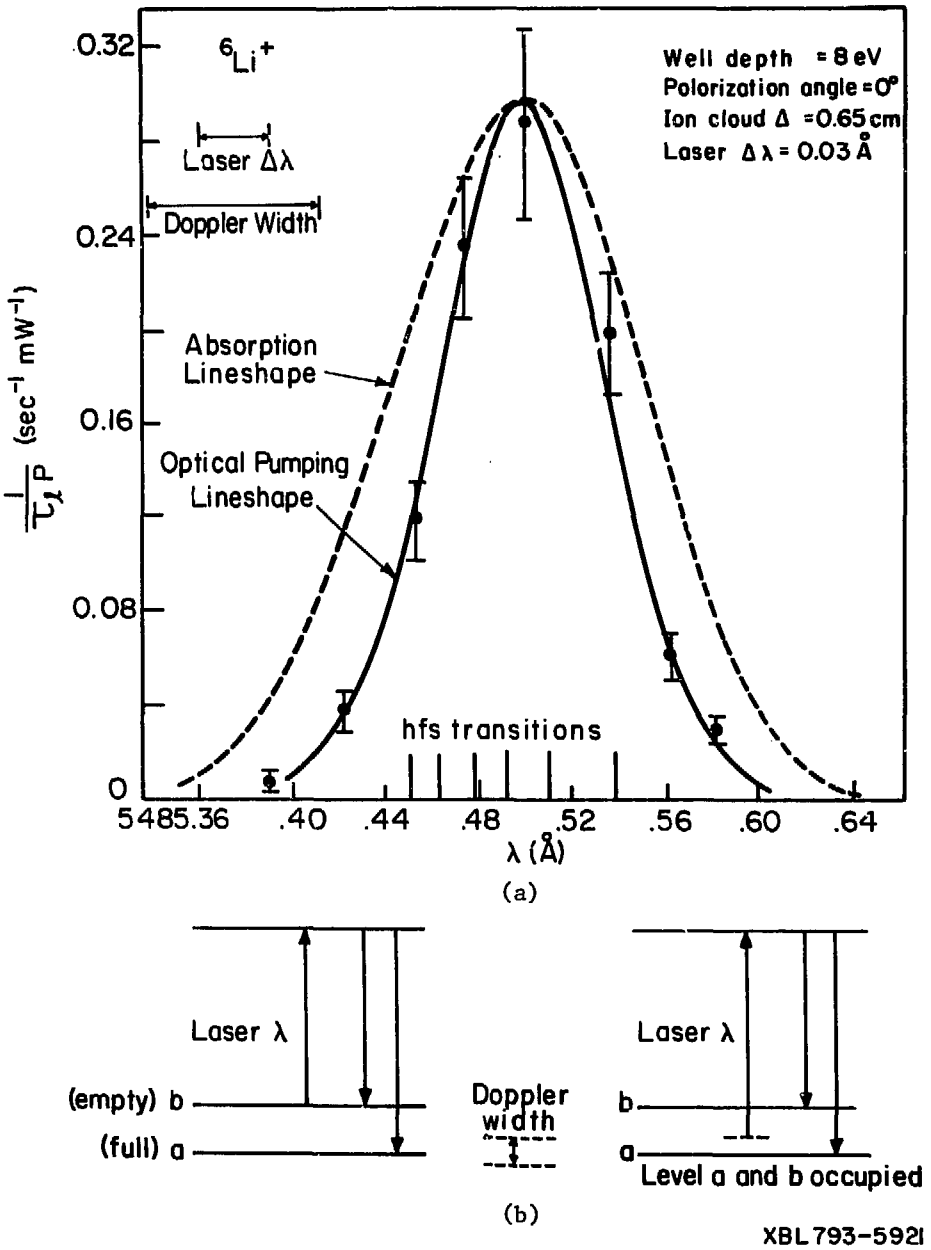


Figure 39. (a) Comparison of the observed $2^3S_1 - 2^3P_1$ lineshape with predictions based on pure absorption and on optical pumping. The wavelengths of the hyperfine transitions are indicated beneath the curves. (b) A simple explanation of optical pumping, showing that ions continue to be excited only when the laser is tuned near the center of the levels.

their statistical weights, whereas the solid line is an optical pumping lineshape for the parameters listed, as calculated in Appendix A. The optical pumping curve assumes that there is no relaxation between the hyperfine levels. The actual wavelengths of the various hyperfine transitions are indicated beneath the curves. The data indicates that the laser is causing optical pumping between the hyperfine levels. An intuitive description is given in Figure 39b. If the wavelength is to one side of center, then the laser tends to preferentially deplete the nearby level by moving the ions into the level which is further away from resonance, from which they are hard to excite. Since the ions have to be pumped around the $2\,^3S_1$ - $2\,^3P_1$ loop $\simeq$1200 times before they decay at 202Å, the laser-induced decay rate is very slow. Only when the laser is tuned very near the center of the levels, where it interacts equally with the Doppler tails of ions in both levels, can the laser-induced decay proceed. The difference between the absorption and optical pumping lineshapes is even more striking in $^7Li^+$ because of its large hyperfine structure, but it is difficult to measure accurately since a narrow linewidth laser at the signal peak is several Doppler widths away from the outer levels, and the depletion rate is thus much slower than in $^6Li^+$.

C. THE METASTABLE LIFETIME AND NONRADIATIVE QUENCHING

By using the laser as a probe of the metastable population, the metastable lifetime $\tau_{^3S_1}$ could be measured with reasonable accuracy in a time (10 minutes) much shorter than was possible with spontaneous emission, as discussed in Chapter III. In fact, the advantages were even larger than estimated since most of the metastables were apparently not decaying by spontaneous emission, whereas the laser-induced depletion still affects all metastable ions. The observed depletion times, $\tau_d \cong .3$ sec, led to the use of one second wide data channels when measuring $\tau_{^3S_1}$. Essentially all metastables are then depleted during one channel, and the number of photons counted is a good measure of the number of metastables present when the laser is turned on.

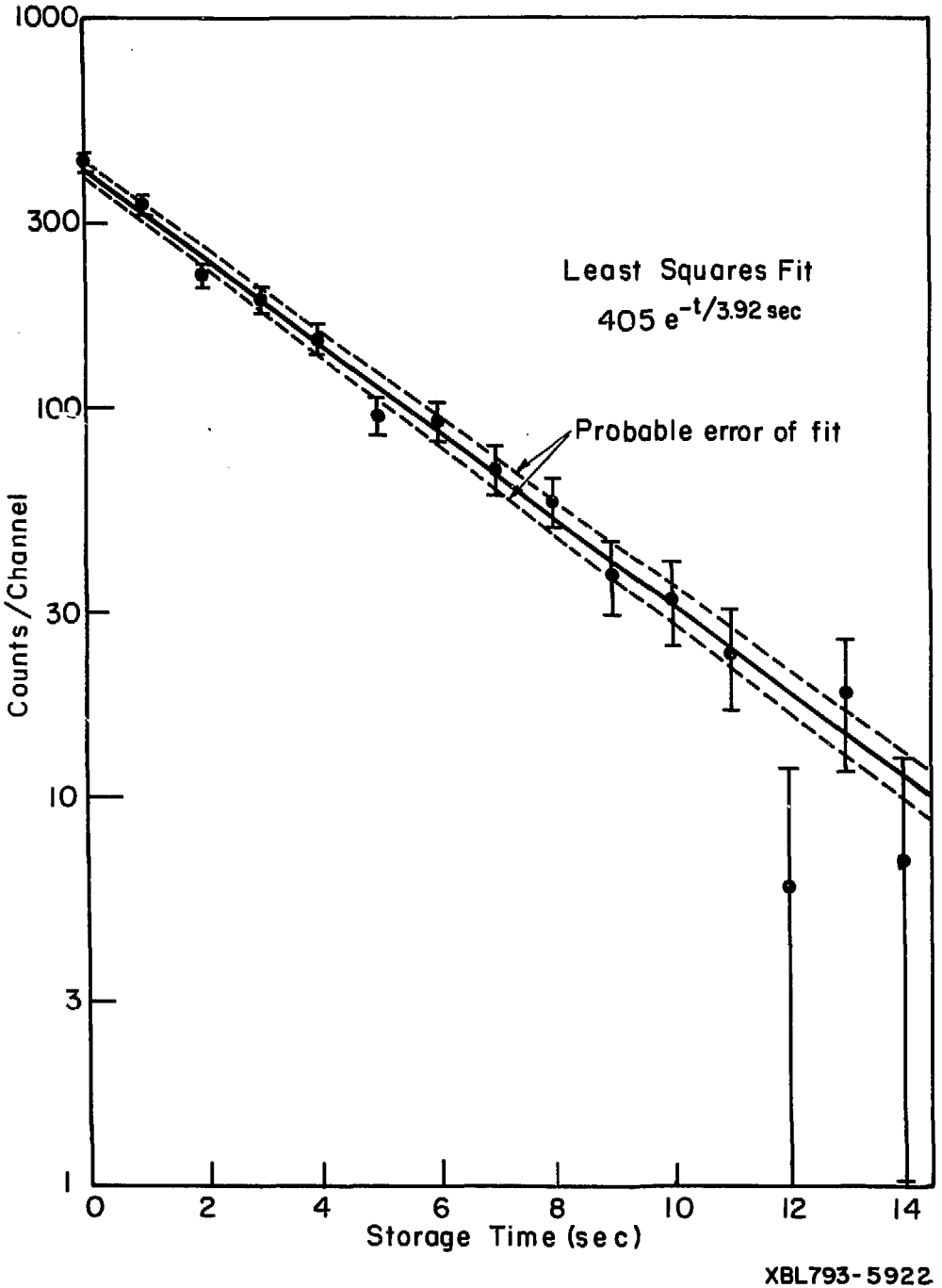


Figure 40. Laser-induced photon signal and the least squares fit of an exponential decay.

The first measurements taken showed that the metastable lifetime, as determined with the laser, was the same as that determined by counting spontaneous photons. This, in fact, confirmed that the previously seen signal was due to spontaneous emission, a fact which had seemed probable but had not been shown conclusively. A next step was to verify that the decay was really exponential. This could not be accurately done with the spontaneous decay signal because of poor statistics. Figure 40 shows the results of accumulating laser-induced data for over four decay lifetimes. The straight line is a least squares fit and the broken lines indicate the probable fitting error. It is clear that the assumption of exponential decay is quite good.

If all metastables were decaying by spontaneous emission, then the integrated spontaneous photon signal would be the same, apart from the detector factor $\frac{\epsilon_{302}}{\epsilon_{210}}$, as the integrated laser-induced photon signal. The observation, described in the preceding section, that it was about a factor of ten less indicated that most metastables were being lost nonradiatively. A first step in elucidating this problem was to determine if the loss was to the Li^+ ground state or if the metastables were being lost from the trap, either due to some type of reaction or to some mechanism which preferentially ejected metastable ions out of the trap. This was done by measuring the ion signal with, alternately, the laser continuously on or off. When the laser is continuously on, all metastables are forced into the ground state immediately after creation, before any nonradiative loss can occur, and the entire ion population, now in the ground state, decays with the ion storage lifetime. With the laser off, on the other hand, the ion signal initially is due to all of the ions, but as time progresses any loss of metastables other than to the ground state would show up as a slightly decreased ion signal. Since the metastable fraction is estimated to be near 10%, any differences in the two ion signals for $t > \tau_{3S_1}$ should be easily observable. In fact, no differences between the ion signals with the laser on or off were seen, to an accuracy of better than 1%. This strongly indicates that the metastables are simply decaying directly to the ground state by giving up their energy in some process other than photon

emission.

The general quenching process then appeared to be of the form

$$Li^+\left(2\,^3S_1\right) + X \rightarrow Li^+\left(1\,^1S_0\right) + X',$$

where X' could be related to X by ionization, dissociation, excitation, near-resonant capture into autoionizing Li $1s2snp$ states, or some combination of these. A knowledge of the background gas composition and of quenching cross sections would allow a calculation of the quenching rate. A quadrupole mass spectrometer was used to determine the principle residual gases and estimate their densities. A search through the literature revealed scattered information on the quenching of metastable helium and argon, the cross sections in most cases being quite large. For the purpose of checking whether quenching could reasonably account for the observed metastable loss rate, estimates of the quenching cross sections for metastable Li^+ were made, based on the helium and argon data, and are shown in Table 5. These cross sections are roughly $5\times$ the He^* thermal cross sections and are within a factor of ~ 2 of Ar^* cross sections. They were chosen on the basis that, at KeV energies, Li^+ cross sections for processes such as charge exchange are typically a factor 5-10 times larger than He cross sections. With this data we can estimate the quenching rate to be

$$A_{quench} \sim v \sum_i n_i \sigma_i.$$

Using $v \sim 1\times 10^{-6}$ cm/sec gives

$$A_{quench} \sim .12\ \text{sec}^{-1}.$$

Adding to this a storage lifetime of 20 sec, the estimated metastable lifetime becomes

$$\tau_{^3S_1} \sim 6\ \text{sec}.$$

This close agreement with observation is certainly not justified, considering the rough guesswork involved, but it does point out that the likely range of quenching cross sections is, indeed, sufficient to produce the observed lifetimes of the metastable state.

The final work necessary to verify the quenching hypothesis was actually to vary the residual gas composition and see whether an extrapolation to zero pressure could give a meta-

Table 5. Background Gas Density and Quenching Cross Section Estimates

Gas	Estimated Density (cm^{-3})	Estimated Quenching σ ($10^{-16} cm^2$)
H_2	2×10^7	10
CO	3×10^6	40
CH_4	1×10^6	60
H_2O	6×10^6	100
CO_2	1×10^6	200

stable lifetime in reasonable agreement with theory. Figure 41 shows the total metastable loss rate $1/\tau_{^3S_1}$ as H_2 and CH_4 are admitted to the system. In both cases a linear fit to the data is reasonable, though the relative nature of the pressure scale precludes any comparison of the slopes. A reference back to Figure 16 will show that the ion storage time is not strongly affected by either H_2 or CH_4, so the variation in the metastable loss rate seen here is very direct evidence of quenching. Similar results are seen for CO and CO_2. H_2O, for which the cross section is likely to be large, was not admitted due to concern that it might impair the vacuum.

The inability to vary simultaneously all of the background gases without altering their relative abundances, the evidence that most of the gases have fairly large quenching cross sections, and the somewhat poor accuracy of the individual measurements all contribute to an inability to extrapolate to zero pressure. It appears, however, that most, if not all, of the metastable loss can be attributed to nonradiative quenching. We have provided evidence that: (1) The $Li^+\left(2\,^3S_1\right)$ loss, by whatever mechanism, is to $Li^+\left(1\,^1S_0\right)$; (2) The decay rate is strongly dependent on the residual gas pressure. In view of this, we conclude that the metastable loss is due to a combination of spontaneous emission, direct loss from the trap, and nonradiative quenching. The possibility of a small decay rate for $2\,^3S_1$ ions which does not involve collisions (including trapping losses) or the emission of a photon cannot be definitely excluded, but the lack of any apparent mechanism renders this highly speculative.

D. PROCEDURES IN MEASURING THE RADIATIVE LIFETIME

The clarification and understanding of the nonradiative quenching cleared the way for the final measurement of the radiative lifetime along the lines discussed in Section III.C. The continued improvement in the photon detection signal-to-noise had reached essentially its limit, and the dark rate was sufficiently less than the spontaneous count rate to allow a 10% measurement of τ_{rad} in roughly one hour. The main consideration during several months of data collection was to locate any systematic errors.

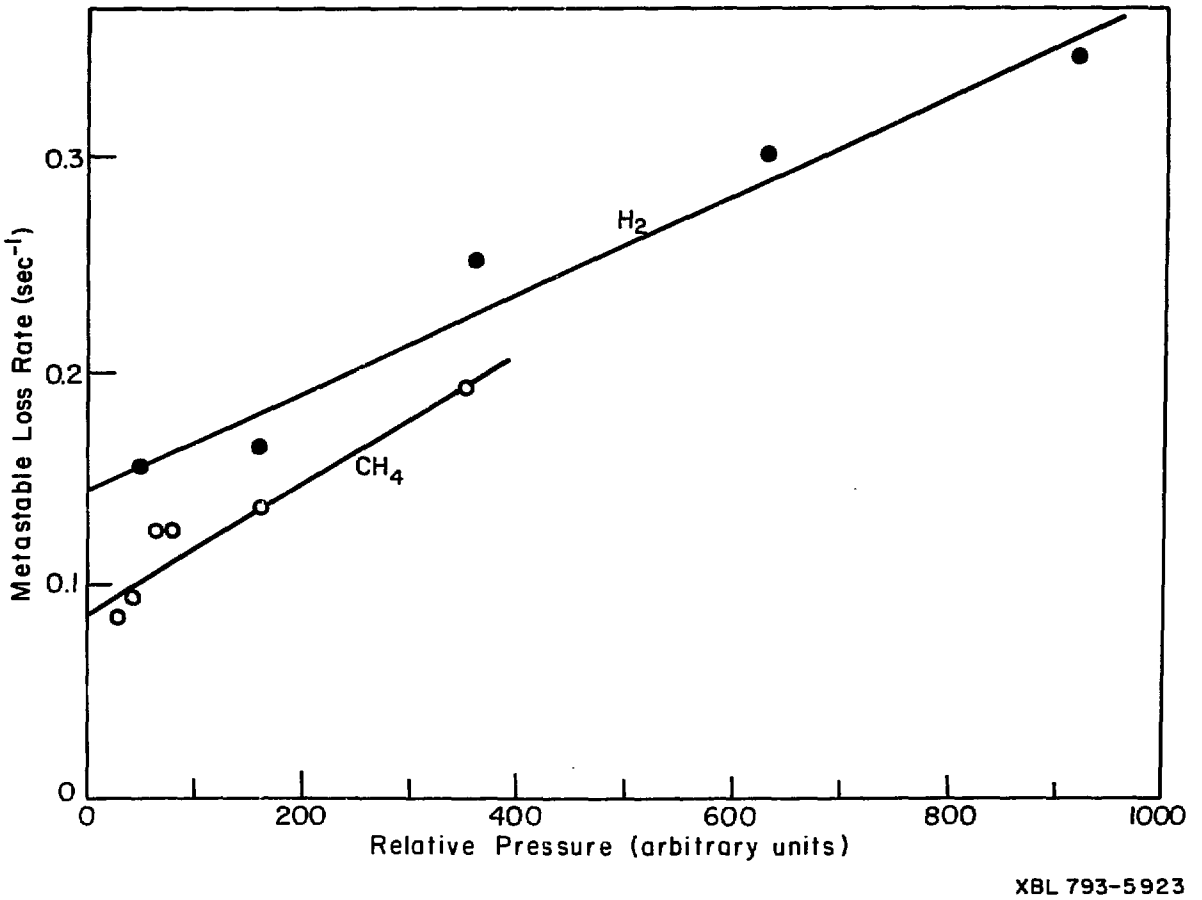


Figure 41. Total metastable loss rate as a function of the pressure of H_2 and CH_4.

As discussed in Section V.H.2., the basic sequence of events consisted of: (1) Measure the total metastable lifetime τ_{3S_1}; (2) Measure the spontaneous and laser-induced photon rates, S_1 and S_2, and the depletion time τ_d; (3) Re-measure τ_{3S_1} in order to get an average value; (4) Perform an analysis using the formulas developed in Section III.C. Only (2) will be discussed here since the other procedures have been covered previously. The determination of S_1, S_2, and τ_d follows the sequence: (1) Fill the trap with Li^+ ions; (2) Count spontaneous photons for a time T_1; (3) Turn on the laser and observe laser-induced photons for a time T_2; (4) Measure the ion signal for monitoring purposes; (5) Repeat everything, except that no Li^+ ions are stored, for background information. The monitoring consists of summing the laser-induced counts and the ion signals for periods of 20 cycles, then dividing the counts by the ion signal, to normalize for any variation in the number of ions stored, and printing the result. This normalized count rate varies only a few percent as long as the laser wavelength remains centered on the 2^3S_1 - 2^3P_1 transition. At the first sign of any wavelength drift, the computer is switched over to a laser adjustment program (see Section V.H.2.) where the problem is corrected, and the data collection is resumed.

A typical set of data, following background subtraction, was shown in Figure 38. In this case, T_1 = 1.0 sec and T_2 = 2.0 sec. During each cycle, the filling time is fixed by the necessity of trapping a large number of ions, while T_2 is fixed at $\simeq 5 \cdot \tau_d$ in order to minimize the error in determining S_2 and τ_d. T_1, however, is arbitrary; a large value increases the rate at which S_1 counts accumulate, but on the other hand it also decreases S_2 and lengthens the duty cycle. A numerical study of the signal-to-noise obtained in a fixed time period for various T_1, using a range of "typical" values for τ_{3S_1} as well as the various other count rates and noise levels, showed that $T_1 \simeq \frac{1}{2}\tau_{3S_1}$ was optimal. Since $\tau_{3S_1} \simeq 4$ sec for most conditions, a fixed value of T_1 = 2.0 sec was used for most data collection periods.

A major consideration is an accurate subtraction of the background. Since the spontaneous photon count rate is not substantially higher than the background rate, errors in the

background subtraction procedure can have a sizable effect on τ_{rad}. The laser-induced rate, being much larger, is not as sensitive to background errors. Since there have occasionally been suggestions of a slight curvature to the background, possibly an after-effect of detector charging during the electron pulse, the background subtraction is performed separately for periods T_1 and T_2. Since the counts in T_1 are summed, a slight background curvature is of no consequence as long as it behaves identically during data cycles and background cycles. Initially, the background was taken by opening the Li beam flag during the fill period but switching the trap's DC potential very negative so that no ions would be stored. The procedure adopted later was to maintain the normal DC voltage but not open the Li beam flag. This method is judged preferable since it allows residual gas ions which are trapped during the data cycle to be also trapped during the background cycle, and it also does not alter the electron beam trajectories any during the cycles. Several overnight runs which collected background counts only found a small but significant difference between the two methods, enough to shift τ_{rad} by $\simeq$1 sec. This difference was attributed to the slightly different electron trajectories obtained when the trap potential is switched, leading to somewhat different charging effects on surfaces and the detectors. All data used in the final averages were collected by the second method of not switching the potential, and they should not see this systematic effect.

Another problem is the possible existence of holes or tears in the aluminum foil filters. This would allow some escaping ions to be counted during the data cycle without any means of compensating for it during the background cycle. To check for any holes, the trap was operated with the laser on continuously and ions were stored for several seconds before the photon detectors were turned on. All metastables will have then been depleted, so any counts above the background rate would have to be attributed to escaping ions which were getting past the foils. This test was performed several times during the months of data collecting, and no additional counts were observed. We then conclude that the integrity of the foils was good throughout the entire period.

The only systematic problem encountered concerns the trap well depth and the electron energy. It was initially observed, using $^6Li^+$, that well depths D = 18 eV generally resulted in smaller values for τ_{rad} than did depths D = 8 eV. Subsequent investigation showed this effect to be more pronounced when low energy electrons ($\leqslant$ 300 V) were used at D = 18 eV. Data taken for D = 18 eV with electron energies $E_{elec} \geqslant 300$ volts were in reasonable agreement with the D = 8 eV data, and furthermore there was little, if any, dependence on E_{elec} for $E_{elec} \geqslant 300$ volts. We concluded that the stronger rf-fields at D = 18 eV were substantially perturbing the lower energy electrons, causing surfaces and the detectors to charge up slightly and leading to systematic errors. With either smaller rf-fields or larger electron energies, the electron trajectories are more nearly straight lines through the trap center, and this problem diminishes. All data used to obtain the final results used $E_{elec} > 300$ volts (usually 450 volts), and further errors are judged to be less than 5%.

Another problem related to the well depth occured for $^7Li^+$ ions. Because the hyperfine structure of $^7Li^+$ is much larger than for $^6Li^+$, the $2\,^3S_1$ - $2\,^3P_1$ resonance is smaller and narrower, a consequence of optical pumping. To obtain as much overlap as possible with the Doppler profiles, and thus make τ_d as small as possible, the laser was generally operated without the internal etalon. No problems were encountered when studying $^7Li^+$ with D = 18 eV, but with D = 8 eV the values of τ_{rad} were very erratic. Replacing the etalon restored the data consistency but required excessively long duty cycles since τ_d was much longer than usual ($\geqslant$ 1 sec). We concluded that the smaller Doppler widths at D = 8 eV reduced the resonance linewidth to the level (few hundreths of an Ångstrom) over which the laser wanders when running with only the birefringent filter. As a result, the laser was erratically tuning in and out of resonance. To avoid affecting the results, all $^7Li^+$ data taken at D = 8 eV without the etalon were excluded from the averages.

A primarily theoretical approach was undertaken to consider the possibility that optical pumping of the ions might affect the results. The principle concern is that an alignment of the $2\,^3S_1$ state would result in anisotropic photon emission and cause a systematic error in S_2.

The major parameters affecting optical pumping are the magnetic field and the angle of laser polarization with respect to the field. As is well known[43], the induced dipole created by the laser's electric field is destroyed by a uniform magnetic field when the precession frequency exceeds the radiative decay rate (this is known as the Hanle effect or magnetic depolarization). The pertinent condition for magnetic depolarization is

$$\alpha = \frac{2\pi\mu_B B}{h\gamma} >> 1,$$

where B is the field strength and γ the radiative decay rate. For the $2\,^3P_1$ states of Li^+ with $B \simeq 50$ gauss, $\alpha \simeq 20$, so depolarization should be complete in our experiment. One can further show (Appendix A) that, for the case of complete depolarization, laser beam polarization at an angle $\theta = \cos^{-1}\left(\frac{1}{\sqrt{3}}\right) \simeq 55°$ with respect to the magnetic field will not cause any alignment. Thus our signals, taken at $\theta = 55°$ and $B \geqslant 50$ gauss, should not exhibit any effects of anisotropy.

While we could not move our detectors about in order to verify an isotropic distribution of photons, we could perform some tests to check the ideas presented here. A simple observation is whether the magnetic field strength affects τ_{rad}, which it would if magnetic depolarization were incomplete. Several measurements over the range 40 - 60 gauss showed no effect. One observation at 75 gauss gave a somewhat lower value for τ_{rad}, though this was not statistically very significant, and the disturbance of the detectors by increasing magnetic fields could produce questionable results. A more decisive test was to measure the laser-induced counts, normalized against the ion signal, as a function of the polarization angle θ. This is shown in Figure 42, along with the predictions of Appendix A's optical pumping model. The satisfactory results of these tests allow us to be confident that the experimental conditions used while collecting data result in an isotropic distribution of laser-induced photons.

One final question is whether the $2\,^3S_1$ state itself is aligned during ion creation, causing an anisotropic emission of spontaneous magnetic dipole photons. Since at threshold the incident electron comes to rest and can carry away no angular momentum, various selection

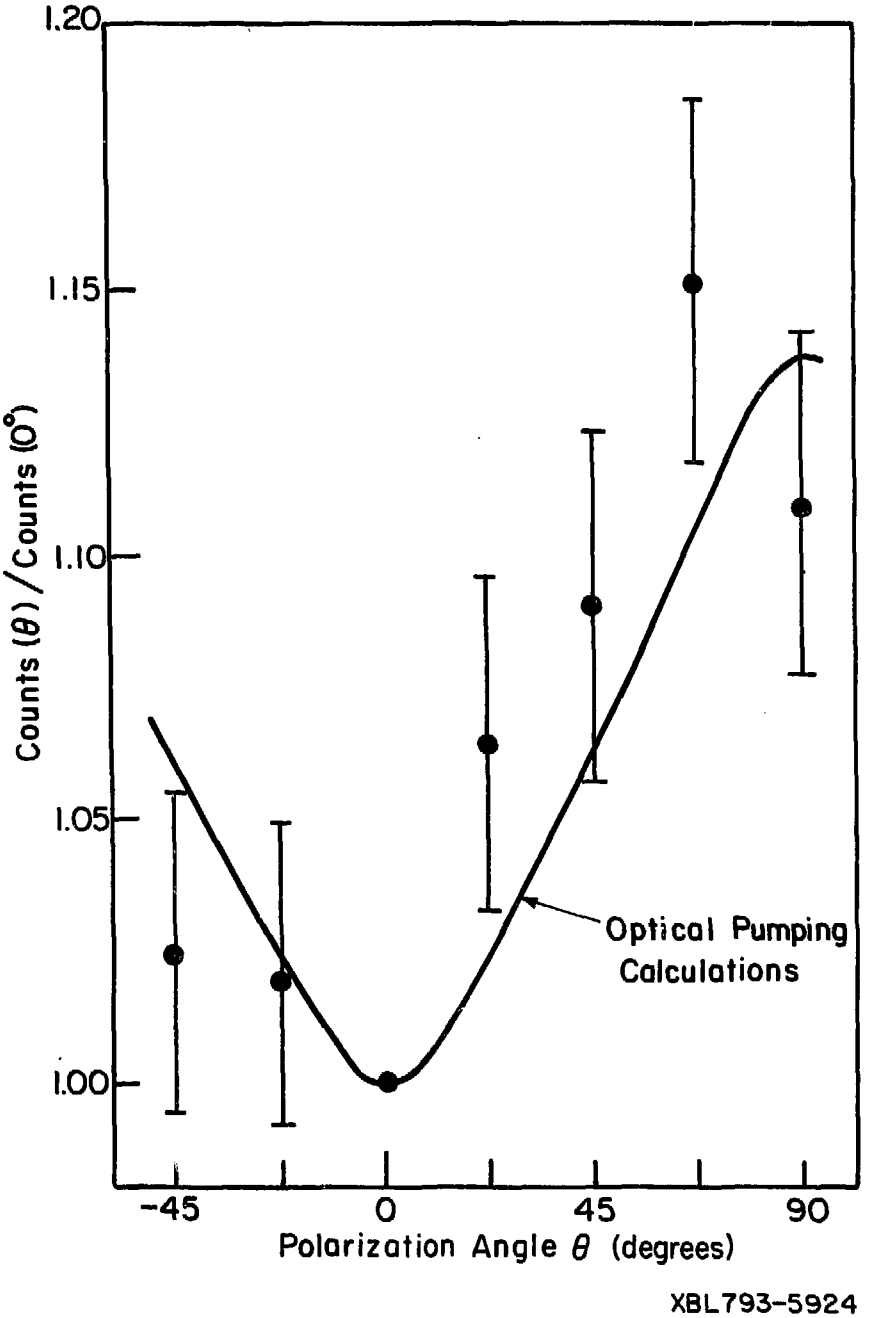


Figure 42. Integrated laser-induced photon count rate for various polarization angles, normalized to the rate at 0°. The solid curve is the prediction of the optical pumping model.

rules do indicate that the ion is aligned. But this diminishes away from threshold, and in our case of $E_{elec} >> E_{thresh}$, large alignment would not be expected. Nonetheless, for much of the data a short ($\simeq$10 msec) laser pulse was applied to the ions immediately following their creation. This has the effect of exciting each metastable to 2^3P_1 about 50 times and, because of the $\theta = 55°$ laser orientation, "unpumping" any initial alignment before counting begins. While this pulse caused no observable change in τ_{rad}, it was deemed a useful precautionary measure.

E. DATA REDUCTION AND ERROR ANALYSIS

The collection of radiative lifetime data had two distinct phases. During the first of these, many parameters were widely varied in order to isolate such effects as the dependence on the laser polarization angle. After understanding how to eliminate these major effects, the second phase produced the data used in obtaining the final figures. Other parameters varied during the second phase allowed an estimate to be made of probable errors. Since the major factor neglected during phase one was the polarization rotation, multiplying the phase one results by a theoretical correction factor of 1.08 should correct the offset introduced by this effect and give reasonable agreement with phase two. This is, indeed, the case, and supports the interpretation that the data remained generally consistent over the five month period during which it was obtained.

The final raw data for both isotopes are given in Table 6. The only phase two data not included in the final list are one $^6Li^+$ value taken at a higher magnetic field than usual and two $^7Li^+$ values which exhibited anomalous background behavior. A somewhat better feeling for the data is found by plotting it after detector and isotope corrections are made, as in Figure 43. The standard deviations for the distributions, indicating the general spread of results, are $\sigma\left(^6Li^+\right) = 4.2$ sec and $\sigma\left(^7Li^+\right) = 5.1$ sec. The mean of each distribution and the associated

Table 6. Summary of $^{6}Li^{+}$ and $^{7}Li^{+}$ Uncorrected Data

Run	τ ($^{6}Li^{+}$)
1	43.5 ± 4.5
2	53.1 ± 5.5
3	55.2 ± 6.3
4	44.0 ± 4.5
5	52.8 ± 7.4
6	51.0 ± 7.2
7	47.0 ± 6.2
8	43.1 ± 4.6
9	48.0 ± 5.6
10	49.0 ± 6.0
11	52.9 ± 6.4
12	49.8 ± 5.3
13	50.7 ± 6.0
14	47.8 ± 5.3
15	46.8 ± 4.9
16	51.1 ± 6.1
17	44.9 ± 4.5
18	47.0 ± 5.0
19	51.5 ± 5.8
20	53.2 ± 5.5
21	57.3 ± 6.5
22	69.9 ±17.1
23	49.6 ± 4.6
24	52.1 ± 4.9
25	40.1 ± 3.2
26	44.1 ± 3.7
Average	47.7 ± 1.0 sec

Run	τ ($^{7}Li^{+}$)
1	48.2 ± 4.2
2	50.4 ± 4.1
3	56.5 ± 7.5
4	49.5 ± 3.7
5	53.5 ± 4.6
6	59.9 ± 4.9
7	59.5 ± 7.2
8	56.9 ± 7.6
9	46.7 ± 5.0
10	56.6 ± 7.5
11	48.5 ± 6.4
12	50.0 ± 6.2
13	60.5 ± 6.9
14	55.7 ± 5.8
15	61.6 ± 6.2
16	53.2 ± 5.3
17	58.2 ± 7.0
18	49.1 ± 6.3
19	52.8 ± 5.3
20	52.5 ± 5.4
21	45.1 ± 4.1
22	55.1 ± 6.3
23	55.6 ± 5.8
24	42.8 ± 4.1
25	57.5 ± 6.8
26	49.7 ± 6.4
27	53.6 ± 5.0
28	50.6 ± 5.0
29	58.8 ± 7.3
30	49.9 ± 5.6
31	45.8 ± 4.4
32	62.1 ± 6.2
33	57.6 ± 7.4
Average	52.0 ± .9 sec

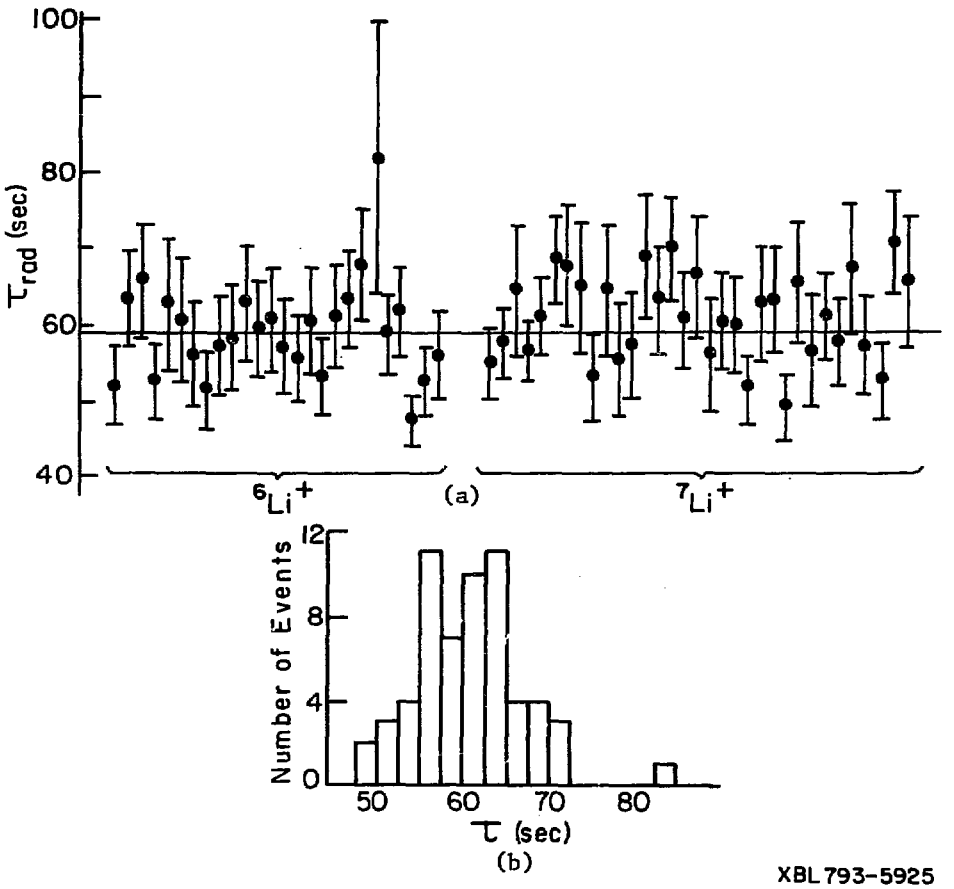


Figure 43. (a) Corrected $^6Li^+$ data and $^7Li^+$ data used in the final analysis. (b) Histogram of the data.

error of the mean were determined by the weighted averages[26]

$$\bar{\tau} = \frac{\sum_i \frac{\tau_i}{\sigma_i^2}}{\sum_i \frac{1}{\sigma_i^2}} \qquad \bar{\sigma}^2 = \frac{1}{\sum_i \frac{1}{\sigma_i^2}}.$$

The error σ_i associated with each value was determined by the analysis programs, as indicated in Sections III.C. and V.H.2. In all cases, the error is almost entirely due to the statistical error associated with S_1.

Two corrections must be made to convert the raw data averages into measured lifetimes. The first of these, which applies only to $^6Li^+$, arises from the fact that the lithium composition is 95.6% ^{6}Li and 4.4% ^{7}Li. (The $^7Li^+$ data used a lithium source which is > 99.9% ^{7}Li.) The small number of $^7Li^+$ ions present contribute spontaneous M1 photons to S_1, but their $2\,^3S_1$ - $2\,^3P_1$ transition is isotopically shifted away from the laser, which is tuned to the $^6Li^+$ transition, so they do not contribute to S_2. To correct for the increased value of S_1, we use the correction factor $\tau_{corrected} = \tau_{uncorrected}/.956$. This raises the $^6Li^+$ value to

$$\tau(\textit{isotope corrected}\ ^6Li^+) = 49.9 \pm 1.0 \text{ sec.}$$

A possible systematic error to this correction arises since the relative number of ions of different masses which are stored is not always in the same proportions as the neutral concentrations. Though the ratio of the $^7Li^+$ and $^6Li^+$ ion signals was roughly 1/25, the $^7Li^+$ signal was too noisy to make the measurement accurately. It is estimated that the actual concentration of $^7Li^+$ was 4.4 ± 2.0%, causing a 2% contribution to the systematic errors in τ_{rad}.

The second correction, which applies to both isotopes, is the factor $\frac{\epsilon_{210}}{\epsilon_{202}} = \frac{1}{.87}$ that comes from the photon detector calibration, discussed in Section V.F.2. We have, then,

$$\tau_{rad} = \frac{\epsilon_{210}}{\epsilon_{202}} \tau(\textit{isotope corrected}),$$

which gives

$$\tau_{rad}\left(^6Li^+\right) = 57.4 \text{ sec} \qquad \tau_{rad}\left(^7Li^+\right) = 59.8 \text{ sec.}$$

As discussed previously, the estimated calibration error is 6%. This has to be treated as a

systematic error since it does not change from run to run.

While, as we have seen, the $2\,^3S_1$ quenching rate and, to a lesser extent, the total ion storage time are dependent on the residual gas pressure, the radiative lifetime should not be. This was tested by admitting H_2, CH_4, H_2O, CO, and air, the main residual gas constituents, and varying the partial pressure of each over a range of at least a factor of ten. As an example, the trap loss rate, the quenching rate, and the radiative rate as a function of CO pressure are all shown in Figure 44. No evidence for any pressure dependence of τ_{rad} was found. This was an important test to verify the assumption that the radiative lifetime could be determined independently of other simultaneous loss processes.

Other parameters which might cause systematic errors were varied in an attempt to set limits on their effects. A possible polarization angle error of a few degrees would produce an error $\simeq$2%, while a residual anisotropy from incomplete magnetic depolarization could also contribute $\simeq$2%. Unresolved problems with the background subtraction produce an error $\leqslant$ 2%, and the somewhat more serious well depth - electron energy problem discussed in the previous section could still cause an error $\simeq$5%. Since the laser-induced photons come from the volume occupied by the laser beam while spontaneous photons come from the entire ion cloud, a slightly different geometrical factor for the two cases could exist. This would be combined with a possible slight light pipe reflectivity difference between the two wavelengths. Variation of the laser beam diameter puts $\simeq$3% limits on collection errors. A possible error in the $^7Li^+$ data exists since most of it was taken without the internal laser etalon in the cavity. Slight wavelength drifts effect both S^2 and τ_d, but the wavelength was monitored closely enough to limit any error to $\leqslant$ 2%. The use of the etalon makes this a negligible source of error for the $^6Li^+$ data.

Other conceivable sources of error have been considered negligible if, either through observation or theory, they contribute at less than the 1% level. This includes such things as the number of ions, the residual gas, and the laser power and linewidth. One could also consider such systematic effects as emission due to Stark-induced mixing of $2\,^3S_1$ with $2\,^3P_1$ in the

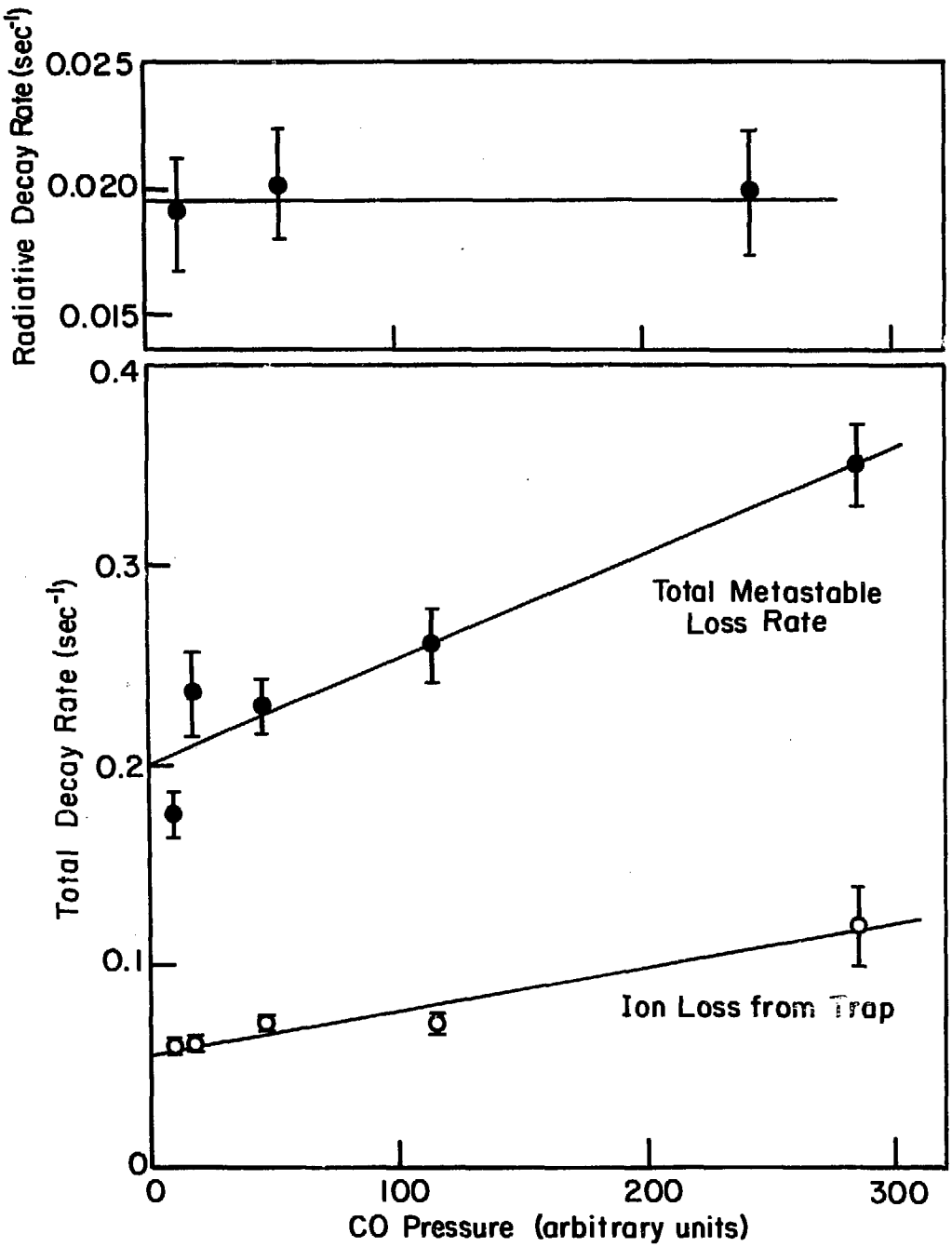


Figure 44. Ion storage loss rate, total metastable loss rate, and metastable radiative decay rate as a function of the pressure of CO.

trap fields or radiative collisions, but estimates show these type of effects to be several orders of magnitude too small to be of consequence.

The results of the data reduction and error analysis are shown in Table 7. An average of the $^6Li^+$ and $^7Li^+$ data yields a value of 58.6 sec for the radiative lifetime. Assigning an appropriate error to this result is not an easy matter. The errors shown in Table 7 are, with the exception of the 2% statistical error, all systematic errors. Their effect on the result is always the same, but we cannot correct for them since we do not know whether they increase or decrease τ_{rad}. If they combined randomly we could use an RMS average, but there is no *a priori* justification for this. A worst-case approach is to consider that they might all affect τ_{rad} the same way, in which case we would have to add the errors. We choose to adopt a conservative approach and feel we can assert, with 95% confidence, that the error in our result is no worse than the sum of the individual errors, combined in an RMS fashion with the statistical error. The 12.9 sec error deduced in this manner does not differ substantially from a 2σ error of 11.7 sec found by a straightforward RMS calculation. The final result of our analysis is then taken to be

$$\tau_{rad} = 58.6 \pm 12.9 \text{ sec.}$$

The quoted error represents 95% confidence levels. This conforms to the practice followed in previous measurements of $2\,^3S_1$ lifetimes and allows a direct comparison with other results.

Table 7. Data Averaging and Error Analysis

Raw data average × Calibration factor (× Isotope factor for $^6Li^+$)

$^6Li^+$: τ_{rad} = 57.4 sec

$^7Li^+$: τ_{rad} = 59.8 sec

Average: τ_{rad} = 58.6 sec

Source of Error	Estimated Contribution
Detector calibration	6%
Well depth/electron energy	5%
Background subtraction	2%
Magnetic field dependence	2%
Laser polarization angle	2%
Laser beam size	3%
$^6Li^+$: Isotope correction $^7Li^+$: Laser wavelength drift	2%
Maximum systematic error	22%
Statistical error	2%
Total RMS error	22%

Final result (95% confidence level): τ_{rad} = 58.6±12.9 sec

VII. CONCLUSION

This thesis has described, in considerable detail, not only the actual measurement of the radiative lifetime, but also many peripheral issues which are deemed important for a careful assessment of the results. The experimental effort expended to understand the ion trap's storage properties was very worthwhile in terms of learning how to estimate collision processes, ion cloud - laser beam overlap, Doppler widths, etc. Detailed studies of the optical pumping and of the nonradiative quenching were equally valuable. We conclude that we now have achieved an adequate knowledge of the ions and their many interactions with the different parts of the experiment, and have made a measurement of the Li^+ $2\,^3S_1$ radiative lifetime, τ_{rad}, with a well-characterized uncertainty.

It is now of interest to look back at Figure 2 and compare the experiments to date with theory. All of the error bars in this figure represent 95% confidence levels. Considering that the lifetimes measured have spanned nearly 14 orders of magnitude, the general agreement of theory and experiment is fairly impressive. Still, it is somewhat disturbing that both Z = 2 (He) and Z = 3 (Li^+) require 2σ error bars to reach agreement, and both experimental lifetimes are longer than theory predicts. Since the theoretical decay rate scales as Z^{10}, any other process scaling with a lower power of Z could be a contributing factor at low Z while not observed in the higher Z beam-foil experiments. No theoretical hypothesis has been advanced, though, for any process which would inhibit the decay. Drake's general theory[7], given in Section II.B, has been confirmed by at least two other independent calculations. Feinberg and Sucher[44] used a more rigorous QED approach which yielded the same final expression for the transition matrix element, while a relativistic Dirac-Hartree-Fock calculation by Johnson and Lin[45] only differs by .1 sec (τ_{theory} = 49.1 sec for Li^+, as compared to Drake's 49.0 sec). Obvi-

ous competing processes, such as hyperfine-induced decays, could only shorten the lifetime, and they can be easily estimated to be several orders of magnitude too small to be of importance.

Since all of the data are within 2σ of the theoretical values and since no basis exists for doubting the theory or the experiments (at least at low Z), it seems most reasonable to conclude that the theory of M1 decay has been confirmed. However, further work, both experimental and theoretical, would not be without merit as long as the puzzles remain of nonexponential behavior at high Z and possibly longer-than-theoretical lifetimes at low Z. A particularly attractive candidate is Be^{++}, with a theoretical lifetime of 1.78 sec. Ion storage at a pressure of $\simeq 10^{-10}$ torr should permit τ_{rad} to be measured directly from spontaneous decay curves, providing direct information on the shape of the curve and leading to a more precise value for the lifetime by avoiding many of the systematic errors which have been inherent in the experiment reported here.

APPENDIX A. OPTICAL PUMPING CALCULATIONS

A. THE MAGIC ANGLE

The details of the ion's interaction with the laser beam can, to a large extent, be ignored as far as this experiment is concerned. However, the polarization of the light can become important since the absorption rates (because of ΔM selection rules) are polarization dependent. This can lead to a situation in which the magnetic sublevels of the various hyperfine levels are not equally populated, and the 202Å intercombination radiation ($2\,^3P_1$ - $1\,^1S_0$) would then be anisotropic. It is important to determine the conditions under which this can be avoided. The results of the following analysis are quite general.

Consider excitation by a linearly polarized light beam from a level F to level F'. Each state $|F'M'>$ decays spontaneously to state $|FM>$ with probability $A_{F'M',FM}$, here normalized to

$$\sum_M A_{F'M',FM} = 1.$$

Selection rules require $A_{F'M',FM}$ to vanish unless $\Delta M = 0, \pm 1$. We consider the light beam, of total intensity I, to impinge along the x-axis, with the plane of polarization at an angle α to the z-axis, as shown in Figure 45. The z-component of the electric field **E** will induce $\Delta M = 0$ transitions at a rate

$$R_{F'M',FM'} \propto I_z A_{F'M',FM'} \sin^2(90°) = I A_{F'M',FM'} \cos^2\alpha,$$

where the factor $\sin^2\theta$, with here $\theta = 90°$, is the solid angle factor for $\Delta M = 0$ emission and absorption. Similarly, the y-component of **E** induces $\Delta M = 1$ transitions at a rate

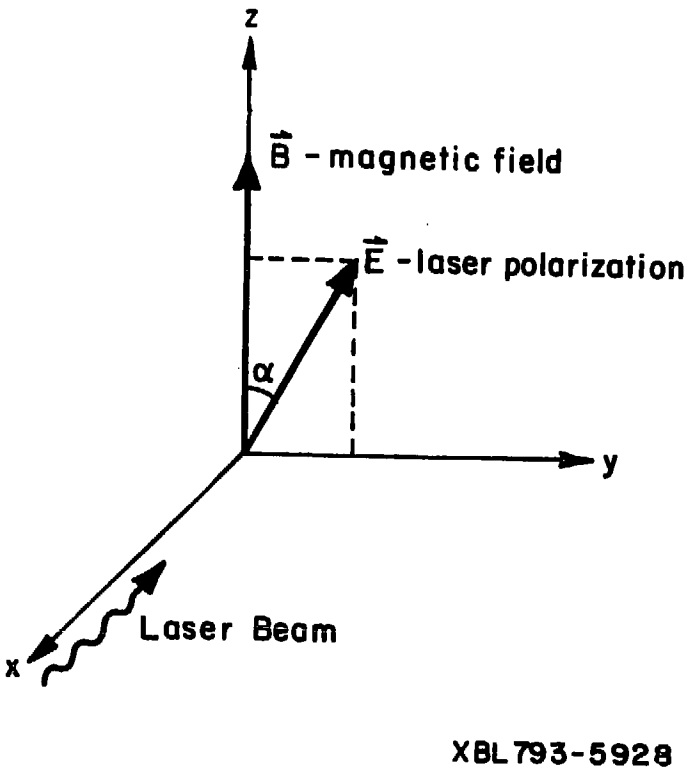


Figure 45. Geometry of the laser beam and magnetic field.

$$R_{F'M',FM'-1} \propto I_y A_{F'M',FM'-1} \cdot \frac{1}{2}\left[1 + \cos^2(90°)\right] = \frac{1}{2} I A_{F'M',FM'-1} \sin^2\alpha$$

with the result for $\Delta M = -1$ identical except for replacing $M'-1$ by $M'+1$. If the lower level F has all sublevels equally populated, then the population of $|F'M'>$ can be written as

$$N_{F'M'} \propto \frac{1}{2}\left[A_{F'M',FM'+1} + A_{F'M',FM'-1}\right] \sin^2\alpha + A_{F'M',FM'} \cos^2\alpha \,.$$

Using the above sum rule for the transition probabilities, this can be rewritten as

$$N_{F'M'} \propto \frac{1}{2}\left[\sin^2\alpha + \left(3\cos^2\alpha - 1\right) A_{F'M',FM'}\right].$$

At the "magic angle" α_0 given by

$$\alpha_0 = \cos^{-1}\frac{1}{\sqrt{3}} = 54.7°,$$

the coefficient of $A_{F'M',FM'}$ vanishes and $N_{F'M'}$ is independent of M'. Hence all upper levels are equally populated. If we further assume that there exists an axial magnetic field strong enough to destroy, by magnetic depolarization, any induced coherence between the two states excited by E_y (B $\geqslant$ 10 gauss for Li^+), then the radiation emitted by level F' will be isotropic and unpolarized. This result, which will be further substantiated in the next section, can be easily generalized to the case of several lower levels F_1, F_2,... and upper levels F_1', F_2',...

B. THE OPTICAL PUMPING EQUATIONS

Even though knowledge of the magic angle is all that is really necessary for this experiment, it was felt useful to investigate the details of any optical pumping, particularly for the purpose of understanding the $2\,^3S_1$ - $2\,^3P_1$ lineshape and to establish that the intercombination radiation is isotropic when pumping at the magic angle. The major factors which we wish to consider are: the Li^+ hyperfine structure; the laser beam's power, linewidth, shape, and polarization; and the ions' temperature and density profile. We ignore stimulated emission, which is negligible for the laser spectral density used, and we also assume that relaxation times are much smaller than optical pumping times. The $2\,^3P_1$ - $1\,^1S_0$ intercombination transition is considered to have no effect on the relative level populations. The calculations are for the case

of an axial magnetic field strong enough to destroy, by magnetic depolarization, any coherence between the upper levels.

Consider the states of $2\,^3P_1$ to have populations $N_{F'M'}$ and those of $2\,^3S_1$ to have populations N_{FM}. Then the rate of downward transitions (spontaneous emission) is

$$\text{Rate}(N_{F'M'} \rightarrow N_{FM}) = A_{F'M',FM}\, N_{F'M'},$$

while for upward transitions (absorption) we have

$$\text{Rate}(N_{FM} \rightarrow N_{F'M'}) = \delta\beta\eta A_{F'M',FM} f_{F'F} N_{FM}.$$

Here β is the relation between the Einstein A and B coefficients, involving the laser spectral density[43], η is the fraction of ions in the laser beam, $f_{F'F}$ is the fraction of ions with their $F - F'$ transition Doppler shifted onto the laser profile, and δ is the laser polarization factor

$$\delta = \begin{cases} 3\cos^2\alpha & \Delta M = 0 \\ \dfrac{3}{2}\sin^2\alpha & \Delta M = \pm 1 \end{cases}$$

with the geometry the same as in Figure 45. The relative transition probabilities obey the sum rule

$$\sum_{FM} A_{F'M',FM} = 1.$$

The fraction of ions in the laser beam, η, is found if we assume (see Appendix B) that the ion density profile, using cylindrical coordinates, is given by

$$\eta(r,z) = \frac{1}{\pi^{3/2}\Delta^3}\, e^{-(r^2+z^2)/\Delta^2}$$

and that the laser beam profile is cylindrical with radius R. Then

$$\eta = 2\pi \int_{-\infty}^{\infty} dz \int_0^R r\eta(r,z)\, dr = 1 - e^{-R^2/\Delta^2}.$$

Since generally $R << \Delta$, the cylindrical beam assumption should be reasonably good.

To determine $f_{F'F}$, we assume that the laser's spectral profile is one of constant intensity within bandwidth $\Delta\lambda$ and zero elsewhere. Then integrating over a piece of the Doppler profile,

$$f_{F'F} = \sqrt{\frac{m}{2\pi kT}} \int_{v_-}^{v_+} e^{-mv_x^2/2kT} dv_x,$$

where

$$\nu_{\pm} = \frac{c}{\lambda}\left(\lambda_{F'F} - \lambda \pm \frac{\Delta\lambda}{2}\right).$$

Writing $3kT = E$, where $E = 3(\Delta/r_0)^2 eD$ (see Appendix B), we get

$$f_{F'F} = \frac{1}{2}\left\{\mathrm{erf}\left[\frac{c}{\lambda}\sqrt{\frac{3m}{2E}}\left(\lambda_{F'F} - \lambda + \frac{\Delta\lambda}{2}\right)\right] - \mathrm{erf}\left[\frac{c}{\lambda}\sqrt{\frac{3m}{2E}}\left(\lambda_{F'F} - \lambda - \frac{\Delta\lambda}{2}\right)\right]\right\}.$$

Writing β in terms of wavelengths, we have

$$\beta = \frac{\lambda^5 P}{8\pi^2 hc^2 R^2 \Delta\lambda},$$

where P is the laser power. We then define

$$\gamma_{F'F} = \beta\eta f_{F'F},$$

and, using the sum rule, write the coupled equations as

$$\dot{N}_{FM} = \sum_{F'M'}\left[-\delta\gamma_{F'F}A_{F'M',FM}N_{FM} + A_{F'M',FM}N_{F'M'}\right]$$

$$\dot{N}_{F'M'} = -N_{F'M'} + \sum_{FM}\delta\gamma_{F'F}A_{F'M',FM}N_{FM}.$$

The relative transition probabilities are generally given by

$$A_{(IJ')F'M',(IJ)FM} = (2J'+1)(2F+1)(2F'+1)\begin{pmatrix} F & 1 & F' \\ -M & \Delta M & M' \end{pmatrix}^2 \begin{Bmatrix} J & J' & 1 \\ F' & F & I \end{Bmatrix}^2,$$

though in $^7Li^+$ the large hyperfine interaction mixes different J states enough that it is preferable to use empirical values or a more detailed expression. Since each ion has to be excited $\simeq$1200 times before producing a detectable intercombination photon, no transient behavior is observed. The steady state situation is solved for by setting $\dot{N}_{FM} = \dot{N}_{F'M'} = 0$, arbitrarily setting a particular $N_{F_0M_0} = 1$, and solving the remaining simultaneous equations in terms of $N_{F_0M_0}$. The solutions can then be normalized to sum to the total number of metastables, N_0.

Having solved for the N_{FM} and $N_{F'M'}$ for a given set of parameters, we can determine the fraction of ions $\epsilon_{F'M'}$ in each $2\,^3P_1$ level. Then

$$\epsilon = \sum_{F'M'}\epsilon_{F'M'}$$

is the total fraction of metastable ions in $2\,^3P_1$. Since each $|F'M'>$ has the same total transition

probability A' for decaying to the ground state $1\,^1S_0$, the metastable population time dependence is $\exp(-\epsilon A' t)$. The angular distribution of the intercombination radiation is given by

$$\frac{dN}{d\Omega} = \frac{3N_0}{8\pi\epsilon A'} \sum_{F'M'} \epsilon_{F'M'} \left[A'_{F'M',IM'} \sin^2\theta + \frac{1}{2}\left(A'_{F'M',IM'+1} + A'_{F'M',IM'-1} \right)\left(1 + \cos^2\theta\right) \right],$$

where $A'_{F'M',IM}$ notes that $F = I$ is the only hyperfine level of the ground J=0 state. The A' values can be expressed by 3-j and 6-j symbols, similar to the A values.

C. RESULTS OF THE CALCULATIONS

The simultaneous equations are easily solved numerically once all of the coefficients are evaluated in terms of the various parameters. Detailed studies have been carried through for $^6Li^+$. The laser depletion rate, $\epsilon A' = 1/\tau_l$, is found to be proportional to the laser power P, as expected when far from saturation. The power normalized lineshape $\frac{1}{\tau_l P}$ compares well with measurements, shown in Figure 39, and is considerably different than an absorption lineshape. In addition, the distribution of ions in the $2\,^3S_1$ levels conforms to the simple physical description given in Section VI.B. Increasing the well depth from D = 8 eV to D = 18 eV leads to a larger and broader lineshape, also confirmed by measurements.

Perhaps of more direct concern to this experiment is the effect of the angle of polarization, α. Only at the magic angle $\alpha_0 = \cos^{-1}\left(\frac{1}{\sqrt{3}}\right)$ was the radiation found to be isotropic, in agreement with the argument of Section A. The integrated count rate at $\theta = 90°$ (horizontal plane) was computed for several values of α and compared to measurements. The results were shown in Figure 42 and provide satisfactory evidence for the validity of these calculations.

It is reasonable to conclude that we now have a good understanding of the optical pumping process occuring in Li^+ when magnetic depolarization is complete. The low magnetic field case, where coherence effects lead to azimuthal asymmetries, is also interesting, both experimentally and theoretically. To include coherence, however, a general density matrix

approach would be more appropriate.

APPENDIX B. MEASUREMENTS OF THE ION DENSITY DISTRIBUTION

A. THE LASER SCANNING TECHNIQUE

An understanding of the ion cloud dynamics, storage times, Doppler widths, and many other details is greatly enhanced by a knowledge of the ion density distribution. An early suggestion by Dehmelt[27] was that the ions reach a steady state distribution where the space-charge forces and trapping forces just balance. In this low temperature limit, the ions fill the potential well at a constant density up to a well-defined ion cloud radius, rather like water in a bowl. This is seen in the T = 0 curve of Figure 18, and this was, indeed, the behavior observed for the trapping of charged metallic dust particles[31]. For atomic and molecular ions, however, considerable rf-heating due to their light mass invalidates this idea, and measurements by bolometric[46] and linewidth[47] techniques had indicated a temperature $T \sim 10^4$ K for D $\simeq$ 10 eV. Theoretical work by André[39] as well as the simple model given in Section IV.C.2. suggested a Gaussian distribution, but prior to this work there was no experimental evidence for this.

The experimental procedures were essentially identical to those described in detail in this thesis. The primary addition was a small mirror that was mounted on the movement of a standard relay. The relay was driven by a sinusoidal voltage at its mechanical resonant frequency of $\simeq$50 Hz and was used to scan rapidly the laser beam across the trap in the horizontal plane. The observed 202Å intercombination photons were then stored in a multichannel scaler whose timebase was synchronized with the scan. Only the center portion of a scan with width $\simeq$10 cm actually intersected the ion cloud, so the scan was quite linear in time during the interaction. After passing through the trap, the scan fell on a plate containing narrow slots

oriented normal to the scan plane and spaced .10 inch apart. The output of a photodiode, mounted behind the plate, was a series of pulses which were used to calibrate the channel number in terms of the laser beam's distance from the trap's z-axis.

The signal stored in each channel is proportional to the integral of the density along the laser beam, at the particular position corresponding to that channel. If the laser propagates in the x-direction and the scan plane is at a height z above the trap center, then channel i, corresponding to position y_i, has signal

$$S_i(y_i,z) = C \int_{-\infty}^{\infty} n(x,y_i,z)\,dx\,.$$

If we utilize the cylindrical symmetry, the general form for the signal can be written as

$$S(y,z) = 2C \int_{y}^{\infty} \frac{rn(r,z)}{\sqrt{r^2 - y^2}}\,dr\,.$$

This integral equation for $n(r,z)$ can be solved by using the Abel transforms[38], resulting in

$$n(r,z) = \frac{-2}{\pi C r} \frac{d}{dr} \int_{r}^{\infty} \frac{yS(y,r)}{\sqrt{y^2 - r^2}}\,dy\,.$$

Both for the previously mentioned theoretical reasons and as observed, $n(r,z)$ is very nearly Gaussian. If we parameterize the data, using least squares techniques, as

$$S(y,z) = S_0 e^{-(y/\Delta)^2},$$

then the integral can be performed analytically and yields

$$n(r,z) = \frac{2S_0}{\sqrt{\pi} C \Delta}\, e^{-(r/\Delta)^2}.$$

In practice, only the parameter Δ is of interest, since the leading coefficient can be obtained by normalization.

B. EXPERIMENTAL RESULTS

A typical set of data is shown in Figure 46, along with the fitted Gaussian used to determine Δ. Approximately one hour is needed to generate such a curve. The apparent structure seen near channel 85 is a shadow caused by one of the heavy gauge copper wires of the ring electrode; these points are excluded from the fitting program.

Since the number of ions created occasionally fluctuates as much as 30%, it was important first to see how the ion radius Δ varies with the number of ions. With the possible exception of very small numbers of ions, no dependence on the ion number was observed. This supports the assumption that space-charge effects are negligible for the high temperature region in which the rf-trap operates. All subsequent data were taken with a sufficient number of ions to insure that no errors existed due to ion fluctuations.

Data taken for different spherical wells were shown in Figure 17. The observed values of Δ provide the basis for the assertion that T ≃ 5000 K. This was determined by averaging the potential energy over a Gaussian ion cloud and using the Virial Theorem for a harmonic oscillator, resulting in

$$E = 3kT = 3\frac{\Delta^2}{r_0^2} eD .$$

Further data taken with the more general ellipsoidal potential well

$$\phi_{eff} = \frac{r^2}{r_0^2} D_r + \frac{z^2}{z_0^2} D_z$$

verified that the ion cloud remained a Gaussian of the form

$$n(r,z) = n_0 \exp\left[-\left(\frac{r}{\Delta_r}\right)^2 - \left(\frac{z}{\Delta_z}\right)^2\right].$$

When $D_z < D_r$, the ion cloud minimizes its energy by spreading out along the z-axis and assuming a cigar-like shape. Likewise, $D_z > D_r$ results in a pancake-like shape. A final observation, which would have been difficult to verify without using the laser to "take a picture" of

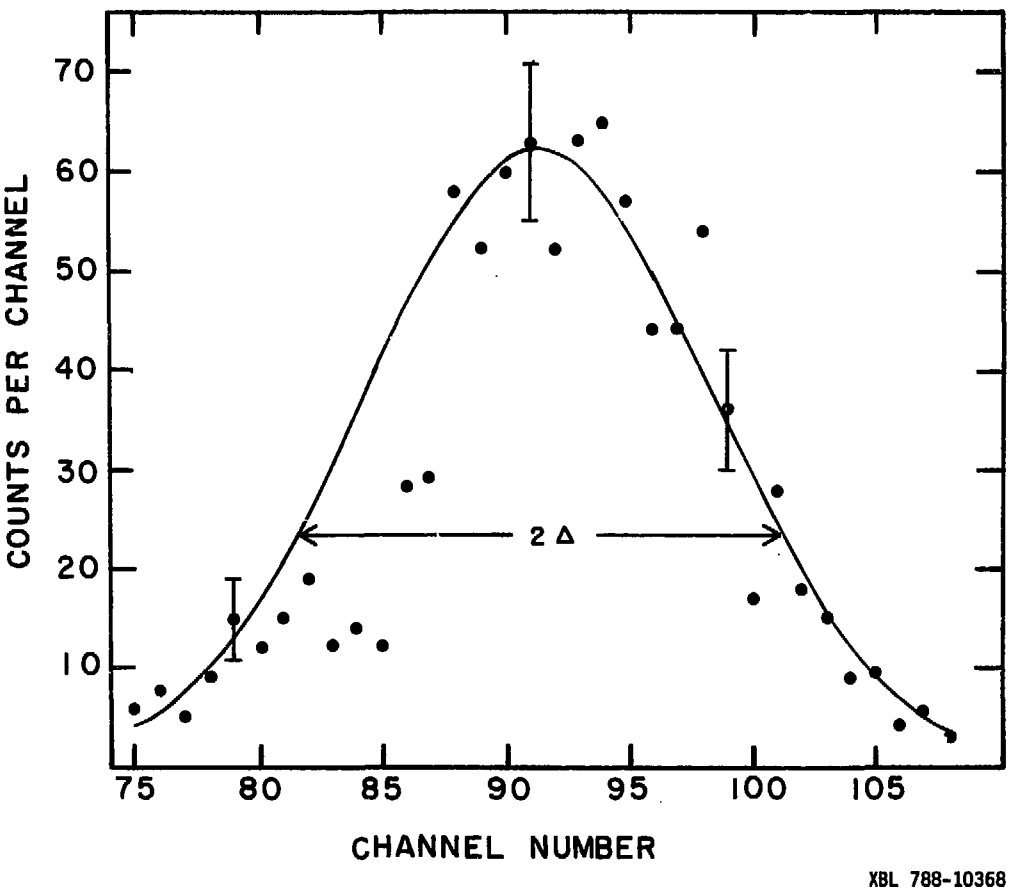


Figure 46. Typical laser scanning data and least squares fitted Gaussian.

the ion cloud, was that the addition of a DC voltage to one endcap electrode could shift the ion cloud $\simeq \pm .5$ cm along the z-axis without affecting the cloud's shape.

All observations were consistent with the model of a Gaussian ion distribution at a temperature of a few thousand degrees. This provides strong evidence for assuming that the ions are maintained in a quasi-equilibrium by being in contact with an effective heat reservoir determined by the background molecules and the rf-field. The knowledge of distributions and temperatures gained here was very valuable for the optical pumping calculation of Appendix A.

ACKNOWLEDGEMENTS

I wish to thank my thesis director and research advisor, Professor Howard Shugart, for having suggested this experiment and for providing constant support and encouragement. His assistance with the computer interfacing is especially appreciated.

My deepest thanks go to Dr. Michael Prior, who has worked directly with me on every aspect of this experiment, from beginning to end, and provided countless ideas and suggestions. The many techniques of scientific research which I have learned are due to his guidance.

I wish, also, to thank the many members of the Atomic Physics Group for their support, in particular the help and advice rendered, often unknowingly, by Professor Eugene Commins, Dr. Steven Chu, Mr. Pat Yarnold, and Mrs. Virginia Lam. The assistance of Dr. Frank Paresce, of the U.C. Space Sciences Laboratory, with calibration of the detectors is also acknowledged.

Finally, a special thanks to my wife, Jean, for her constant devotion and encouragement, and for sharing the often frustrating but always interesting life of a graduate student.

This work was supported by the Division of Chemical Sciences, Office of Basic Energy Sciences, U.S. Department of Energy under contract No. W-7405-Eng-48.

REFERENCES

[1]A.H. Gabriel and C. Jordan, Nature **221**, 947 (1969).

[2]G. Breit and E. Teller, Astrophys. J. **91**, 215 (1940).

[3]M. Goeppert, Naturwiss. **17**, 932 (1929); M. Goeppert Mayer, Ann. d. Phys. **9**, 273 (1931).

[4]G.W.F. Drake, G.A. Victor, and A. Dalgarno, Phys. Rev. **180**, 25 (1969).

[5]H.R. Griem, Astrophys. J. **156**, L103 (1969).

[6]C. Schwartz, unpublished work (1970).

[7]G.W.F. Drake, Phys. Rev. A3, 908 (1971).

[8]R. Marrus and R.W. Schmieder, Phys. Lett. **32A**, 431 (1970).

[9]R.W. Schmieder and R. Marrus, Phys. Rev. Lett. **25**, 1245 (1970).

[10]H.W. Moos and J.R. Woodworth, Phys. Rev. Lett. **30**, 775 (1973).

[11]H. Gould, R. Marrus, and P. Mohr, Phys. Rev. Lett. **33**, 676 (1974).

[12]J.R. Woodworth and H.W. Moos, Phys. Rev. **A12**, 2455 (1975).

[13]J.A. Bednar, C.L. Cocke, B. Curnutte, and R. Randall, Phys. Rev. **A11**, 460 (1975).

[14]D.L. Lin and L. Armstrong, Jr., Phys. Rev. **A16**, 791 (1977).

[15]J. Sucher, in *Atomic Physics 5*, p.415, edited by R. Marrus, M. Prior, and H. Shugart (Plenum Press, New York, 1976).

[16]W. Heisenberg, Z. Physik **39**, 499 (1926).

[17]H.A. Bethe and E.E. Salpeter, *Quantum Mechanics of One- and Two-Electron Atoms* (Springer-Verlag, Berlin, 1957).

[18]G. Herzberg and H.R. Moore, Can. J. Phys. **37**, 1293 (1959).

[19]E. Merzbacher, *Quantum Mechanics* (John Wiley and Sons, Inc., New York, 1970).

[20]C.L. Pekeris, Phys. Rev. **126**, 143 (1962).

[21]R.E. Knight and C.W. Scherr, Rev. Mod. Phys. **35**, 431, 436 (1963).

[22]G.W.F. Drake and A. Dalgarno, Astrophys. J. **157**, 459 (1969).

[23]S.D. Rosner and F.M. Pipkin, Phys. Rev. **A1**, 571 (1970).

[24]B. Fau, A. Lurio, and D. Grischkowsky, Phys. Rev. Lett. **41**, 1460 (1978).

[25]A. Jette, T. Lee, and T.P. Das, Phys. Rev. **A9**, 2337 (1974).

[26]P.B. Bevington, *Data Reduction and Error Analysis* (McGraw-Hill, New York, 1969).

[27]H.G. Dehmelt, Adv. Atom. and Mol. Phys. **3**, 53 (1967); **5**, 109 (1969).

[28]M.H. Prior and E.C. Wang, Phys. Rev. **A16**, 6 (1977).

[29]W. Paul and H. Steinwedel, Z. Naturforsch. **8a**, 448 (1953).

[30]E. Jahnke, F. Emde, and F. Losch, *Tables of Higher Functions* (B.G. Verlagsgesellschaft, Stuttgart, 1960).

[31]R.F. Wuerker, H. Shelton, and R.V. Langmuir, J. Appl. Phys. **30**, 342 (1959).

[32]A.V. Gaponov and M.A. Miller, JEPT **7**, 168 (1958).

[33]R. Iffländer and G. Werth, Fifth Inter. Conf. Atom. Phys. (1976).

[34]M. Baril and A. Septier, Rev. de Phys. Appl. **9**, 525 (1974).

[35]H.G. Dehmelt and F.L. Walls, Phys. Rev. Lett. **21**, 127 (1968).

[36]C. Schwebel, P.A. Moller, and P.T. Manh, Rev. de Phys. Appl. **10**, 227 (1975).

[37]L. Spitzer, *Physics of Fully Ionized Gases* (Interscience Publishers, Inc., New York, 1956).

[38]R.D. Knight and M.H. Prior, J. Appl. Phys. (To be published March 1979).

[39]J. André and F. Vedel, J. Physique **38**, 1381 (1977).

[40]J.A.R. Samson, *Techniques of Vacuum Ultraviolet Spectroscopy* (John Wiley and Sons, Inc., New York, 1967).

[41]W.R. Hunter, D.W. Angel, and R. Tousey, Appl. Optics **4**, 891 (1965).

[42]M. Born and E. Wolf, *Principles of Optics* (Pergamon Press, Oxford, 1975).

[43]A. Mitchell and M. Zemansky, *Resonance Fluorescence and Excited Atoms* (Cambridge University Press, London, 1934).

[44]G. Feinberg and J. Sucher, Phys. Rev. Lett. **26**, 681 (1971).

[45]W.R. Johnson and C. Liu, Phys. Rev. A**9**, 1486 (1974).

[46]D.A. Church and H.G. Dehmelt, J. Appl. Lett. **40**, 3421 (1969).

[47]R. Iffländer and G. Werth, Metrologia **13**, 167 (1977).